

Investigation on carrier recombination and energetics of kesterite materials for photovoltaic applications

Zeng, Xin

2016

Zeng, X. (2016). Investigation on carrier recombination and energetics of kesterite materials for photovoltaic applications. Doctoral thesis, Nanyang Technological University, Singapore.

<https://hdl.handle.net/10356/65938>

<https://doi.org/10.32657/10356/65938>



NANYANG
TECHNOLOGICAL
UNIVERSITY

Investigation on Carrier Recombination and
Energetics of Kesterite Materials for Photovoltaic
Applications

ZENG XIN

SCHOOL OF MATERIALS SCIENCE & ENGINEERING

2015

Investigation on Carrier Recombination and
Energetics of Kesterite Materials for Photovoltaic
Applications

ZENG XIN

SCHOOL OF MATERIALS SCIENCE & ENGINEERING

A thesis submitted to the Nanyang Technological University in
partial fulfillment of the requirement for the degree of
Doctor of Philosophy

2015

Abstract

$\text{Cu}_2\text{ZnSnS}_{4-x}\text{Se}_x$ (CZTSSe) based kesterite solar cells, comprise of abundantly available and environmental benign elements, which have drawn widespread attention as they are excellent candidates for thin film solar cells. In addition, other advantageous qualities of CZTSSe that makes it suitable for thin film applications include its high absorption coefficient in the visible wavelength range, intrinsic p-type conductivity and a direct band gap.

The technologies available to fabricate high quality CZTSSe absorbers are still in their infancy, with the solution based techniques requiring either a highly toxic and dangerous solvent such as hydrazine, or an organic solvent such as methanol. Thus, an environmentally green and cost effective method is in current high demand.

In this work, an aqueous-based chemical spray pyrolysis technique was used to deposit a uniform CZTS layer on Mo coated glass. The film was further processed in a high temperature selenization furnace to obtain a highly crystalline CZTSSe absorber. Using X-ray diffraction (XRD) and Raman spectroscopy, no detectable secondary phase was observed from the CZTSSe absorbers. A uniform elemental distribution was suggested from SIMS depth profiling, except for slightly increased concentrations of Zn and S close to the Mo contact layer. The S/Se ratio can be tuned by applying different amounts of Se in the selenization process, which resulted in similar solar cell conversion efficiencies above 5%. The highest efficiency obtained after process optimization was 7.5%, which to the best of our

knowledge, is the highest efficiency obtained for a kesterite containing solar cell fabricated by an aqueous-based solution method.

The carrier recombination behavior in CZTSSe absorber was investigated by temperature and power dependent photoluminescence (PL) spectroscopy. The donor-acceptor pairs (DAPs) transition was concluded as the dominant recombination mechanism. Non-radiative recombination was responsible for the large temperature quenching effect observed for the PL intensity. The thermal activation energies of the non-radiative recombination channels have been calculated and present a higher value for the post-optimized CZTSSe absorber, indicating a less severe non-radiative recombination for post-optimized CZTSSe.

The energetics alignment of the CZTSSe solar cells was investigated by impedance spectroscopy. Three solar cell devices with a similar short circuit current density (J_{sc}) were investigated and revealed a similar recombination resistance from the analysis of their impedance spectra. The calculated results from the Mott-Schottky relationship indicated a similar carrier concentration but a variation in the energetics alignment, which was considered as one of the critical factors affecting the V_{oc} . The schematic band alignment was presented for a better understanding V_{oc} origin.

Alternative CMTSSe (M=Ca, Ni, Mg, Mn) absorbers were also fabricated via a spray pyrolysis method followed by selenization. XRD and Raman spectroscopy showed that the CMTSSe (M=Ca, Ni, Mg) samples all coexisted with additional binary and tertiary phases. Similar to the CZTSSe, the samples of CMnTSSe

presented a single kesterite phase. Furthermore, the solar cell devices based on the CMnTSSe absorber generated a 0.07% conversion efficiency, indicating it as a potential alternative for CZTSSe-based absorbers.

Acknowledgement

During the time of my PhD, I have encountered great challenges and difficulties in my research work. Without doubt, I could not have completed my studies without the assistance of my colleagues, friends and mentors. I would like to take this opportunity to thank all the people who have kindly offered their help.

First of all, I would like to show my sincerest thanks to both of my supervisors, Assoc. Prof Chen Xiaodong and Prof. Subodh Mhaisalkar, for their continuous guidance, encouragement and support. Their guidance has led me into an exciting and promising research field. And their encouragement has helped me through all the dejected times when the research work did not go to plan. Their support not only came from the advanced laboratory facilities they have provided for the work, but most importantly, the caring assistance they have given.

Secondly, I am grateful for Asst. Prof Lydia Wong for her leadership of the thin film solar cell team, where she directed me to a higher level of understanding towards my research work as well as providing consistent support and patience to me throughout the work. She has been a good mentor and advisor for the entire time. Furthermore, I would also like to thank Dr Jinesh, Dr. Sudip, Dr. Mai, Dr Pablo and Dr Tom for their help and support towards my research work.

Thirdly, I would love to express my hearty gratitude to my lab friends, Hui Min, Mengxi, Sun Juan and Tianliang. I could not have reached this stage without them.

They have always been there for me even at the most difficult times and the memories will influence me for my future life.

Last but not least, I would like to thank all the group members and friends in ERI@N who help me directly and indirectly. We together have made the lab an excellent facility for our research work.

Table of Contents

ABSTRACT	III
ACKNOWLEDGEMENT	VI
TABLE OF CONTENTS.....	VIII
LIST OF FIGURES	XII
CHAPTER 1 INTRODUCTION	1
1.1 Introduction and Background	1
1.2 Motivation.....	2
1.3 Objective and Scope	3
1.4 Thesis Contribution.....	5
CHAPTER 2 LITERATURE REVIEW.....	7
2.1 Thin Film Photovoltaic Development and Advantages	7
2.2 Kesterite Materials and Solar Cell Working Principle	8
2.2.1 Structure of Kesterite Materials	8
2.2.2 Working Principle of Kesterite Solar Cell	10
2.3 Review of Promising Solar Cell Fabrication Techniques	11
2.3.1. Non-Vacuum Techniques.....	12
2.3.2. Vacuum Techniques.....	14

2.4 Challenging Aspects of Kesterite Solar Cells: Factors Affecting the V_{oc}	15
2.4.1 V_{oc} Deficit Study from Current-Voltage-Temperature (JVT) Measurements of the Solar Cell Performance	15
2.4.2 Recombination study of CZTSSe Films by PL Spectroscopy	18
2.4.3 Electronic Structures Study of the Kesterite Materials and its Defects Complexity towards Chalcopyrite Materials	21
2.4.4 Impedance Spectroscopy on Solar Cells	25
 CHAPTER 3 EXPERIMENTAL	 31
3.1 Kesterite Solar Cell Fabrication and Measurement	31
3.1.1 Spray Pyrolysis of CZTS on Mo-Coated Glass	31
3.1.2 High Temperature Selenization of CZTS Film to Form CZTSSe Absorber	32
3.1.3 Device Fabricated on Top of CZTSSe	33
3.1.3 Solar Cell Measurement	34
3.2 Characterization of CZTSSe Thin Film	34
3.3 Impedance Spectroscopy on Kesterite Solar Cell Devices	36
 CHAPTER 4 SOLUTION PROCESSABLE CZTSSE ABSORBER	
DEVELOPMENT AND CHARACTERIZATION	37
4.1 Morphology Analysis and Phase Identification of CZTSSe thin film	37
4.1.1 Investigate Acidic Effect on CZTS Morphology and Crystallinity Growth	37
4.1.2 Phase Analysis and Elemental Distribution Discussion on CZTSSe Thin Film	40
4.2 Solar Cell Performance (J-V and EQE) Discussion with Different Se Concentration in CZTSSe	44
4.3 Summary	52

**CHAPTER 5 INVESTIGATION OF CARRIER RECOMBINATION
MECHANISM IN CZTSSE ABSORBER 54**

5.1 Analyzing Carrier Transition and Temperature Quenching Effect by PL Spectroscopy 55

5.2 Selenization Temperature Effect on Non-radiative Recombination Channels 61

5.3 Comparison Analysis on Recombination Behavior in CZTSSe 64

5.3.1 Phonon Assisted DAPs Transition Analysis from PL Spectra 64

5.3.2 Luminescence Energy Discussion and its Relation to the V_{oc} of the Solar Cell 67

5.3.3 Comparison Study on Thermal Activation Energy of Non-radiative Recombination .. 70

5.4 Minority Carrier Lifetime Study by TRPL on CZTSSe-7 Absorber 70

5.5 Summary 74

**CHAPTER 6 ENERGETICS STUDY AND DISCUSSION ON THE V_{oc} OF
CZTSSE SOLAR CELLS 76**

6.1 V_{oc} Analysis and Comparison from J-V and EQE Measurement of the Solar Cells 76

6.2 Investigate Recombination Resistance from Nyquist Plot of Impedance Spectroscopy .. 81

6.3 Energetics Alignment Illustration and Discussion from Mott-Schottky Relation 82

6.4 Summary 88

**CHAPTER 7 CMTSSE (M=METAL) MATERIAL DEVELOPMENT AND
APPLICATION IN SOLAR CELL 90**

7.1 Investigation on CMTSSE (M=Mg, Mn, Ni, Ca) as Potential Kesterite Absorbers. 90

7.2 Crystal Structure and Phase Analysis of CMTSSE (M=Ca, Ni, Mg, Mn) 93

7.3 Light J-V Measurement Discussion on CMTS _{Se} Solar Cells	99
7.4 Summary	101
CHAPTER 8 CONCLUSION AND PROSPECTS.....	102
8.1 Conclusion and Overall Summary	102
8.2 Future Work Recommendation	105
8.2.1 Analyze the Illumination Difference between the Absorber and Device	106
8.2.2 Investigate the Back Surface Field for Kesterite Solar Cell	106
8.2.3 Investigate the Impedance Behavior of the Solar Cell under Different Illumination Conditions.....	107
8.2.4 Tuning the Band Gap by Cation Incorporation and Replacement	108
REFERENCE	108
APPENDIX A: LIST OF ABBREVIATIONS	118
APPENDIX B: LIST OF PUBLICATIONS.....	119
Journals.....	119
Conferences	119
Patents	119

List of Figures

Figure 2-1 Structure relationship of ZnS, CIS and CZTS ¹⁵	9
Figure 2-2 Origination of the kesterite structure ¹⁵	9
Figure 2-3 Kesterite solar cell structure.....	10
Figure 2-4 Band diagram illustration of kesterite solar cell working principle.	11
Figure 2-5 a) top view and b) cross-sectional view of CZTSSe film with 12.6% efficiency ¹²	13
Figure 2-6 J-V current of CZTSSe and CZTGeSSe solar cells fabricated via nano-particle ink deposition technique ³⁰	14
Figure 2-7 JVT analysis of hydrazine CZTSSe and CIGS solar cell ³⁴	17
Figure 2-8 Extracted E_a from JVT measurement (left) and PL spectra with fitting from a CZTSSe absorber (right) ³⁶	18
Figure 2-9 Power dependent a) and temperature dependent b) PL spectrum ³⁷	19
Figure 2-10 Temperature dependent PL spectra on a CZTSSe monograin ³⁸ ...	20
Figure 2-11 Band gap bowing effect with different S/Se compositions ¹¹	22
Figure 2-12 Band positions and alignment of semiconductors used in thin film solar cell ¹¹	23
Figure 2-13 Defects energy level calculated in CZTS structure. ⁵¹	24
Figure 2-14 Compensated defects complexes calculated from nonstoichiometric CZTS ⁵¹	25
Figure 2-15 Impedance spectra of Si solar cell for different sunlight intensity at a) forward bias 0.2 V b) reversed bias 0.5 V ⁶⁰	27

Figure 2-16 The Si solar cell (a) total resistance changed with applied DC bias (b) R_s changed with applied DC bias. ⁶⁰	28
Figure 2-17 The Si solar cell (a) capacitance spectra at 0 applied DC bias with different blend composition (b) Mott-Schottky relation derived from impedance spectra	30
Figure 3-1 Setup of spray pyrolysis for CZTS film deposition	32
Figure 3-2 Setup for high temperature selenization of CZTS to form highly crystalline CZTSSe	33
Figure 4-1 (a) Surface FE-SEM imaging of CZTS film without HCl precursor solution treatment (b) cross-section FE-SEM imaging of CZTS film without HCl precursor solution treatment (c) Surface FE-SEM imaging of CZTS film with HCl precursor solution treatment (d) cross-section FE-SEM imaging of CZTS film with HCl precursor solution treatment.....	39
Figure 4-2 (a) FE-SEM top view of post-selenized CZTSSe (b) FE-SEM cross-sectional view of posted CZTSSe.....	40
Figure 4-3 XRD curves of (a) as-deposited CZTS (b) XRD curves of post-selenized CZTSSe.....	41
Figure 4-4 Raman spectra of (a) as-deposited CZTS film (b) post-selenized CZTSSe.....	42
Figure 4-5 SIMS depth profile on CZTSSe thin film grown on Mo-coated glass	43
Figure 4-6 Cross-section FESEM image of total device with layers labeled	44
Figure 4-7 Raman spectrum of low-Se-content CZTSSe	45
Figure 4-8 light J-V curves of control device and low-Se-content device.....	46

Figure 4-9 (a) EQE plot of control cell and low-Se-content cell. (b) Band gap plots of both solar cells.....	47
Figure 4-10 Light J-V plot of solar cells with varying Se concentration in the absorbers, the amount indicted in the figure referred to the adding amount of Se pellets during selenization.....	48
Figure 4-11 (a) cross-section image of champion device absorber (b) J-V curve of champion device with major parameters inset.....	50
Figure 4-12 EQE curve of champion device with 7.5% efficiency (band gap calculation inset).....	50
Figure 4-13 Light J-V plots of Zn(O,S) and Zn-Sn-O buffer layer solar cells with CdS as reference	52
Figure 5-1 (a) spectra of temperature dependent photoluminescence on CZTSSe-5 film (b) temperature quenching effect fitting with two non-radiative recombination parameters.....	55
Figure 5-2 radiative recombination transition types, (a) band-to-band transition (b) free-to-band transition (c) donor-acceptor pairs (DAPs) transition	56
Figure 5-3 (a) spectra of power dependent photoluminescence on CZTSSe-5 film (b) power law fitting of the luminescence intensity versus laser power with a coefficient of 0.93 ± 0.013	59
Figure 5-4 (a) spectra of temperature dependent photoluminescence on CZTSSe-7 film (b) temperature quenching effect fitting with one non-radiative recombination parameter	62

Figure 5-5 (a) spectra of power dependent photoluminescence on CZTSSe-7 film (b) power law fitting of the luminescence intensity versus laser power with a coefficient of 0.74 ± 0.02	64
Figure 5-6 Raman spectra of CZTSSe-7 with indicating the vibration mode	66
Figure 5-7 Power dependent PL on CZTSSe-7 with power range from 100 μ W to 1 mW.....	67
Figure 5-8 Power law fitting in the range of 0.1-1 mW with calculated coefficient value $k=0.97 \pm 0.04$	67
Figure 5-9 Illustration of “mid-gap states” inside the forbidden energy band of semiconductor	68
Figure 5-10 value of V_{oc} , PL peak energy and band gap of both CZTSSe-5 and CZTSSe-7 device	69
Figure 5-11 a) spectra of TRPL on CZTSSe-7 absorber with different power intensity (b) fitting results of minority carrier lifetime τ	73
Figure 6-1 (a) J-V curves of selected solar cells under dark and light (one sun AM 1.5) conditions (b) EQE curves of selected solar cells	79
Figure 6-2 (a) impedance spectra fitting by Z-view software with the fitting circuit inset (b) R_{rec} fitting results from 0-0.5 V for all three cells.	82
Figure 6-3 Mott-Schottky relation plot extracts the flat band potential at AC frequency 5k.	84
Figure 6-4 Proposed schematic energetic alignment pathway, from (a) \rightarrow (b) and from (c) \rightarrow (d), that satisfy the results of flat band potential calculation (considering same carrier concentration)	85

Figure 6-5 Carrier density calculated from different AC frequency impedance spectroscopy.	87
Figure 6-6 Flat band potentials calculated from different AC frequency impedance spectroscopy.	88
Figure 7-1 relative ionic radii of atoms ¹¹¹	92
Figure 7-2 Earth abundant elements with price	93
Figure 7-3 XRD curves of as-deposited CMTS (M=Ca, Ni, Mg, Mn) films by spray pyrolysis on Mo coated glass (with CZTS as reference).....	94
Figure 7-4 XRD curves (two views) of post-selenized CMTS _{Se} (M= Ca, Ni, Mg, Mn) films (with CZTS as reference).....	95
Figure 7-5 Raman spectra of as-deposited CMTS films	96
Figure 7-6 Raman spectra of post-selenized CMTS _{Se} compare to CZTS _{Se} with same selenization process.	98
Figure 7-7 Cross-section FE-SEM image of post-selenized CMTS _{Se} comparing to CZTS _{Se}	99
Figure 7-8 Light J-V curves of CMTS _{Se} (M=Ni, Mg, Mn) solar cells under one sun illumination comparing with CZTS _{Se} solar cell	100
Figure 8-1 configuration for back surface field study by impedance spectroscopy.....	107
Figure 8-2 Schematic illustration of light wavelength dependence on penetration depth.....	108

Chapter 1 Introduction

1.1 Introduction and Background

The development of sustainable energy, in particular, solar energy has significant meaning for the human society, as it translates to harvesting energy directly from the sun. Photovoltaic (PV) devices involve the direct transfer of energy from sunlight to electricity. The first practical PV solar cell was demonstrated in Bell Labs in 1954 using silicon p-n junctions.¹ Thin film PVs have emerged since the 1970s, and includes chalcopyrite $\text{CuIn}_{1-x}\text{Ga}_x\text{S}_{2-x}\text{Se}_x$ (CIGSSe), CdTe and amorphous silicon (a-Si) containing solar cells.² As CdTe solar cells require highly toxic cadmium elements and a-Si solar cell efficiency is limited by its intrinsic problem of recombination, chalcopyrite type CIGSSe solar cell has become increasingly promising in this field.³

CIGSSe materials have a very high absorption coefficient of up to 10^5 cm^{-1} and an adjustable direct band gap between 1.0-1.7 eV, which can be varied by modifying the concentrations of In and Ga in the crystal lattice.⁴⁻⁵ These properties make it highly suitable for visible light (400-800 nm wavelength range) harvesting in PV devices. In principle, a two micrometer layer of CIGSSe thin film is able to absorb 90% of the incoming solar energy. CIGSSe materials have been used to make flexible solar cells without compromising the power conversion efficiency (PCE).⁶⁻⁸ CIGSSe solar cells have very good chemical and physical stability that can resist the detrimental effects of illumination, temperature variation and humidity.⁹ So far, the CIGSSe solar cells have obtained a PCE of 21.7% under laboratory

conditions and 15.7% for a demonstration module.¹⁰ However, the low elemental abundance and the high cost of In and Ga, render CIGSSe-containing PVs unsustainable and costly.

Indium and gallium free kesterite semiconductor such as $\text{Cu}_2\text{ZnSnS}_{4-x}\text{Se}_x$ (CZTSSe) makes it a promising candidate for solar cell development due to the high abundance and low cost of Zn and Sn. As the In (III) and Ga (III) are replaced by Zn (II) and Sn (IV), it possesses similar structural, physical and electrical properties to that of CIGSSe. CZTSSe is an intrinsic p-type semiconductor with direct band gap (E_g) ranging from 1.0 eV (pure CZTSe) to 1.5 eV (pure CZTS).¹¹ The high absorption coefficient and hole conductivity in polycrystalline CZTSSe lead to good light harvesting and charge separation in the solar cell devices. The solar cell design for CZTSSe can adopt the same structure as CIGSSe solar cell with a substrate configuration to enhance the charge collection at the p-n junction depletion region. To date, the power conversion efficiency for kesterite solar cells reaches 12.6% with hydrazine-related solution based process,¹² which indicates a promising future for further development.

1.2 Motivation

CZTSSe solar cells have the potential to be developed into highly efficient thin film PV devices with earth abundant and low cost elements. However, the fabrication processes remain challenging despite efforts to adapt these from the relatively mature CIGSSe fabrication procedures. Currently, the highest efficiency obtained for CZTSSe solar cell was achieved for a device fabricated under an inert

argon atmosphere with hydrazine solvent, which is a highly toxic chemical. Most of the solution-based fabrication techniques involve organic solvents or ligands, which are not considered effective and environmental benign. Other techniques such as vacuum-based processes are observed to suffer from severe loss of Sn, and only achieved 9.2% efficiency combined with the high cost of fabrication.¹³ Therefore, a scalable, cost-effective and environmental benign technique is highly demanded for CZTSSe fabrication.

To date, the most critical problem limiting the kesterite solar cell efficiency is the open circuit voltage (V_{oc}). Compared to the high quality CIGSSe solar cell which has a V_{oc} deficit ($E_g - V_{oc}$) of around 500 mV, the CZTSSe solar cells have more than a 600 mV V_{oc} deficit.¹⁴ This phenomenon has been primarily analyzed and attributed to various aspects, such as interface recombination at CdS/CZTSSe, deep defects formation and short minority carrier lifetime.¹⁵ However, the V_{oc} limiting factors are still inconclusive and a detailed mechanism is still under investigation. For example, the carrier recombination mechanism from device quality CZTSSe has yet to be established. The energetics alignment has only been studied between the buffer layer and CZTSSe, without considering its effect on the V_{oc} .¹⁶⁻¹⁸ Research targeting these problems is crucial for understanding further the functionality of kesterite solar cells towards improving their power conversion efficiencies.

1.3 Objective and Scope

By considering the challenges encountered during the development of the kesterite solar cell aforementioned, the **objectives** and scopes of this research work cover the following aspects:

1. Develop a novel and environmentally friendly aqueous-based solution technique for CZTSSe thin film absorber deposition

- a. Investigate the solution acidity effect on the morphology and uniformity of as-deposited CZTS thin film by chemical spray pyrolysis (CSP).
- b. Analyze the impact of morphology, phase purity and elemental distribution on poly-crystalline CZTSSe thin films.
- c. Study the effect of band gap tuning, by Se incorporation, on the solar cell performance.

2. Investigate the carrier recombination mechanism in CZTSSe thin films by studying photoluminescence spectroscopy

- a. Investigate the transition type of carrier recombination in CZTSSe by temperature and power dependent photoluminescence spectroscopy
- b. Analyze the impact of CZTSSe selenization temperature on the luminescence energy and thermal activation energy of the non-radiative recombination
- c. Investigate the role of defect complexes of CZTSSe on the luminescence
- d. Explore the minority carrier lifetime of CZTSSe by time-resolved photoluminescence (TRPL) spectroscopy

3. Explore energetics alignment effect on the V_{oc} of the solar cell by impedance spectroscopy

- a. Investigate the forward bias effect on device recombination resistance by analyzing Nyquist plots derived from impedance spectroscopy
 - b. Explore the CZTSSe carrier concentrations and flat band potentials from Mott-Schottky relation.
 - c. Investigate energetic alignment of the solar cell devices and its relation with the V_{oc} of the solar cell.
- 4. Crystal structure analysis of CMTSSe (M=Ca, Ni, Mg, Mn) materials for solar cell applications**
- a. Illustrate the necessity and potential of CMTSSe as a light absorber
 - b. Analyze the crystal structure and identify secondary phases in CMTSSe film using XRD and Raman spectroscopy
 - c. Demonstrate the application of CMTSSe in solar cells and investigate the J-V properties under light conditions.

1.4 Thesis Contribution

The original scientific contribution from this research work is listed below:

1. Demonstrated a novel, scalable and environmental benign method to fabricate device quality CZTSSe absorber. A 7.5% PCE solar cell has been obtained from this work.
2. Identified the carrier recombination as the donor-acceptor pairs (DAPs) transition in CZTSSe absorber. Analyzed the thermal activation energy of the non-radiative recombination in CZTSSe. Illustrated the role of defects complexes in the carrier recombination.

3. Investigated the recombination resistance and energetics alignment of the solar cells. Analyzed the effect of energetics alignment on the V_{oc} of the solar cells using the Mott-Schottky relation.
4. Analyzed the crystal structure and phase purity of CMSTSSe materials. Demonstrated a 0.07% efficiency CMnTSSe solar cell with a diode-type behavior. This was the first description of a CMTSSe-containing kesterite solar cell.

Chapter 2 Literature Review

2.1 Thin Film Photovoltaic Development and Advantages

The current PV market is dominated by monocrystalline and polycrystalline silicon, due to its abundance and high efficiency.¹⁹ However, the thin film PV has become a rising alternative over the recent decades,²⁰ where devices containing CIGSSe, CdTe and a-Si, have demonstrated their high efficiencies in both laboratory and industry settings.²¹⁻²³ These direct band gap semiconductors display a very high absorption coefficient and band gap suitable for visible light harvesting. Thus, a highly efficient solar cell can be achieved with only a several micrometer thickness of absorber,²⁴ which can be considered a remarkable saving of materials, and allows the demonstration of flexible PV devices without compromising their efficiency.²⁵⁻²⁶

The solar cell efficiency is measured under controlled environment with solar simulator generating one sun spectrum at AM1.5 condition (irradiance energy density is 1000W/m²). The solar cell efficiency is calculated by selecting the maximum point of $V \times J$, where V is the voltage and J is the current density. The fill factor (FF) can be calculated as: $FF = \frac{P_{\max}}{V_{oc} \times J_{sc}}$, where P_{\max} is the maximum power selected.

So far, the chalcopyrite CIGSe and CdTe containing solar cell have reached efficiencies of 20.9% and 19.6 % respectively.¹⁰ However, due to the high cost of

indium and gallium, the future development of the chalcopyrite solar cells is expected to be restricted. For CdTe solar cell, the high toxicity of the cadmium is the critical issue for its development, as is the rarity and cost of tellurium. Therefore, alternative absorbers, with similar electronic and optical properties are in high demand.

The kesterite CZTSSe material is considered as one of the most promising candidates in this field. It shares similar advantages of CIGSSe material, such as high absorption coefficient and tunable band gap, but contains only cheap and earth abundant elements. Thanks to the efforts from worldwide research, the kesterite solar cell efficiency reached 12.6% in 2014, starting from 0.66% in 1996, ¹⁴ and displays a prominent future towards commercial development and utilization.

2.2 Kesterite Materials and Solar Cell Working Principle

2.2.1 Structure of Kesterite Materials

The kesterite structure is originally derived from the cubic zinc blende structure of II-VI group semiconductor, where both II and VI atoms are tetrahedral coordinated to each other. As illustrated in figures 2-1 and 2-2, the quaternary kesterite unit cell contains two zinc blende unit cells with an orderly substitution of group II atoms with group I atoms and one group IV atoms. The kesterite unit cell can also be considered to be derived from the chalcopyrite ternary structure with substitution of group III atoms with group II and group IV atoms. ¹⁵ The location order of the elements is difficult to control, and can lead to a detrimental

effect on solar cell performance. This problem is addressed further in chapters 5 and 6.

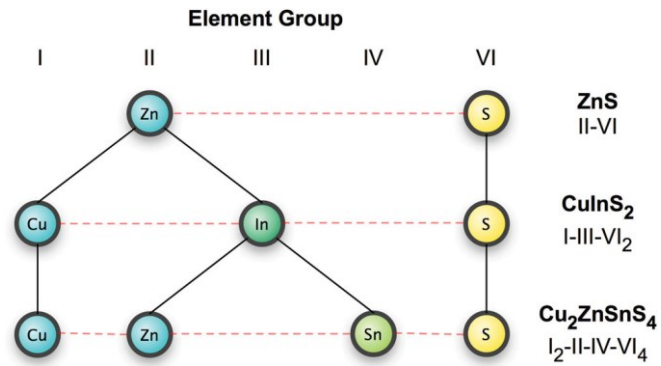


Figure 2-1 Structure relationship of ZnS, CIS and CZTS ¹⁵

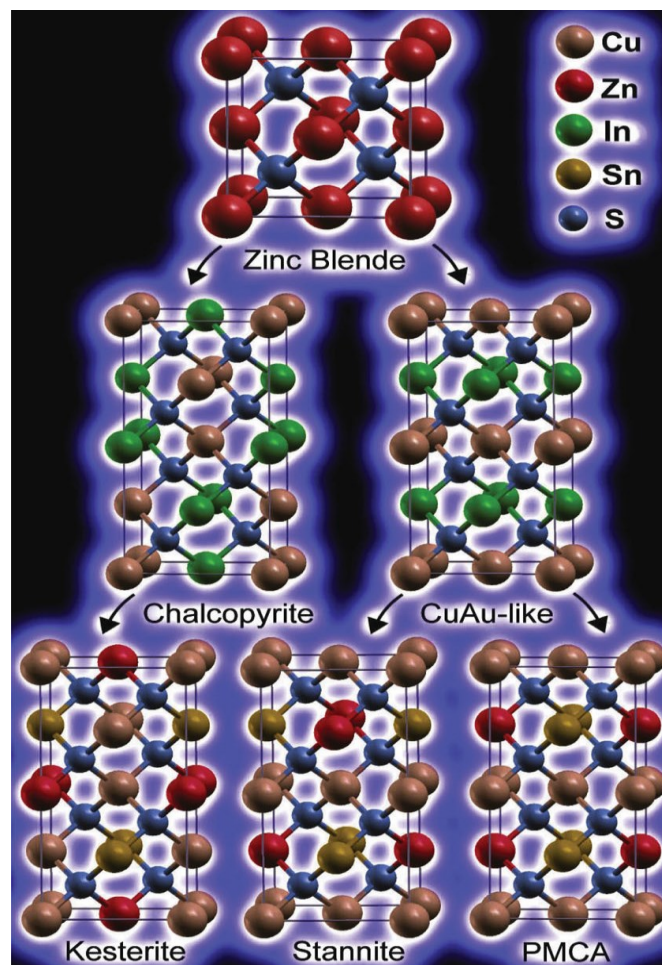


Figure 2-2 Origination of the kesterite structure ¹⁵

2.2.2 Working Principle of Kesterite Solar Cell

The kesterite solar cell adopts a similar architecture to chalcopyrite solar cells, as shown in figure 2-3. The CZTSSe absorber is deposited on the molybdenum (Mo) coated glass substrate, followed by thin layer coating of CdS as the buffer layer, which helps the band alignment and charge separation at the p-n junction. On top of the CdS layer, an intrinsic ZnO and transparent conducting oxide (TCO) are sputtered as the n-type window layer, followed by metal grid deposition. ⁴

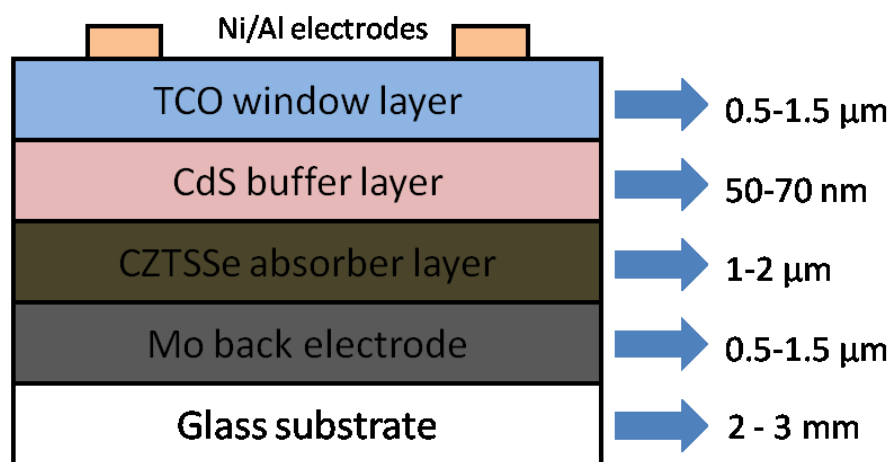


Figure 2-3 Kesterite solar cell structure

The working principle of the kesterite solar cell is based on the p-n junction of the diode. The p-n junction is formed between the intrinsic p-type CZTSSe absorber layer and the n-type buffer layer, as well as the window layers. The p-n junction can generate a built-in electrical field through the diode, which is called depletion region. After incident light reaches on the absorber layer, electrons are activated and ejected from the valence band (VB) to the conduction band (CB) of the absorber. When the electrons diffuse into the depletion region, the electrons will drift through the p-n junction into the n-type TCO layer by the force from the built-

in electrical field; while the holes from p-type semiconductor diffuse to the Mo electrode. Therefore, the charge separation and carrier collection are achieved. With the help of an external circuit, the conversion of optical energy to electronic energy is completed. Figure 2-4 provides an illustration of the working principle of kesterite solar cells. The conduction band offset (CBO) is also illustrated as the CZTSSe and CdS layers form a hetero-junction at the semiconductor interface, thus band alignment is critical for kesterite solar cells.

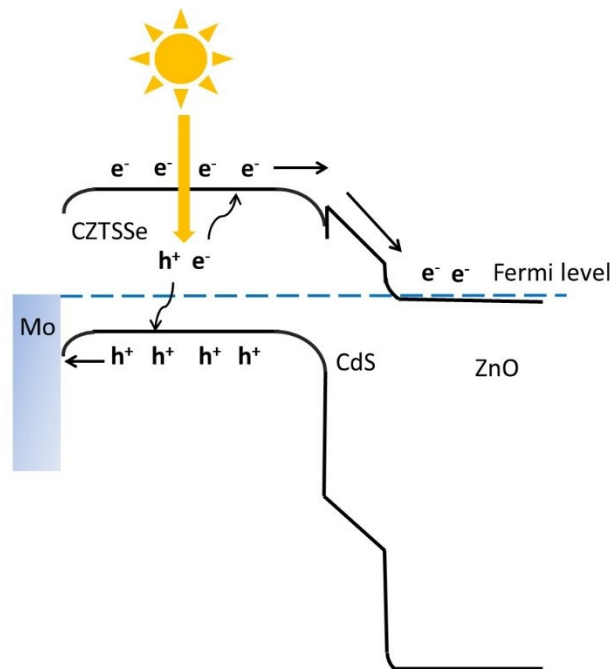


Figure 2-4 Band diagram illustration of kesterite solar cell working principle

2.3 Review of Promising Solar Cell Fabrication Techniques

The CZTSSe thin films have been successfully deposited by various vacuum and non-vacuum techniques, where outstanding solar cell performances have been obtained. Some of these techniques are introduced as follows

2.3.1. Non-Vacuum Techniques

A world record 12.6% efficiency for CZTSSe solar cell was held by a non-vacuum solution-based technique developed by Mitzi and co-workers.¹² Hydrazine was used as solvent for dissolving and dispersing the required binary and elements precursors followed by a spin-coating deposition process and high temperature annealing step. The high quality CZTSSe films were obtained by controlling the S/Se ratio during selenization step. Solar cells with greater than 10% efficiency were obtained over a wide range of S/Se ratios.²⁷ In addition, the thickness of buffer layer and window layer were also adjusted to improve the light transmittance for improved current collection. The 2 μm grains were observed to penetrate the absorber layer (figure 2-5), which helped to reduce the recombination and facilitate the charge separation. The composition was designed as $\text{Cu}/(\text{Zn}+\text{Sn})=0.8$ and $\text{Zn}/\text{Sn}=1.2$ to avoid the detrimental Cu-rich secondary phase formation. So far, this is still considered the best method to fabricate CZTSSe solar cells, as it does not require extra solvents or elements that may contaminate the final absorber. However, hydrazine is a highly toxic solvent that should only be used under the protection of an inert gas atmosphere,²⁸ which may restrict any future scalable production.

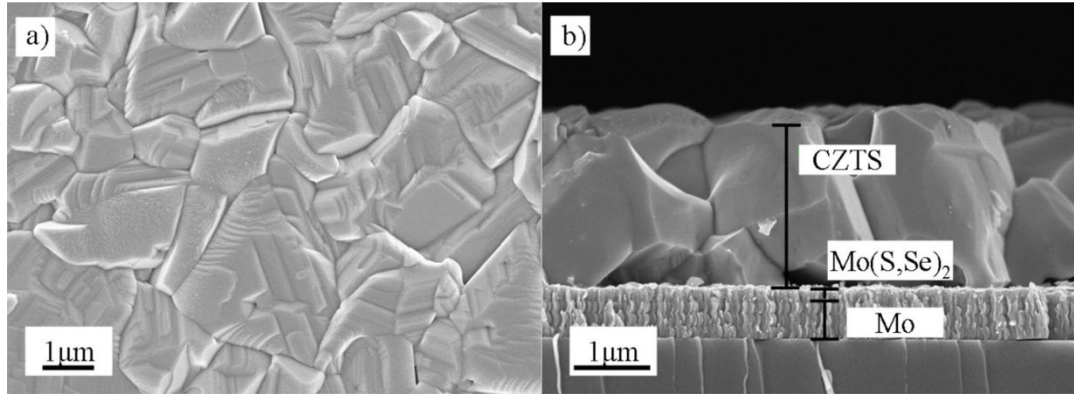


Figure 2-5 a) top view and b) cross-sectional view of CZTSSe film with 12.6% efficiency ¹²

Another popular technique to fabricate high efficiency kesterite solar cells is to use nano-particle ink as the precursor. Miskin and co-workers synthesized CZTS nano-particles via a hot-injection method. ²⁹ The nano-particle structure was confirmed by transmission electron microscopy (TEM) and Raman spectroscopy. The ink was spin-coated on Mo coated glass followed by a high temperature selenization step, which resulted in solar cell efficiencies up to 9%. ²⁹ Hages and co-workers also demonstrated the replacement of Sn by Ge in the nano-particles, as a technique to adjust the band gap of absorber. With an alloying of 30% Ge, the band gap could be modified from 1.1 eV of CZTSSe to 1.18 eV of CZTGeSSe. The corresponding efficiency was improved from 8.4% to 9.4%. ³⁰ This work provided guidance on adjusting the band gap by cation substitution, mimicking the Ga replacement in CIGSSe absorbers, to pursue better performance of the solar cells. The comparison of the J-V curves for CZTSe and CZTGeSSe is shown in figure 2-6.

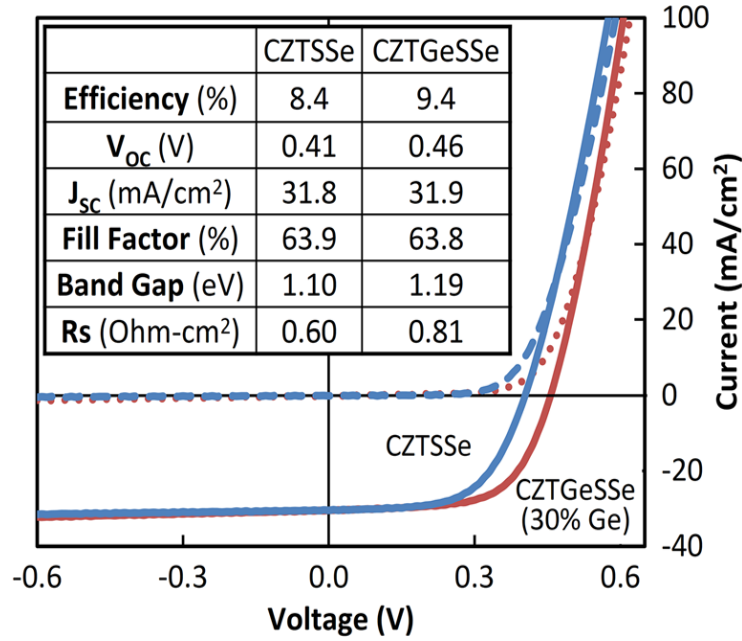


Figure 2-6 J-V current of CZTSSe and CZTGeSSe solar cells fabricated via nano-particle ink deposition technique ³⁰

Additionally, Cao and co-workers fabricated a CZTSSe absorber by applying binary and tertiary nano-particles. ³¹ Metal sulfide precursors were synthesized and spin-coated on Mo glass followed by high temperature selenization. A 9.6% efficiency was demonstrated in this work, even though a thick layer of carbon coated CZTSSe small grains remained on the MoSe₂ layer. The carbon residues originated from the organic solvent introduced from the precursor solution and was considered a limitation of this method to further improve the absorber quality.

2.3.2. Vacuum Techniques

Co-evaporation was demonstrated as a good technique for depositing CIGSSe absorber and a world record efficiency of 20.9% was achieved via the co-evaporation of elemental copper, indium, gallium and selenium. However, for the CZTSSe absorber deposition encountered Sn loss during the process that hindered

the control of elemental stoichiometry. So far, the best efficiency achieved is 9.2% by Repin and co-workers from National Renewable Energy Laboratory.¹³ They used the same equipment and procedures as their CIGSe processing, which achieved a 20% efficiency for the CIGSe solar cell. The In and Ga sources were replaced by Zn and Sn and they were able to attain very high J_{sc} (37.4 mA/cm²) but low V_{oc} (377 mV). Similarly, Shin and co-workers deposited CZTS absorber by the thermal evaporation of elemental Cu, Zn, Sn and S.³² This selenium free device attained an efficiency of 8.4%, with a V_{oc} as high as 661 mV.

Sputtering techniques can achieve a precise control of the composition of the deposited film. Brammertz and co-workers demonstrated this technique for a CZTSSe absorber.³³ Cu, Zn and Cu₁Sn₉ metallic precursors were sputtered on Mo-coated glass followed by selenization under H₂Se environment. The solar cell achieved a 9.7% efficiency with a V_{oc} = 408 mV and a J_{sc} = 38.9 mA/cm².

2.4 Challenging Aspects of Kesterite Solar Cells: Factors Affecting the V_{oc}

Even though the kesterite structure is derived from chalcopyrite structure, its solar cell efficiency is much lower than the best performing CIGSs containing devices. One of the most critical problems is the V_{oc} limitation. The calculated V_{oc} deficit is much higher than that of CIGSs solar cell, indicating that an additional recombination process occurs within the device.

2.4.1 V_{oc} Deficit Study from Current-Voltage-Temperature (JVT) Measurements of the Solar Cell Performance

In general, the V_{oc} of the kesterite solar cells is lower than that of CIGSSe devices although they share the same band gap. Gunawan and co-workers from IBM investigated this phenomenon by using current-voltage-temperature (JVT) measurements to extract the temperature influence to the V_{oc} and the dominated activation energy of the recombination of the solar cell.³⁴ The relation can be revealed by following equation:

$$V_{oc} = \frac{E_a}{q} - \frac{nkT}{q} \ln\left(\frac{J_{00}}{J_L}\right)$$

where E_a is the activation energy of the recombination, n is the diode ideality factor, J_{00} is the reverse saturated current pre-factor and J_L is the light current. When it is assumed that n , J_{00} , J_L are independent of temperature, the open circuit voltage and temperature can be plotted with an extrapolated line indicating the E_a at $T=0K$. As shown in figure 2-7, the E_a value from CIGS solar cell was equal to the band gap E_g calculated from external quantum efficiency (EQE), which indicated that the main recombination mechanism for CIGS solar cells occurs in the bulk of the CIGS absorber. However, for CZTSSe solar cells, the E_a was less than the band gap of CZTSSe. The authors suggested that a significant contribution to the recombination happened at the interface between the CZTSSe absorber and CdS buffer layer. Thus, the interface recombination suppressed the V_{oc} of the solar cell.

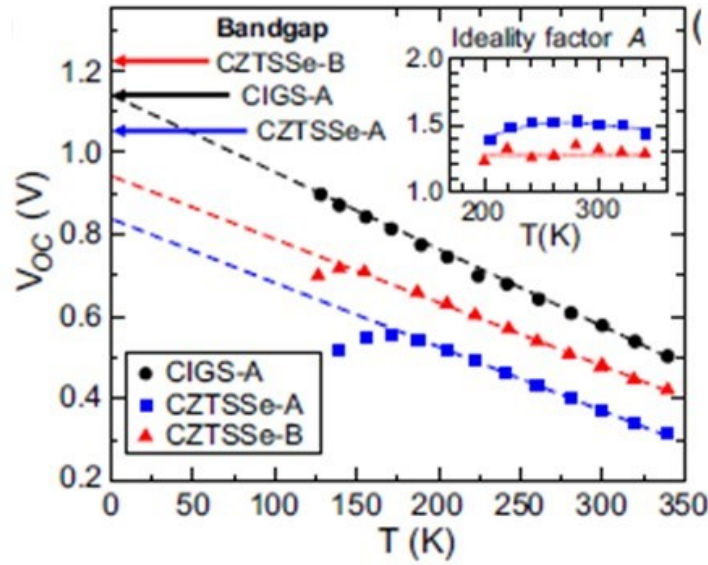


Figure 2-7 JVT analysis of hydrazine CZTSSe and CIGS solar cell ³⁴

This V_{OC} deficit phenomenon had also been observed from solar cells prepared using different fabrication processes. Brammertz and co-workers fabricated CZTSe absorber layers by sputtering metallic stacks followed by selenization. ³⁵ The JVT study of the solar cells showed a smaller E_a comparing to the E_g calculated from the EQE. However, it gave identical value to the photoluminescence (PL) transition energy. ³³ It advised that the carrier recombination condition could contribute to limit the V_{OC} . A further study by Redinger and co-worker observed the same relation between the extracted E_a and PL transition energy. ³⁵ They refined their PL peaks and extracted an E_a equal to the lowest PL transition energy, as shown in figure 2-8. They asserted this observation as evidence that the dominated recombination remained in the CZTSSe bulk. This study indicated that PL spectroscopy can be a useful tool to reveal the recombination behavior of the CZTSSe absorber and, to some extent, its influence on the V_{OC} of the solar cells.

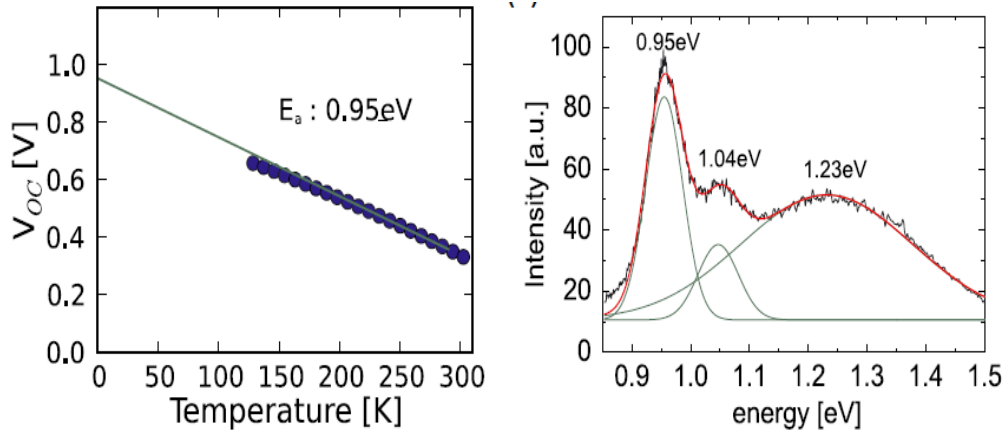


Figure 2-8 Extracted E_a from JVT measurement (left) and PL spectra with fitting from a CZTSSe absorber (right) ³⁶

2.4.2 Recombination study of CZTSSe Films by PL Spectroscopy

PL spectroscopy is a powerful tool to analyze the carrier properties in semiconducting materials. Many research groups have used this technique to investigate the CZTSSe thin films. Leitao and co-workers conducted a comprehensive PL study on highly crystalline CZTSSe, where temperature dependent and power dependent PL spectroscopy were used to investigate the recombination transition type. The authors observed a severe quenching effect of the PL intensity throughout the temperature dependent PL spectra, and a non-linear relation between the PL intensity and laser power (figure 2-9). Through the analysis, they concluded the carrier transition type was the donor-acceptor pairs (DAPs) transition. ³⁶ In addition, two thermal activation energies of non-radiative recombination were extracted from the fitting of luminescence intensity versus temperature. However, this analysis was based on a non-device quality CZTSSe film that might mislead the practical situation for a device quality CZTSSe absorber.

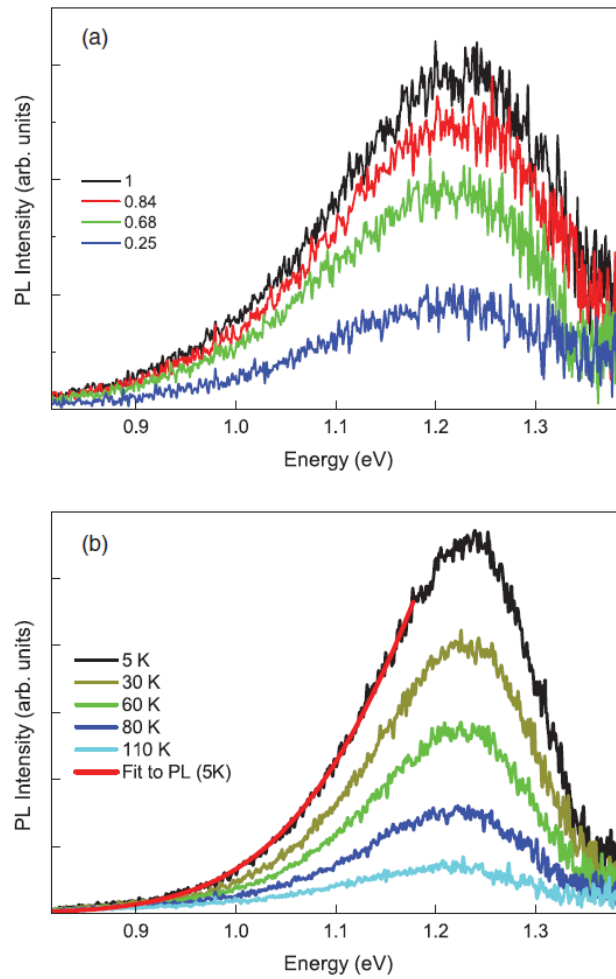


Figure 2-9 Power dependent a) and temperature dependent b) PL spectrum ³⁷

In addition, Grossberg and co-workers from Tallinn University of Technology applied the temperature dependent PL on their synthesized CZTSe monograin. ³⁸ The PL peaks from the monograin separated into three peaks, which were considered as different recombination transition types coexisting in the monograin. They observed a similar PL intensity quenching effect as the temperature increased and were able to calculate the thermal activation energy from individual peaks. Besides, they observed a remarkable blue shifting of the peak along with a reduction in temperature, as shown in figure 2-10. They attributed this observation to the band-to-impurity type carrier recombination that involved acceptor defect

levels in the CZTSSe. In a following study, they demonstrated a series of PL spectroscopy experiments on CZTSSe monograins with different S/Se ratios. The PL peak positions changed according to the S/Se ratio, which allowed them to calculate the average depth of potential fluctuation.³⁹

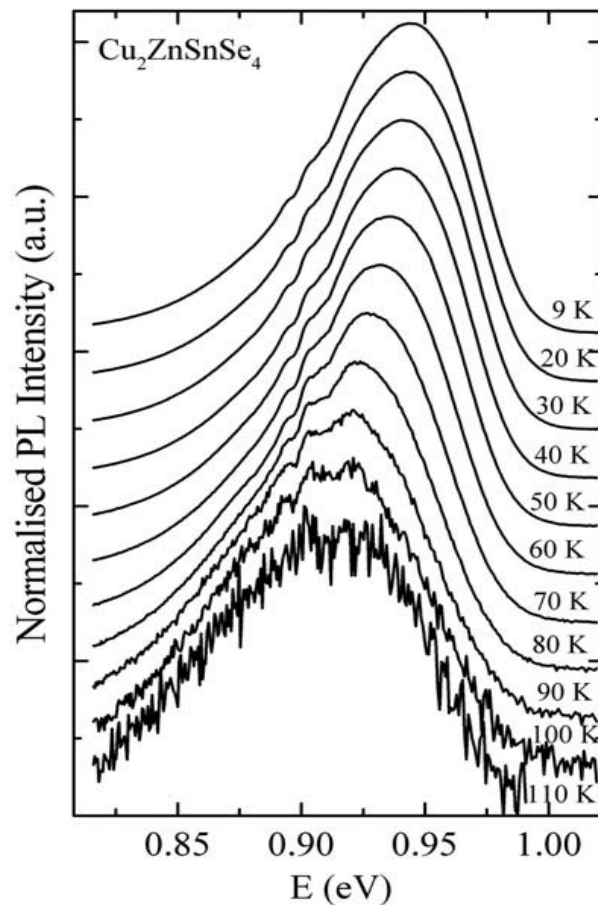


Figure 2-10 Temperature dependent PL spectra on a CZTSSe monograin³⁸

PL spectroscopy has also been used to identify the band gap of wurtzite CZTSSe nano-crystals. A broad emission peak was observed from the nanocrystals, which indicated its difference from the thin film study, possibly due to a quantum confinement effect. The peak shifting followed the same trend as for thin film CZTSSe with varying S/Se ratios.⁴⁰

Similar PL studies have been applied on various semiconductors such as CuInSe₂⁴¹, CIGSe⁴²⁻⁴⁴, GaAs⁴⁵⁻⁴⁶ and GaInP⁴⁷⁻⁴⁸, where it has proved itself as a promising technique for probing the electrical properties of semiconductor materials.

2.4.3 Electronic Structures Study of the Kesterite Materials and its Defects Complexity towards Chalcopyrite Materials.

Since 2009, Chen, Gong, Walsh, Wei and co-workers together have done invaluable studies on the simulation of the electronic structures of CZTSSe.^{11, 15, 49-53} Firstly, they calculated the CZTSSe electronic structures of the different crystal structures (kesterite, stannite and PMCA) using first principle theory.⁵⁴ Their procedures allowed them to calculate the lattice constants, tetragonal distortion parameters and the values of the direct band gaps with respect to pure CZTS and CZTSe. This work provided a first insight of the basic electronic parameters for the CZTSSe materials, as suggested that the kesterite structure type attained the lowest formation energy among the three structures. However, the formation energy gap of the crystal structure transformation was not large enough to prevent the other two structures coexisting as minority phases. They also found that the ordering of the Cu and Zn cations was weak. The presented band gaps of CZTS and CZTSe based on their calculations were 1.5 eV and 1.0 eV respectively, which were consistent with experimental values.^{13, 32} A subsequent study on the simulation of the structural and electronic properties of CZTSSe revealed a nearly linear relationship between the CZTSSe band gap and S/Se ratio. The band gap bowing factor was less than 0.1, as shown in figure 2-11.¹¹ This phenomenon was similar

with CIGS_{Se} materials ⁵⁵, giving a feasible principle to predict the band gaps of CZTS_{Se} by controlling the S/Se ratio.

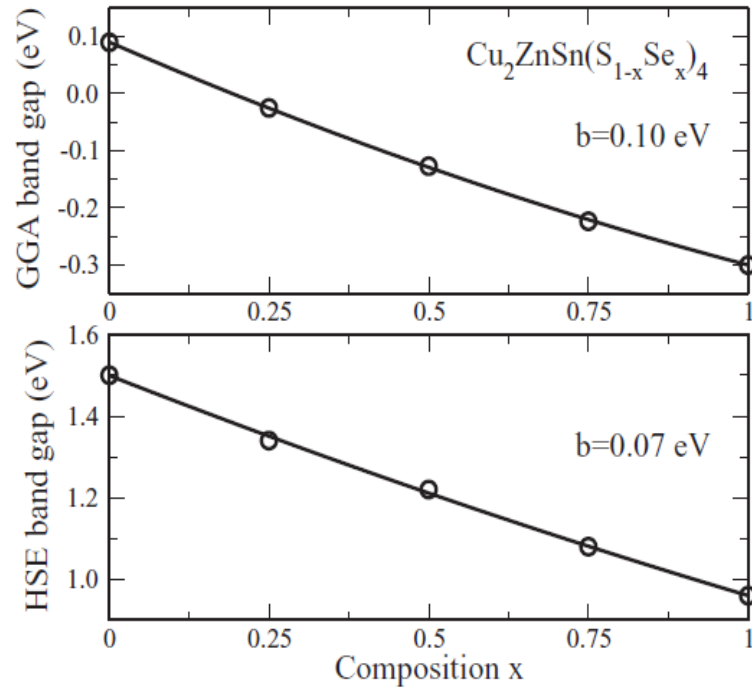


Figure 2-11 Band gap bowing effect with different S/Se compositions ¹¹

Furthermore, the relative band positions and band alignment were calculated. Figure 2-12 provided a clear visual representation of understanding the band alignment between the CZTS_{Se}, CIGS_{Se} absorbers and the CdS buffer layer. The red dashed line presented the pinning level for all chalcopyrite and kesterite materials. Considering the high position of the CZTS conduction band, they proposed that it could be very difficult to dope CZTS to n-type conductivity according the doping limit rules, with CZTSe offering a better alternative for n-type doping.

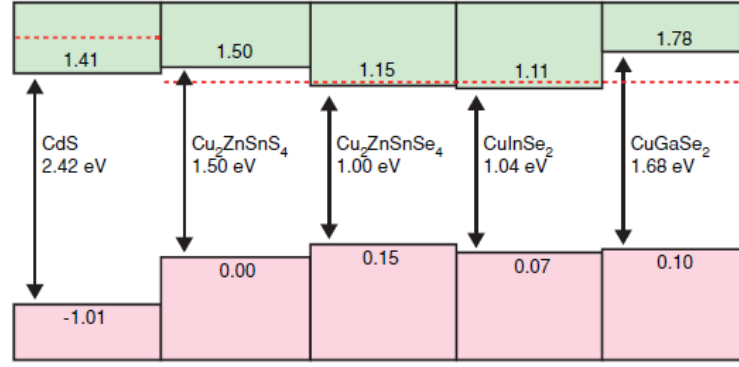


Figure 2-12 Band positions and alignment of semiconductors used in thin film solar cell ¹¹

The simulation work was also focused on the intrinsic defects and complexes existing in CZTS materials. ⁵² The transition-energy levels of the intrinsic defects in CZTS were calculated, and showed a complicated diagram as represented in figure 2-13. In this figure, V_{Cu} represented Cu vacancy, Cu_{Zn} represented the Cu to Zn anti-site and Cu_i represented the Cu interstitial defect in the lattice of CZTS. For kesterite material, Cu cation possessed +1 oxidation state, Zn cation possessed +2 oxidation state and Sn cation possessed +4 oxidation state. In this case, the Cu vacancy indicated an acceptor defect. For Cu to Zn anti-site, acceptor defect was also expected due to their different oxidation states. The Cu interstitial brought one additional charge to the lattice, resulting a donor defect formed near the conduction band. Similarly, the other defects could be derived and interpreted from difference of the cation oxidation states, so to be interpreted as donor and acceptor defects, as illustrated in the figure 2-13.

The shallow Cu vacancy defect possessed the lowest doping energy level. However, the relatively deeper Cu_{Zn} anti-site defects provided the lowest formation energy in CZTS system, which contributed to the intrinsic p-type

conductivity of the CZTS. As in CIGS system, the shallow Cu vacancy was dominating due to its lowest formation energy among all the defects. In addition, deep defects presented in CZTS could also contribute to the trapping of the minority carriers.

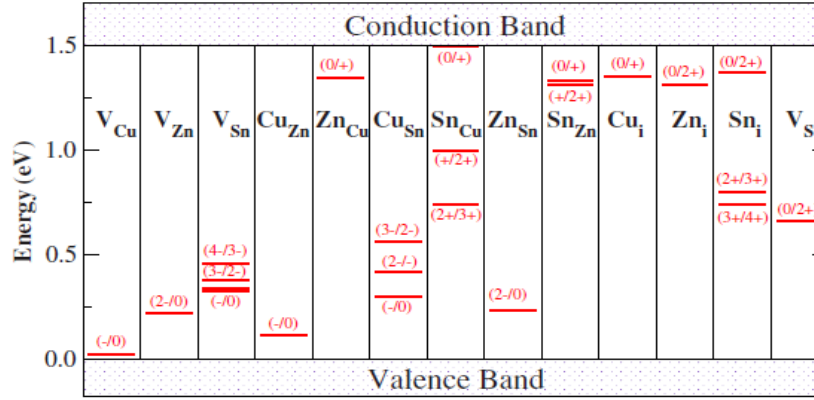


Figure 2-13 Defects energy level calculated in CZTS structure. ⁵¹

Due to the complexity of the CZTS system that three cations with different oxidation states are coexisting, some deep defects were easily formed in nonstoichiometric conditions. The deep defects could act as traps of free carriers or recombination centers, which led to reduce final solar cell efficiency. As Cu poor and Zn rich conditions were applied to fabricate the CZTS absorber, defects complexes, as pairs of the donor-acceptor defects, could also be formed in this nonstoichiometric CZTS films (figure 2-14). Charge compensation between donors and acceptors pushed the electron donor level up and the electron acceptor level down, so that the deep defects were eliminated and minimized. In this case, the defects complexes could give an electrically benign property for its passivation effect on the deep defects, similar to the passivation effect to the In_{Cu} antisite in CuInSe₂ material.

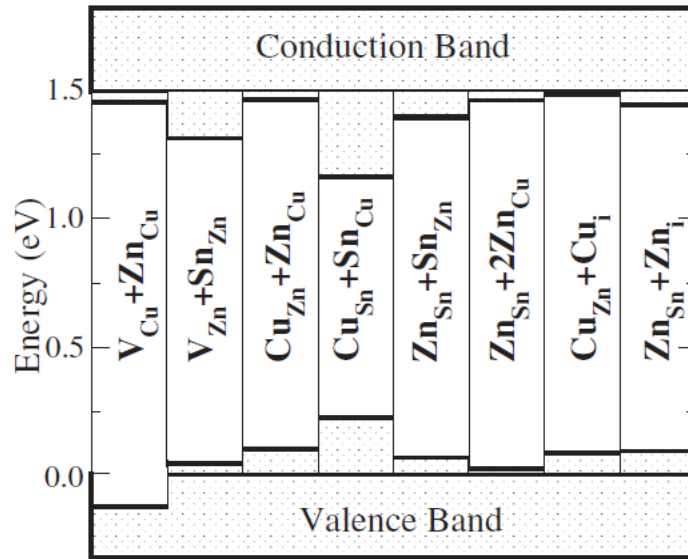


Figure 2-14 Compensated defects complexes calculated from nonstoichiometric CZTS ⁵¹

2.4.4 Impedance Spectroscopy on Solar Cells

Impedance spectroscopy is a powerful and novel technique to characterize the electrical properties and interface properties of electronic devices. ⁵⁶ The principle of this technique is based on the impedance measurement from the device under an alternating current (AC) conditions. The frequency of the AC power can be adjusted from several Hz up to MHz on the device. The electronic signal collected can be analyzed to reveal the carrier density, mobility and lifetime. Together with the constant direct current (DC) voltage provided, the signal can reflect the carrier changing properties at each point of the DC bias. A light bias can also be added into the system if the targeting devices are photo-sensitive. ⁵⁷ A temperature dependent study is more suitable for devices not involving phase changing, such as liquid to solid, in the system. It can be used to examine the dynamics of carriers or charges in the materials bulk or interface. This technique is suitable for studying a wide range of materials such as metals, semiconductors, electrolytes and even

insulators. Previous studies using this technique in the field of material science were mainly focused on the investigation of the interface between solid surface and electrolytes. Dye sensitized solar cells (DSSC) were well investigated by this technique to study the charge transportation and mobilization.⁵⁸⁻⁵⁹ Further development has been achieved by studying the solid-solid interface to illustrate the carrier behavior at the junction and bulk of the materials. However, to date, this method has not been well adopted to heterojunction solar cells. Some pioneering researchers have employed this method to Si solar cell⁶⁰, Organic photovoltaic (OPV)⁶¹, CdTe⁵⁷ and CIGS⁶² solar cells to provide some leads in this field.

Mora-Sero and co-workers demonstrated the application of the impedance spectroscopy on high efficiency Si solar cells.⁶⁰ In their work, they extracted the transport resistance R_{tr} and recombination resistance R_{rec} under different light intensities and different DC bias (figure 2-15). The R_{rec} was referring to the recombination resistance of the solar cell. The R_{rec} value was represented as the diameter distance of the full arc, along x-axis. For illustration, in figure 2-15(a), the R_{rec} for 0.2 sun was 10 ohm; in figure 2-15(b), it was 50 ohm.

The R_{rec} reduced significantly as the sunlight intensity increased at forward bias. The total resistance was significantly higher at a reverse bias of 0.5V compared to a forward bias of 0.2V. This was due to the reverse bias enlarging the width of the depletion region of the p-n junction, or in another words, it put up the electronic barrier for electron movement. This figure presented a good example of the spectra obtained from a high quality solar cell. The solar cell working principle can

be described from the varying of sunlight intensity and voltage bias, as these are the factors promoting the charge separation

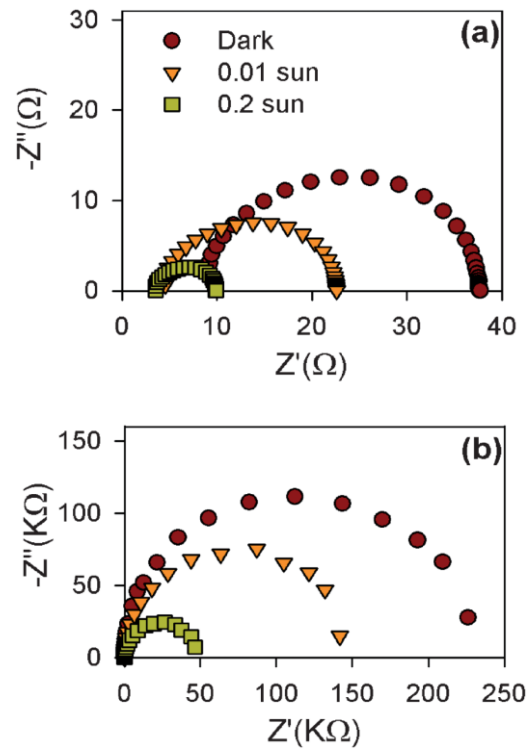


Figure 2-15 Impedance spectra of Si solar cell for different sunlight intensity at a) forward bias 0.2 V b) reversed bias 0.5 V ⁶⁰

This work also extracted the total resistance R_{dc} under different DC bias, as illustrated in figure 2-16. Under reversed bias conditions, the R_{dc} remained at high values, while as the DC bias increased in the forward bias region, the R_{dc} declined significantly. This result was mainly contributed by the R_{rec} as the R_s did not change significantly under any DC voltages investigated.

Both R_s and R_{rec} were parameters that described the impedance of the diode under certain voltage bias. They were used to describe the impedance behavior of a diode under different DC voltages and AC voltages with different frequency.

Under high frequency AC voltage, only R_s was observed where the depletion region was acting as a capacitor; while under low frequency AC voltage, the depletion region presented remarkable impedance to the charge flow, resulting high impedance value that equaled to the sum of $R_s + R_{rec}$. Here the R_s could be considered as material impedance to the charge flow, while the R_{rec} could be considered as the depletion region impedance to the charge flow.

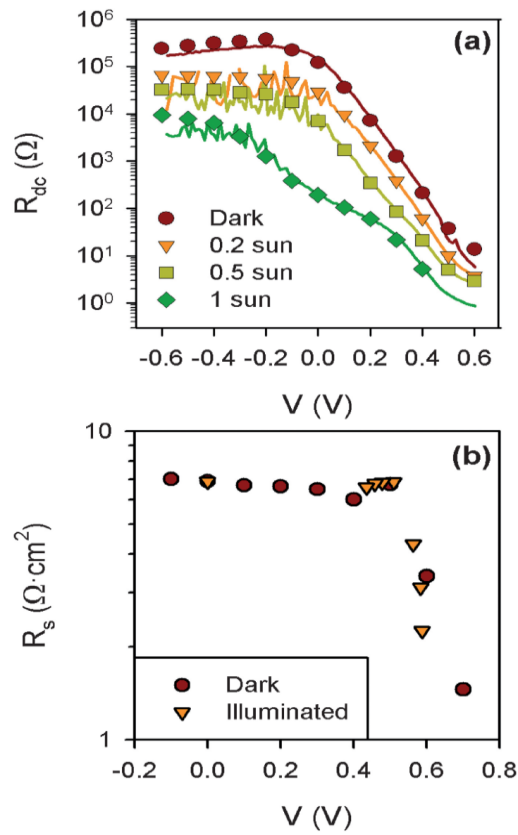


Figure 2-16 The Si solar cell (a) total resistance changed with applied DC bias (b) R_s changed with applied DC bias. ⁶⁰

As the R_{rec} was the recombination resistance of the solar cell, in this case, the solar cell could be considered as a simple diode. Under 0 V DC bias, the built-in electric field originated from the p-n junction was stronger than that under forward bias. When the forward bias was added to the diode, the depletion region width

was getting narrower and the current running through the diode was getting higher. Since the series resistance R_s was kept constant, as a results, the R_{rec} was smaller. Thus, the change of R_{rec} was due to narrowing of electronic barriers within the p-n junction, which was considered universal in a p-n junction solar cell.

Boix and co-workers conducted a detailed analysis of interface properties of organic-PV (OPV) devices by applying impedance spectroscopy (figure 2-17).⁶¹ They were focusing on the capacitance measurement for the heterojunction of the solar cell devices. Figure 2-17(a) showed that the capacitance varied with the changing frequency, indicating the response changing of the charge at the junction. The carrier density of the absorbers and the flat band potential of the devices were both extracted from the measured data using the Mott-Schottky equation:

$$C^{-2} = \frac{2(V_{fb} - V_{appl})}{A^2 q \epsilon \epsilon_0 N}$$

where V_{fb} is the flat-band potential, V_{appl} is the applied bias, A corresponds to the cell area, ϵ is the relative permittivity of the blend, ϵ_0 represents the vacuum permittivity and N is the carrier density of blend. The Mott-Schottky relation was used to describe the interface/junction property involving charge separation and transportation. The junction of the solar cell could be considered a capacitor. By applying AC voltages with different frequencies, the material carrier concentration could be calculated out. The experiment helped to study the junction properties of the solar cells, such as the OPV device tested here. The Mott-Schottky relation plot was illustrated in figure 2-17(b), in which the reduction in forward bias (V_{bias}) was

used to extract the flat band potentials, and the declining slope indicated the carrier concentrations of the absorbers in the OPV device.

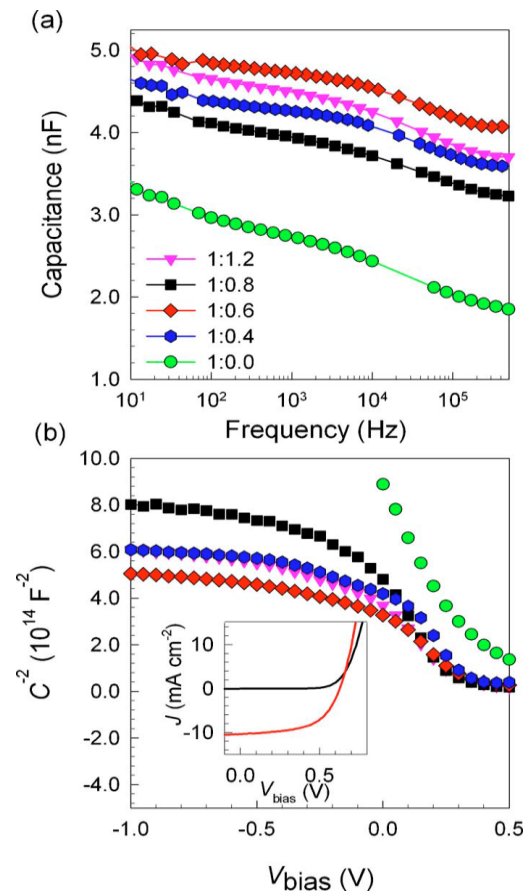


Figure 2-17 The Si solar cell (a) capacitance spectra at 0 applied DC bias with different blend composition (b) Mott-Schottky relation derived from impedance spectra

The research work based on impedance spectroscopy on CIGS and CdTe were focused on the design of equivalent circuit to match the device performance. However, the complexity of the circuit match did not present a clear understanding of the energetics of the solar cell.⁶³ The solar cell performance was not linked to the solar cell impedance analysis.

Chapter 3 Experimental

This chapter focuses on the experimental details of CZTSSe absorber fabrication and solar cell characterization. In addition, photoluminescence and impedance spectroscopy are introduced and described, as both of these techniques were utilized to characterize the optical and electrical properties of the CZTSSe absorber.

3.1 Kesterite Solar Cell Fabrication and Measurement

3.1.1 Spray Pyrolysis of CZTS on Mo-Coated Glass

Precursor solutions were prepared by dissolving copper chloride dihydrate $\text{CuCl}_2 \cdot 2\text{H}_2\text{O}$ (Sigma-Aldrich, ACS reagent, 2.8 mmol, 476 mg), zinc chloride ZnCl_2 (Sigma-Aldrich, ACS reagent, 19.5 mmol, 266 mg), tin chloride dihydrate $\text{SnCl}_2 \cdot 2\text{H}_2\text{O}$ (Sigma-Aldrich, reagent grade, 1.58 mmol, 356 mg) and thiourea (TU, Sigma-Aldrich, ACS reagent 28mmol 2.13g) into deionized water (150ml). The solution was adjusted to a PH of 2 by addition of HCl solution. The pH is equal to 2 with careful measurement by pH meter, which is calibrated under acidic standard solution before use. The error is within 0.1. The solution was stirred for 2 minutes before use. All the chemicals were purchased from Sigma Aldrich, without further purification.

The spray pyrolysis setup is shown in figure 3-1. Nitrogen gas was used as carrier gas and controlled by a gas regulator. The airbrush was connected to precursor solution with plastic tube and the pressure for spraying was 4 bar. The spray rate was adjusted to 3ml/min, so the total spray time was 50 minutes. The

solution was sprayed onto Mo-coated glass substrate, which was pre-fabricated by sputtering Mo on soda lime glass. The substrate was preheated to 160°C, which was slowly increased to 280°C over a period of 5 minutes after initiation of the spraying. The substrate temperature was controlled by ceramic hot plate (Thermo scientific StirTrac) and surface temperature was calibrated with thermocouple. The distance between the nozzle and substrate was approximately 30 cm. After finishing the deposition, the samples were cooled in atmosphere and stored without further purification and cleaning.

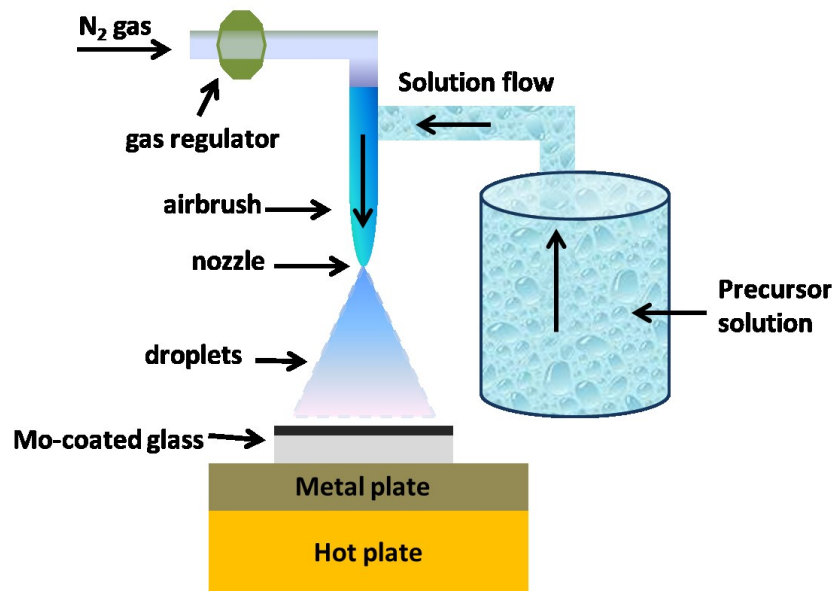


Figure 3-1 Setup of spray pyrolysis for CZTS film deposition

3.1.2 High Temperature Selenization of CZTS Film to Form CZTSSe Absorber

The CZTS films were subjected to high temperature selenization in tube furnace shown in figure 3-2. The temperatures for selenization were set to 500-540°C. Se pellets (30 mg, Sigma-Aldrich) were used as the Se source and quartz tube was used

to isolate the system from the atmosphere. The tube was pre-evacuated and refilled with Ar gas three times to ensure an inert gas protective environment. The quartz tube was sealed at one end and placed inside in a larger quartz tube, where the Ar gas flow was mainly through the larger tube. The gas flow inside the large tube was adjusted to 10 sccm to maintain the Ar environment. The ramping rate for selenization was 0.6°C/s. The post selenized film was furnace cooled to room temperature.

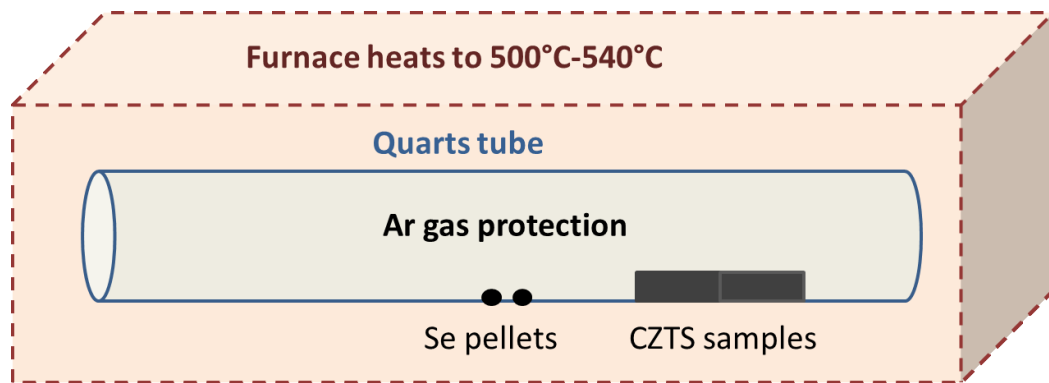


Figure 3-2 Setup for high temperature selenization of CZTS to form highly crystalline CZTSSe

3.1.3 Device Fabricated on Top of CZTSSe

A 50 nm CdS layer was deposited on top of CZTSSe by chemical bath deposition (CBD). Cadmium acetate (Sigma-Aldrich, ACS reagent, 0.4 mmol, 92 mg) was added to 200 ml deionized water with stirring. Ammonium acetate (Sigma-Aldrich, BioUltra, 4 mmol, 308 mg) and thiourea (Sigma-Aldrich, ACS reagent 2mmol 152mg) were added sequentially to the solution. The solution was stirred for 3 minutes and ammonium solution (Sigma-Aldrich, BioUltra) was added dropwise to adjust the solution to a PH of 9. The CZTSSe film was then taken out from selenization furnace and transferred to the CBD solution within a time period of 2 minutes. The solution

was capped and merged into a water bath preheated to 80°C with continuous stirring. The deposition was carried out for 10 minutes, and then the film was taken out and washed immediately using cold DI water. The films were then blown with N₂ gas and stored in a dry box.

The CdS coated films were taken in to the sputtering machine for intrinsic ZnO (i-ZnO) and ZnO:Al (AZO) deposition. 50 nm i-ZnO and 400 nm AZO were coated on top of CdS by RF magnetron sputtering. Ni/Al was used as front electrode. 300 nm Ni and 400 nm Al were deposited by thermal evaporation.

3.1.3 Solar Cell Measurement

The solar cell was measured under 1.5 AM sunlight conditions using a San-EI Electric, XEC-301S solar simulator. A Keithley source meter (2612A) was used to program the measurement and calculate the power conversion efficiency. The light intensity was calibrated using a standard Si solar cell (Fraunhofer) to 100mW/cm². The external quantum efficiency (EQE) was measured using a PVE300 Photovoltaic Devices Characterization System (Betham) with dual Xenon/quartz halogen light source, which was pre-calibrated using Si and Ge standard cells before measurement. The measurement conditions used were an interval of 5 nm and a scan rate of 5nm/s. The electrode area is 0.01cm² while the active area is at 0.12cm². The cell area is measured by SEM.

3.2 Characterization of CZTSSe Thin Film

The morphology of the CZTS and CZTSSe film was observed using a field emission scanning electron microscopy (JOEL, FE-SEM, JSM-7600). The composition of the films was monitored using an energy dispersive X-ray spectroscope (EDS, Oxford), equipped as part of the FE-SEM system. The crystallographic structure of the film was investigated by X-ray diffraction (XRD, Bruker-AXS D8) in thin film mode. The incident X-ray angle was 4° with $\text{CuK}\alpha$ radiation ($\lambda=0.1542 \text{ nm}$). Raman spectroscopy was conducted using a Raman microscope (WiTec Alpha 300) equipped with $100\times$ microscope objective lenses (Nikon, Japan) and a piezo scanner. The laser used was 488 nm He-Ne laser ($\lambda=488\text{nm}$) (Coherent Inc., Santa Clara, CA) with a power density of $200 \mu\text{W}/\text{cm}^2$, and a 3 time scanning average mode.

Micro-PL spectroscopy was carried out using continuous wave diode laser with 532nm excitation wavelengths. By applying an objective lens (Nikon CFI60 Lu Plan Epi ELWD), the laser beam was focused on an area with less than a $10 \mu\text{m}$ diameter. The laser power was controlled in the range from $100 \mu\text{W}$ to 10 mW . For temperature-dependent PL, the sample was placed in a cryostat and the temperature control was achieved using liquid He or N_2 ranging from $6\text{-}300\text{K}$. All PL signals were collected by an InGaAs array detector (Princeton Instruments OMA V) attaching to a monochromator (Princeton Instruments Acton Series SP2300) equipped with a $150\text{g}/\text{mm}$ grating blazed at 500 nm (Princeton Instrument).

Time resolved photoluminescence (TRPL) spectroscopy was used to measure the minority carrier lifetime in CZTSSe absorber. Picosecond pulsed diode laser with pulsed width of 68 ps (FWHM) was used as the power source. The laser

wavelength is 638 nm. Near infrared photomultiplier tube (NIR PMT) detector together with spectrometer were used to detect the signal. Time-correlated single photon counting (TCSPC) was used to analyze the fluorescence photon with a limiting differentiation time of 40 ps.

3.3 Impedance Spectroscopy on Kesterite Solar Cell Devices

Impedance spectroscopy was carried out on the prepared solar cells using an Autolab PGSTAT128N. The measurements were performed in dark conditions with a scanning intermittent DC potential varying from -0.75 V to 0.75 V at 0.05 V. The AC signal was fixed to 20 mV with frequency sweeping from 400 KHz to 10 Hz at each DC bias. The obtained Nyquist plot was fitted with an equivalent circuit, with data fitting achieved in the software Z-View.

Chapter 4 Solution Processable CZTSSe

Absorber Development and Characterization

In this chapter, the crystal structure and morphology of CZTS and CZTSSe films obtained from chemical spray pyrolysis and selenization are analyzed. Secondary phases and elemental distribution are discussed in relation to obtaining high quality absorber films for light harvesting. The CZTSSe absorbers are used to fabricate solar cells and conduct further optical and electrical characterization. A comparative study of the performance of the fabricated solar cell under different conditions is described. A high power conversion efficiency was obtained and analyzed accordingly.

4.1 Morphology Analysis and Phase Identification of CZTSSe Thin Film

4.1.1 Investigate Acidic Effect on CZTS Morphology and Crystallinity Growth

In the initial stages of this work no aqueous-based chemical spray pyrolysis fabrication technique for device quality CZTSSe absorbers was available. In principle, this technique possesses a range of advantages such as residue free and scalable process, and the details of which were discussed in the introduction chapter. This technique had been successfully applied to fabricate CISSe absorbers where a 6% efficiency was achieved.⁶⁴ However, the problem encountered for CZTS spray pyrolysis was the solubility of Sn salts which allows the particles to be

dissolved in a precursor solution. A white precipitate was observed when SnCl_2 was added to water. Therefore, it was difficult to deposit a uniform and compact thin film. Kumar and co-workers applied a spray pyrolysis technique to deposit CZTS thin film under various spraying conditions.^{65 66 67} However, the uniformity of deposited film was not sufficient for further solar cell fabrication. In addition, no solar cell efficiency was reported by these researchers. In this work, this problem was addressed by the introduction of certain concentration of HCl into the Cu^{2+} , Sn^{2+} and Zn^{2+} precursor solution, which enabled the precipitates to be dissolved. The precursor solution was transparent before spraying on the Mo-coated glass and the as-deposited films comparison was illustrated in the FE-SEM image shown in figure 4-1. Without HCl treatment, the precursor solution particles were imbedded in the as-deposited CZTS film with a diameter greater than 2 μm . From the cross-sectional view, it could also be observed that the surface was very rough with the particles protruding from the top of the film. This film quality is not suitable for fabricating thin film solar cell, as shunting effect is highly expected from the thinner part of the film. And the particles can also acting as shunting center for the whole device, as the EDS spectra revealed that the composition of the particle is Sn and Cu rich. However, as the HCl solution was added, no particles were observed from the top and cross-sectional view of the films. During the pyrolysis process, the temperature was more than 270°C, so that all the water and HCl were evaporated, and the thiourea was also decomposed at this temperature too.⁶⁸ Thus, it led to CZTS film formation with near amorphous status. The film appeared very compact and uniform and was considered suitable for further device fabrication. In addition, the EDS spectra indicated elemental ratios of

$\text{Cu}/(\text{Zn}+\text{Sn})\approx 0.72$ and $\text{Zn}/\text{Sn}\approx 1.27$ in average, which was also considered suitable for absorber fabrication.

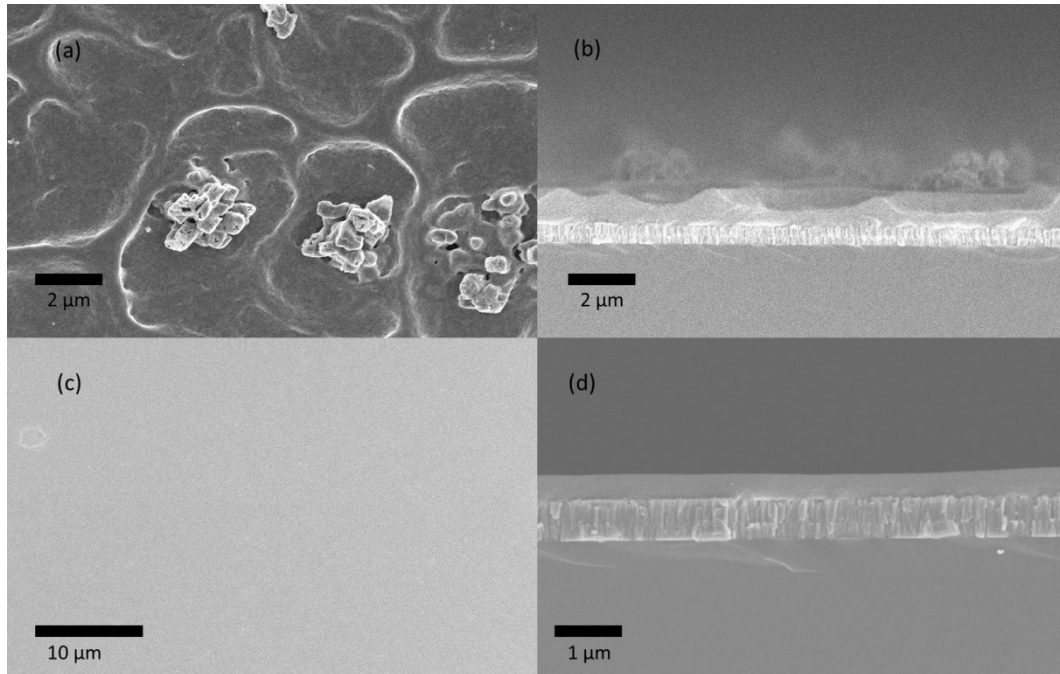


Figure 4-1 (a) Surface FE-SEM imaging of CZTS film without HCl precursor solution treatment (b) cross-section FE-SEM imaging of CZTS film without HCl precursor solution treatment (c) Surface FE-SEM imaging of CZTS film with HCl precursor solution treatment (d) cross-section FE-SEM imaging of CZTS film with HCl precursor solution treatment

After deposition, the CZTS film was selenized at 520°C under a selenium atmosphere with Ar protection. A highly crystalline CZTS_{Se} film was observed from FE-SEM images (figure 4-2), with no pinholes or cracks observed in the film. Grain sizes up to 500 nm could be obtained with good adhesion to the Mo layer. As no organic solvent was used in the precursor solution, there was no traceable carbon layer formed at either the front or back surface of the CZTS_{Se} film. The film composition detected by EDS was $\text{Cu}/(\text{Zn}+\text{Sn})\approx 0.75$ and $\text{Zn}/\text{Sn}\approx 1.15$. Zn and Sn loss was observed during the selenization process, and was attributed to the elemental

sublimation phenomenon at high temperatures.⁶⁹ This ratio was considered to be in the functional range of device quality absorber. Therefore, the attained CZTSSe film was used for further analysis and solar cell fabrication.

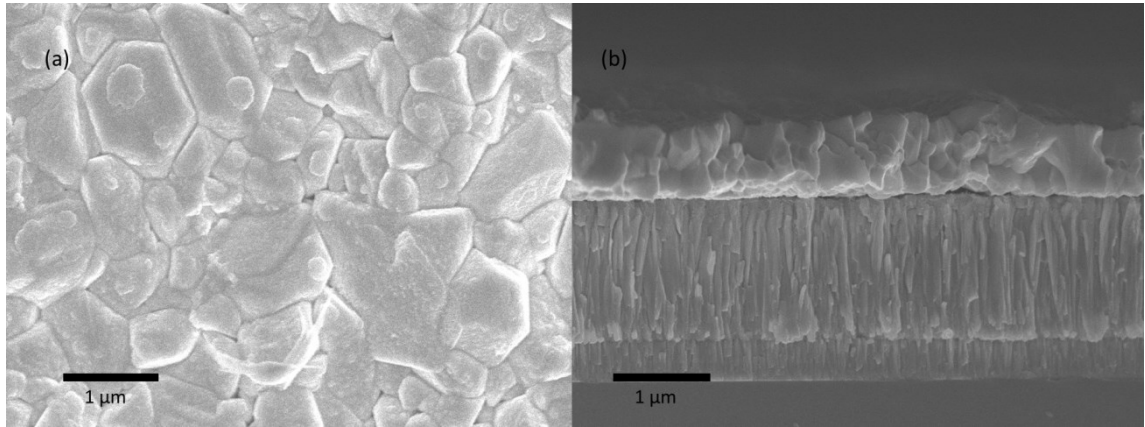


Figure 4-2 (a) FE-SEM top view of post-selenized CZTSSe (b) FE-SEM cross-sectional view of posted CZTSSe

4.1.2 Phase Analysis and Elemental Distribution Discussion on CZTSSe Thin Film

Phase analysis is critical for CZTSSe absorber fabrication, as any coexisting secondary phases would be detrimental for further solar cell performance. X-ray diffraction was firstly used to examine the crystal structure of as-deposited CZTS and post-selenized CZTSSe films. As shown in figure 4-3, the as-deposited CZTS XRD patterns showed nearly amorphous form with broad diffractions at $2\theta=28.6^\circ$, 47.4° , 56.2° and 58.7° . These diffractions corresponds to the (112), (220/024), (312/116) and (224) lattice planes, which match the XRD pattern for a kesterite-type structure. The diffraction at $2\theta=40.5^\circ$ corresponds to the Mo layer. After high temperature selenization, the diffractions become sharper and more defined due to enhanced crystallization. The diffraction position to lower angle because of the replacement

of S (Ionic radius = 1.84 Å) by Se (Ionic radius = 1.98 Å), indicating the larger unit cell for the latter. The diffractions from the (011), (110), (013) and (221) planes were also observed. This pattern gives robust confirmation of the desired kesterite-type phase. However, due to the possible secondary phases such as ZnS(Se) and CTS(Se), which display diffraction positions overlapping with those for a kesterite structure, further verification by Raman spectroscopy was also conducted.

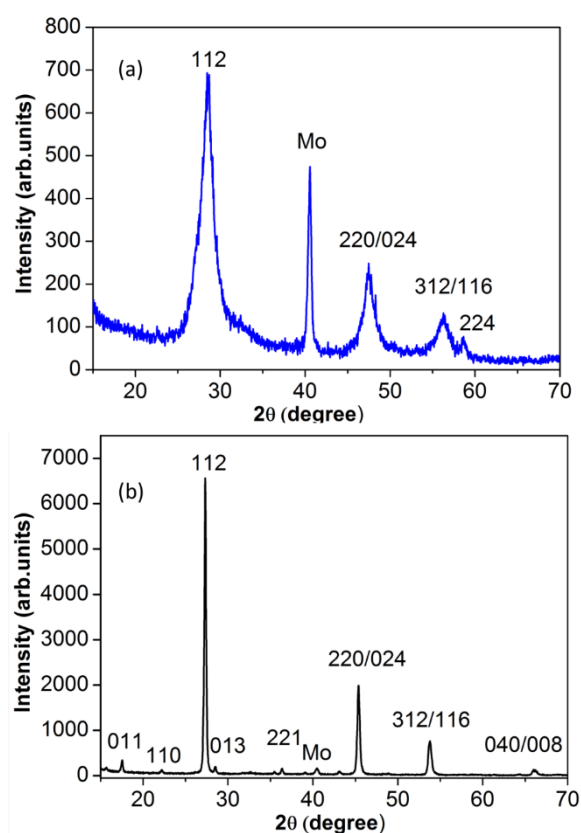


Figure 4-3 XRD curves of (a) as-deposited CZTS (b) XRD curves of post-selenized CZTSSe

As shown in figure 4-4, an as-deposited CZTS film reveals an A_1 mode shift at 333 cm^{-1} which is consistent with the literature value.¹⁴ After selenization, the bands shift at 173 cm^{-1} , 195 cm^{-1} and 235 cm^{-1} were clearly observed that were corresponding to the A_1 mode of CZTSe. The small band located at 328 cm^{-1} indicated that a small amount of CZTS remained after selenization. The shift of CZTS

band from 333 cm^{-1} to 328 cm^{-1} was originated from the two-mode behavior of the lattice vibration. This phenomenon has also been observed from CISSe crystals.⁷⁰ In these spectra, bands originating from secondary phases were not observed. It was worth noting that the absence of ZnS and ZnSe peaks from the Raman spectra indicated a good formation of pure phase CZTSSe. Based on the first principle calculations, the kesterite structure possesses a much lower formation enthalpy than the other possible secondary phases.^{49, 71} In this work, as the film composition was Zn rich, Cu and Sn poor, the secondary phases apart from zinc chalcogenide did not co-exist in the final film after high temperature selenization. Therefore, it revealed the formation of pure phase CZTSSe within the Raman spectroscopy detection depth from the surface to the bulk of the film. This sample presented a Se-rich CZTSSe, which is considered as “control sample” for further study.

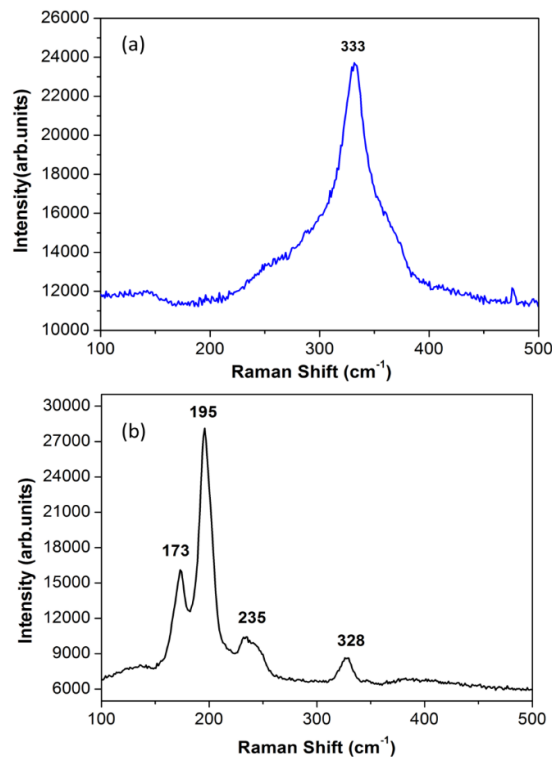


Figure 4-4 Raman spectra of (a) as-deposited CZTS film (b) post-selenized CZTSSe

The CZTSSe film with thickness of 600 nm was also studied using secondary ion mass spectroscopy (SIMS) depth profile measurement (figure 4-5). The Cu, Sn and Se were distributing uniformly across the film, while the Zn and S signals increased towards the Mo back contact. This increment indicates the possibility of ZnS(Se) coexisting at the Mo/CZTSSe interface. This phenomenon has also been reported by other research groups.⁷² It is believed the segregated phase at the back contact has no detrimental effect to the solar cell performance, and rather than acts as a dark region in the film.⁷³ In addition, no carbon signal was observed from the SIMS measurement even though thiourea was introduced as the sulfur source of CZTS. The metal-thiourea complexes evidently decomposed and evaporated at the spray temperature, leaving no carbon residue behind. Therefore, based on the absence of the carbon layer from the cross-section FE-SEM image and absence of EDS and SIMS carbon signals, it can be concluded that a carbon free absorber was attained with the spray pyrolysis technique used.

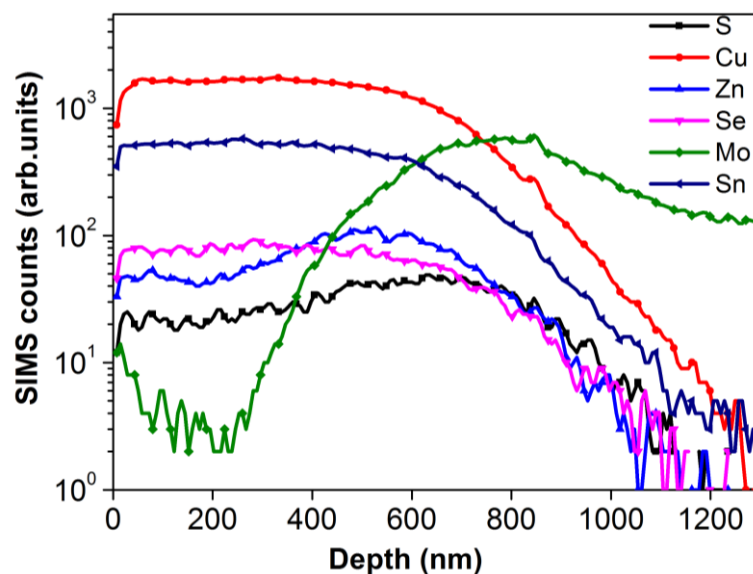


Figure 4-5 SIMS depth profile on CZTSSe thin film grown on Mo-coated glass

4.2 Solar Cell Performance (J-V and EQE) Discussion with Different Se Concentration in CZTSSe

Using the control samples, typical thin film solar cells were fabricated with the architecture of glass/Mo/CZTSSe/CdS/i-ZnO/AZO/Al, using the procedure described the in the experimental section. The cross-sectional FE-SEM image is shown in figure 4-6, and indicates the thickness of the CZTSSe absorber is approximately 600 nm.

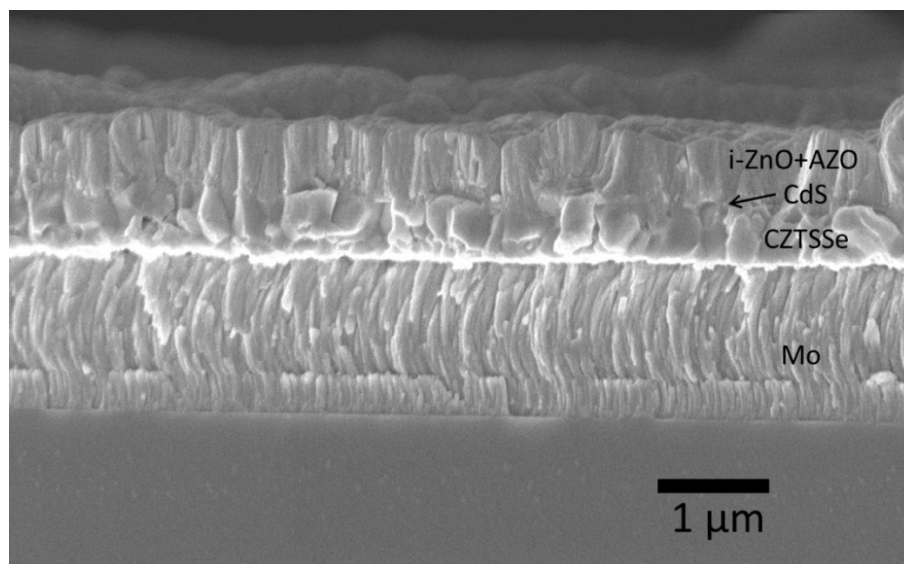


Figure 4-6 Cross-section FESEM image of total device with layers labeled

The J-V measurement under one sun AM 1.5 illumination generated a 5.1% PCE with $V_{oc} = 370$ mV, $J_{sc} = 27.3$ mA/cm² and FF = 50.6% (figure 4-8). The low V_{oc} value is primarily attributed to the Se-rich CZTSSe absorber, which was characterized by XRD and Raman spectroscopy. To further control the band gap of the absorber, experimental procedures were performed with reduced Se concentrations in the selenization process. Raman spectroscopy was used to evaluate the Se

concentration inside the low-Se-content CZTSSe absorber by direct viewing the A_1 mode peaks shift. Illustrated in figure 4-7, two broad bands were observed with Raman shift at 212 cm^{-1} and 329 cm^{-1} . Comparing the Raman spectrum from the control sample in figure 4-7, no clear CZTSe peaks are observed and band position shifts to 212 cm^{-1} , presumably due to the influence of the decreased Se concentration. This bi-model shift indicates a higher S/Se ratio for the low-Se-content sample compared to that for the control sample. As a result, a similar solar cell PCE was attained from the low-Se-content sample with higher $V_{oc} = 426\text{ mV}$ and lower $J_{sc} = 24.42\text{ mA/cm}^2$, compared to the control device, with the FF remaining 50%. The J-V plot is illustrated in figure 4-8 with the major parameters displayed in the inset.

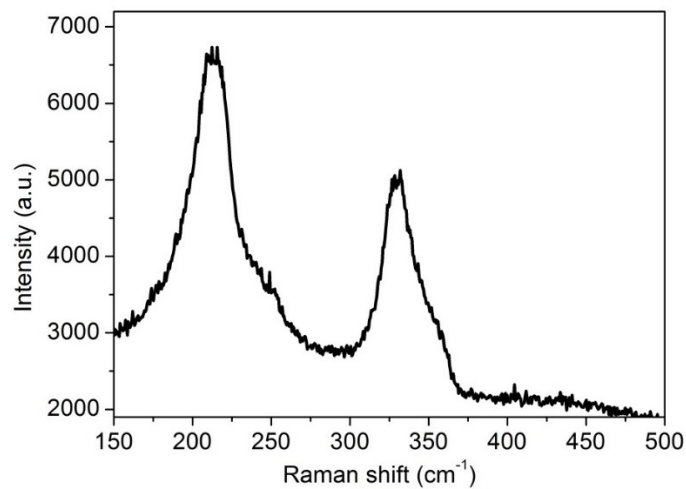


Figure 4-7 Raman spectrum of low-Se-content CZTSSe

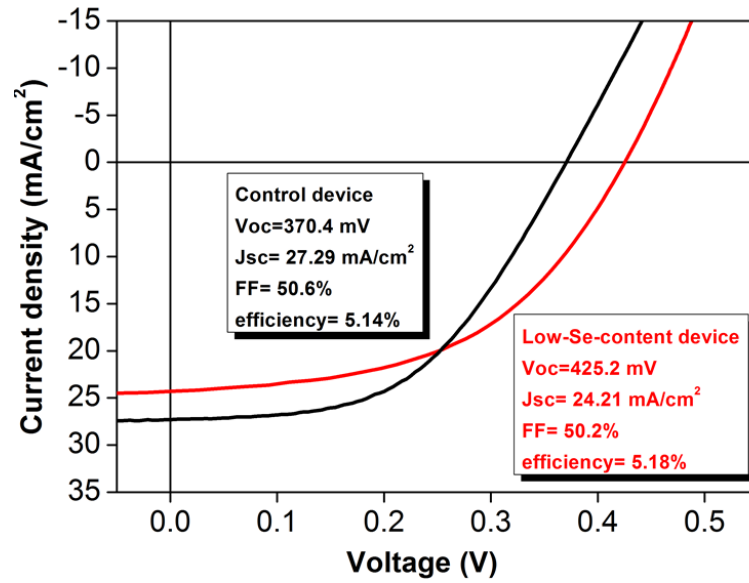


Figure 4-8 light J-V curves of control device and low-Se-content device

These two cells were taken to the external quantum efficiency (EQE) measurements shown in figure 4-9. The plots clearly show the different absorptions ending at a longer wavelength range. The band gaps E_g were calculated by plotting $[E \ln(1-EQE)]^2$ versus E . The control sample cell had $E_g=1.07$ eV while the low-Se-content cell had $E_g=1.21$ eV. As stated in the literature review, pure CZTS had $E_g \approx 1.5$ eV and pure CZTSe had $E_g \approx 1.0$ eV. Linear relation of S/Se content corresponding to E_g was observed in CZTSSe.⁴⁰ Therefore, as expected, the band gap values calculated from EQE plot are consistent to the Se concentration in each CZTSSe absorber. The short circuit current was also calculated by integrating the current from the EQE spectra. The calculated J_{sc} was 25.81 mA/cm^2 and 23.67 mA/cm^2 for the control device and the low-Se-content device, which were a little smaller than the J_{sc} at the one sun AM1.5 condition. It indicated that the device yielded less under low irradiance. The corrected efficiencies based on the integrated J_{sc} were 4.89% and 5.05% respectively.

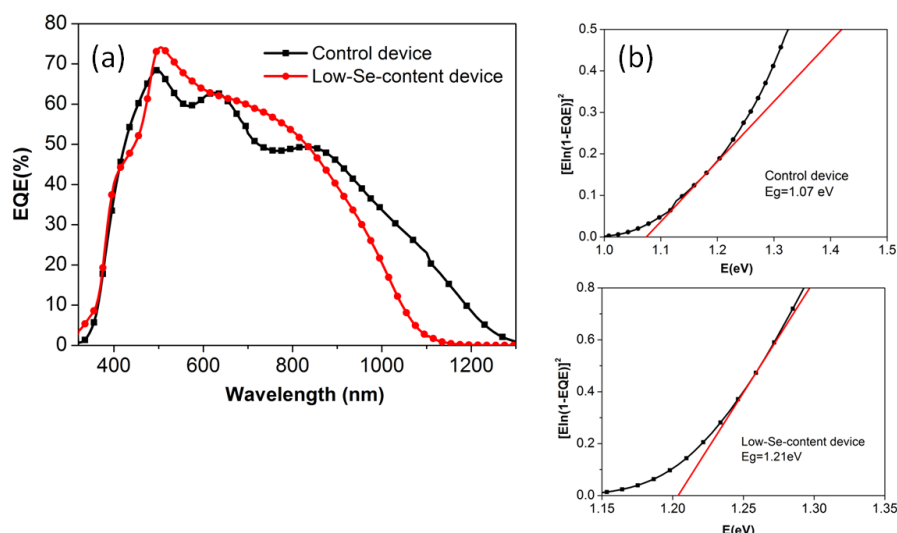


Figure 4-9 (a) EQE plot of control cell and low-Se-content cell. (b) Band gap plots of both solar cells.

It is worth mentioning that the optimized thickness for CZTSSe absorber was approximated 2 μm and so far, the highest kesterite solar cell efficiency reported possessed a higher temperature up to 540°C for the selenization process. Therefore, further efficiency improvement was attempted by adjusting the CZTSSe absorber thickness and selenization temperature, with the other process parameters unchanged.

The absorber thickness was firstly enlarged to 900 nm with the selenization temperature kept constant at 520°C. The selenium amount used was varied from 30mg to 50mg, aiming to deliver different Se concentrations to the CZTSSe absorbers while the other parameters remained the same. Figure 4-10 shows the solar cells based on these CZTSSe absorbers delivered a very similar PCE around 5.9% with V_{oc} in the range of 387-406 mV, J_{sc} in the range of 28.5-25.3 mA/cm^2 and FF in the range of 55-60%. As expected, the Se concentration in the CZTSSe

absorber had great effect on the V_{oc} and J_{sc} of the solar cells, due to its influence on band gap tuning of CZTSSe. Surprisingly, all the light J-V plots crossed the identical maximum efficiency point at $V_{mp} = 280$ mV and $J_{mp} = 21.1$ mA/cm². This phenomenon indicates the tradeoff effect of the voltage and current in the solar cells by introducing different Se concentration. In this case, it is considered that the band gap of CZTSSe was not the primary factor influencing the conversion efficiency for our devices. Therefore, to further improve the solar cell performance, the absorber layer thickness was increased beyond 1 μ m. The thicker absorber is believed to suppress the shunting behavior of the solar cell while optimizing the current generation.

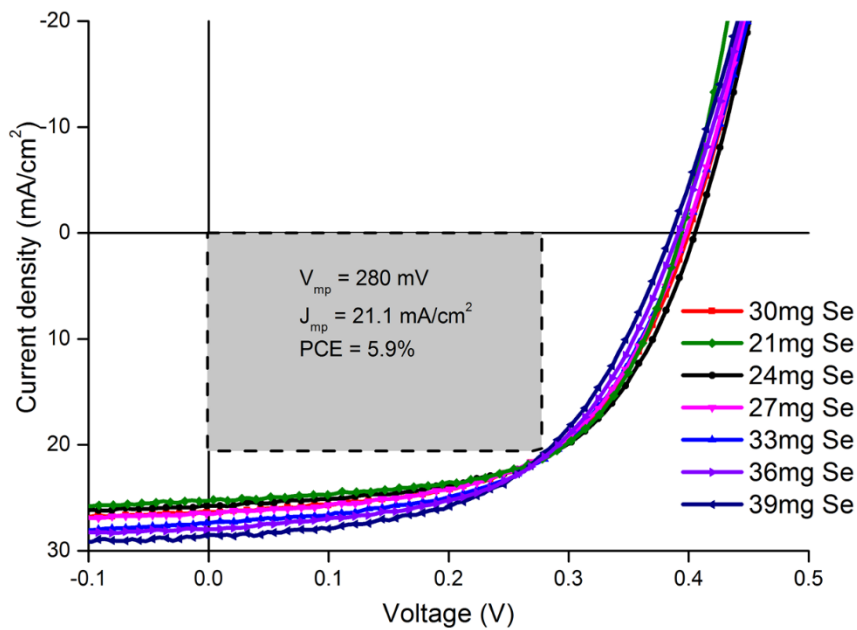


Figure 4-10 Light J-V plot of solar cells with varying Se concentration in the absorbers, the amount indicted in the figure referred to the adding amount of Se pellets during selenization.

However, further increases of the absorber thickness to 1.3 μ m did not produce large grain size in the film with the selenization temperature remaining at 520°C.

Small grains were observed with diameters less than 300 nm. Consequently, the PCE dropped to the level of 4-5%. This detrimental result can be attributed to the high series resistance of the small grains that consumed the light current and limited the FF. The recombination occurring at the grain boundary suppressed the voltage. Therefore, the selenization temperature was further adjusted to 540°C to pursue a better crystallinity of CZTSSe absorber.

So far, the highest PCE of 7.5% was obtained with absorber thickness at 1.3 μm and selenization temperature of 540°C. The cross-sectional SEM image shown in figure 4-11(a) reveals large grains size above 1 μm existing in the film. The solar cell performance is shown in figure 4-11(b) with $V_{oc} = 427 \text{ mV}$, $J_{sc} = 28.7 \text{ mA/cm}^2$ and $FF = 61\%$. The band gap calculated from EQE in figure 4-12 is 1.16 eV. The J_{sc} calculated from integrating EQE current was 28.1 mA/cm^2 , leading to a drop of the efficiency to 7.35% of the solar cell.

Compared to the previous solar cells, the V_{oc} and FF improve significantly. This can be attributed to the high crystallinity of the CZTSSe absorber. Furthermore, the optical and electronic origins of this improvement will be discussed later in chapters 5 and 6.

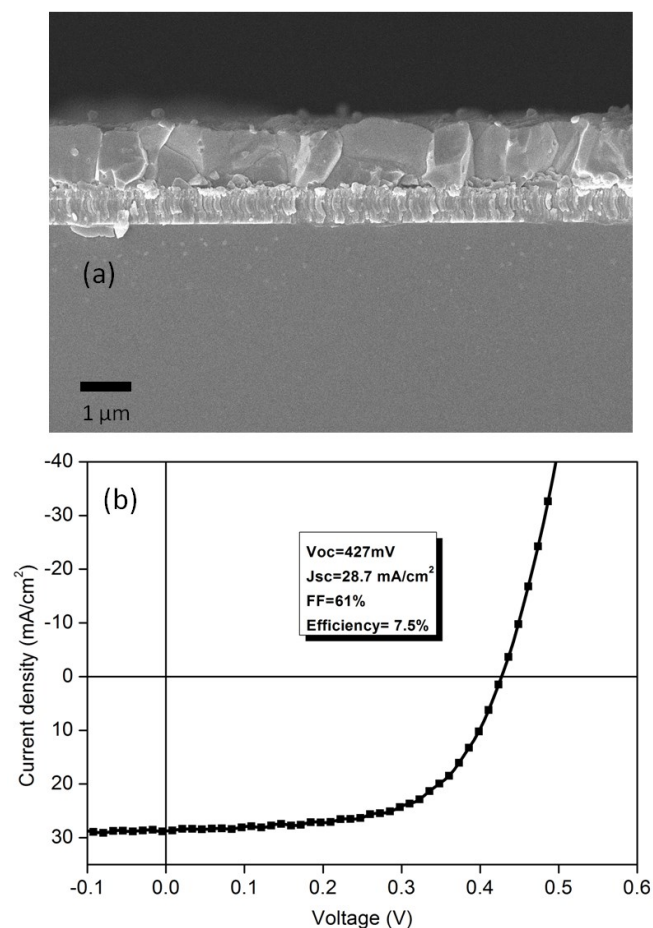


Figure 4-11 (a) cross-section image of champion device absorber (b) J-V curve of champion device with major parameters inset

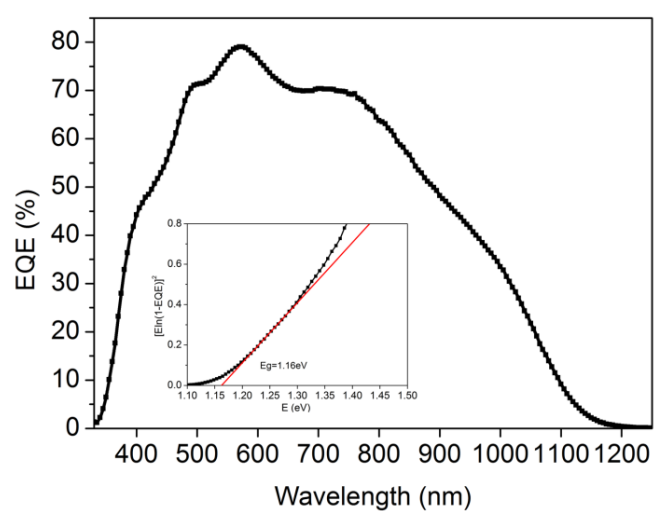


Figure 4-12 EQE curve of champion device with 7.5% efficiency (band gap calculation inset)

Apart from CdS, alternative buffer layers such as Zn(O,S) and Zn-Sn-O have also been applied to CZTSSe solar cell, with the aim of avoiding the toxicity of Cd. The Zn(O,S) buffer layer was deposited by chemical bath deposition (CBD) method and the Zn-Sn-O buffer layer was deposited by atomic layer deposition (ALD), with the Zn/Sn ratio at 4:1 for 80 nm thickness. This ratio selected was based literature report of ClGSe solar cells,⁷⁴⁻⁷⁵ which was considered suitable for primary trial on CZTSSe solar cells.

The solar cell light J-V performances are plotted in figure 4-13 for both Zn based buffer layers and CdS buffer layer as reference. The Zn(O,S) buffer layer provided a very low conversion efficiency of 0.05%. Similar phenomenon was also been observed by Barkhouse and co-worker, and was attributed to the high conduction band offset (CBO) of CZTSSe/Zn(S,O) band alignment.¹⁶ No depletion region was formed at the interface of CZTSSe/Zn(S,O), indicating a lack of band bending. Thus, the excited carriers are not able to drift into the n-type layer, so that the J_{sc} is extremely small and the diode behavior is not robust.

Compared to the CdS buffer layer, the Zn-Sn-O buffer layer displays a promising result in light conditions. The V_{oc} and FF values are slightly lower than that of CdS buffer layer, indicating the recombination conditions are similar for both solar cell devices. The main drawback for Zn-Sn-O buffer layer is the reduction in J_{sc} , which is 20% lower in comparison to that of CdS buffer layer cell. This is considered as a consequence of the high series resistance from the Zn-Sn-O layer. The R_s calculated for Zn-Sn-O buffer layer device was 80 ohm, while only 50 ohm was obtained from

the CdS reference cell. Further optimization can be applied on thinner the Zn-Sn-O buffer layer with varying the Zn/Sn ratio.

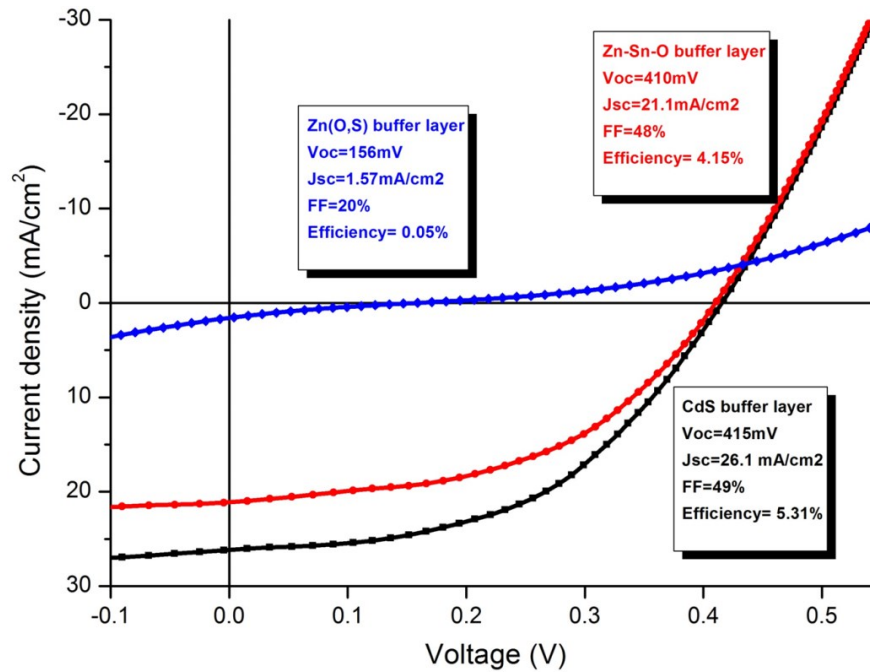


Figure 4-13 Light J-V plots of Zn(O,S) and Zn-Sn-O buffer layer solar cells with CdS as reference

4.3 Summary

The control sample was imaged by FE-SEM and presented a uniform and compact film for potential solar cell fabrication. A highly crystalline CZTSSe film was obtained after high temperature selenization. The $\text{Cu}/(\text{Zn}+\text{Sn}) \approx 0.75$ and $\text{Zn}/\text{Sn} \approx 1.15$ was detected from EDS on the CZTSSe film, which is a sufficient ratio for a functional absorber. XRD and Raman spectroscopy was used to confirm the presence of single phase CZTSSe from the surface to the bulk after the selenization step. SIMS depth profiling indicated a uniform distribution of Cu, Sn and Se elements and a slightly increasing distribution for Zn and S towards the Mo back

contact. This feature implies the possibility of ZnS(Se) coexisting at the CZTSSe/Mo interface. In addition, no traceable carbon was observed in the CZTSSe film using the deposition technique described.

These features allowed a functional absorber for the solar cell to be fabricated. Based on the control CZTSSe film, a PCE=5.1% solar cell was obtained. In addition, by varying the Se amount in the selenization process, a low-Se-content absorber could also achieved 5% efficiency. Furthermore, the PCE was improved by optimizing the fabrication conditions where a 7.5% efficiency was achieved. To our best knowledge, this is the highest efficiency of kesterite solar cell fabricated by aqueous solution technique. For all solar cell presented in the thesis, the efficiencies rang was from 5.1% to 7.5 %.

Chapter 5 Investigation of Carrier

Recombination Mechanism in CZTSSe

Absorber

This chapter focuses on the investigation of the carrier recombination mechanism for a device quality CZTSSe absorber. Through the temperature and power dependent PL spectroscopy, the carrier transition behavior is analyzed and it is concluded as donor-accepter pairs (DAPs) transition. The non-radiative recombination of carriers is analyzed from the temperature quenching effect on the PL spectra. A comparative study on the selenization temperature effect is also presented and analyzed from the perspectives of thermal activation energy of non-radiative recombination and defects contribution. The analysis reveals a suppressed effect on the non-radiative recombination from high temperature selenization process. Highly compensated defects complexes are illustrated as the origin of the DAPs carrier transition from the refined power dependent PL spectroscopy.

Photoluminescence (PL) spectroscopy is considered a powerful tool to investigate the carrier properties of a semiconductor. The minority carriers generated from the laser illumination are relaxed from the excited energy level to lower energy level through different types of recombination processes. The radiative recombination emits light with a certain wavelength corresponding to the transition condition of the carrier and the emission is collected by photon detector. With control of the temperature and laser power, the PL spectra can indicate the

carrier recombination type. The radiative and non-radiative recombination can also be analyzed from the temperature quenching effect of the PL intensity.

5.1 Analyzing Carrier Transition and Temperature Quenching Effect by PL Spectroscopy

The PL spectroscopy was conducted on CZTSSe-5 absorber, which was the control sample described in chapter 4. The film composition was Se-rich with a band gap of 1.07 eV, determined from the EQE spectrum. Temperature dependent PL spectroscopy was conducted by controlling the temperature within the range 6.5 K to 120 K (figure 5-1) and by using a Helium cryostat as the cooling liquid.

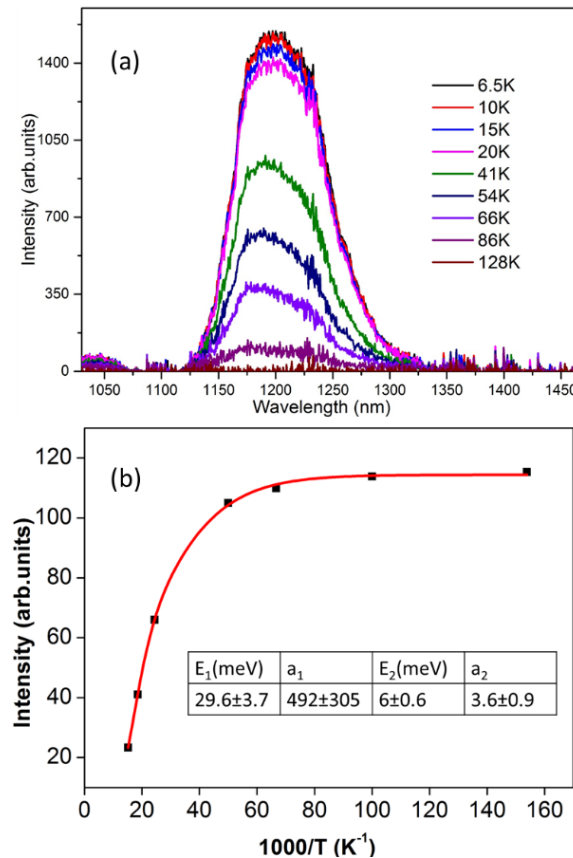


Figure 5-1 (a) spectra of temperature dependent photoluminescence on CZTSSe-5 film (b) temperature quenching effect fitting with two non-radiative recombination parameters

The photoluminescence are originated from the radiative recombination of carriers. Herein, the luminescence peaks were analyzed to reveal the radiative recombination type and temperature quenching effect. Three types of radiative recombination, (i) band-to-band transition, (ii) free-to-bound transition and (iii) donor-acceptor pairs (DAPs) transition, were taken into consideration. The energy diagram was drawn as in figure 5-2 below. The band-to-band transition referred the recombination of the carriers from conduction band directly to valence band. The free-to-bound transition referred to the transition involved both defect and band in the recombination. The donor-acceptor pairs (DAPs) transition occurred when only defects involved in the radiative recombination.

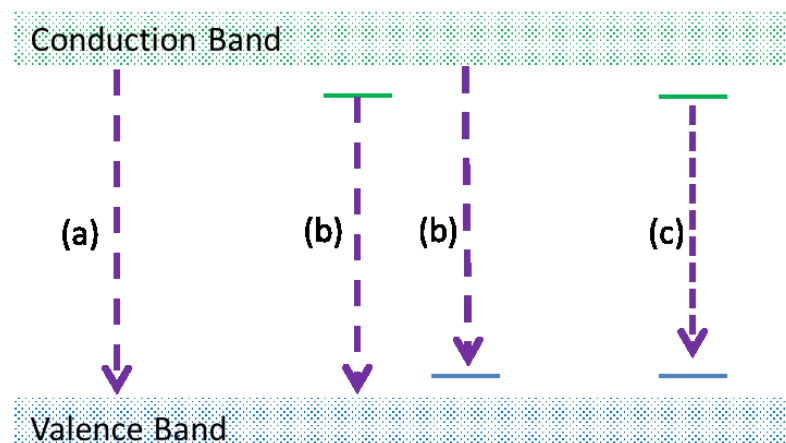


Figure 5-2 radiative recombination transition types, (a) band-to-band transition (b) free-to-band transition (c) donor-acceptor pairs (DAPs) transition

The spectra showed no substantial peaks shifting and peaks shape changing with respect to the temperature changing. This phenomenon revealed that the type of radiative recombination was consistent within the temperature range studied. Single type of radiative recombination mechanism was presented in this

measurement. The luminescence peak energy centered at 0.97 eV was lower than the band gap value derived from the EQE calculation, which eliminated the possibility of band-to-band transition type at the recombination.

Further analysis also rules out the free-to-bound transition type. For this type of transition, either VB or CB is involved in the recombination so that the luminescence peak energy should be correlated to the temperature based on the equation such that ³⁸

$$h\nu = E_g - E_{D/A} + n_u k_B T \quad (5.1)$$

where E_g is the band gap, E_D and E_A are the donor and acceptor ionization energies and n_u is constant. The principle of this equation could be interpreted as the optical energy emission obtaining from the excited carrier recombination. The assumption to this equation was that the excited carrier recombination through a donor or acceptor level rather than direct recombination from conduction band to valence band. The carrier was bound to the defects level before an optical wave emitted from the material. The $n_u k_B T$ in the equation referred to the thermal energy added up from the conduction/valence bands. For example, in higher temperature the emission could come from a slightly higher state in conduction band recombining to an acceptor defect. For the free-to-bound transition, temperature increment should lead to the blue-shift of the luminescence peak positions. As no peak blue-shift was observed in the spectra, it indicates neither the CB nor the VB are involved in the recombination process. Therefore, DAPs transition is confirmed to be responsible for the luminescence from the sample. The DAPs transition can be attributed to the intrinsic properties of CZTSSe since

the CZTSSe is considered as a heavily doped and highly compensated p-type semiconductor.

Furthermore, a large temperature quenching effect was also observed, whereby the luminescence intensity dropped significantly with a corresponding increase in temperature. This phenomenon can be explained by the thermal activation of non-radiative recombination where no light is emitted during the non-radiative recombination. For a detailed analysis at $T < 41$ K, the luminescence intensity does not reduce significantly with increasing temperature, while at $T \geq 41$ K it shows an extensive drop till $T=120$ K. This quenching process reveals two non-radiative recombination channels being activated during the increase of temperature, leading to the carrier recombining in a non-radiative way. Thus, two thermal activation energies E_1 and E_2 , can be extracted by fitting the spectra curves with following equation ⁷⁶:

$$I(T) = I_0 \left(1 + a_1 e^{-\frac{E_1}{k_b T}} + a_2 e^{-\frac{E_2}{k_b T}} \right)^{-1} \quad (5.2)$$

where I_0 is the PL intensity extrapolated at $T=0$ K. The a_1 and a_2 are the coefficients that indicate the degeneracy level of the non-radiative recombination pathways. The fitting shown in figure 5-1(b) reveals $E_1 = 29.6 \pm 3.7$ meV and $E_2 = 6 \pm 0.6$ meV with a_1 in two order magnitudes larger than a_2 . These values indicate that at very low temperature of $T < 41$ K, only one non-radiative recombination channel is activated corresponding to a small activation energy of E_2 . Since the degeneracy factor a_2 is very small, the temperature quenching effect is not significant. However, when the temperature rises beyond 41 K, channel E_1 starts

contributing significantly, resulting in a remarkable drop of luminescence intensity. The mechanism behind the remarkable non-radiative recombination can be understood as the thermal activation of intrinsic deep defects inside CZTSSe which could originate from non-stoichiometric composition or an insufficient high temperature selenization process.^{51 77}

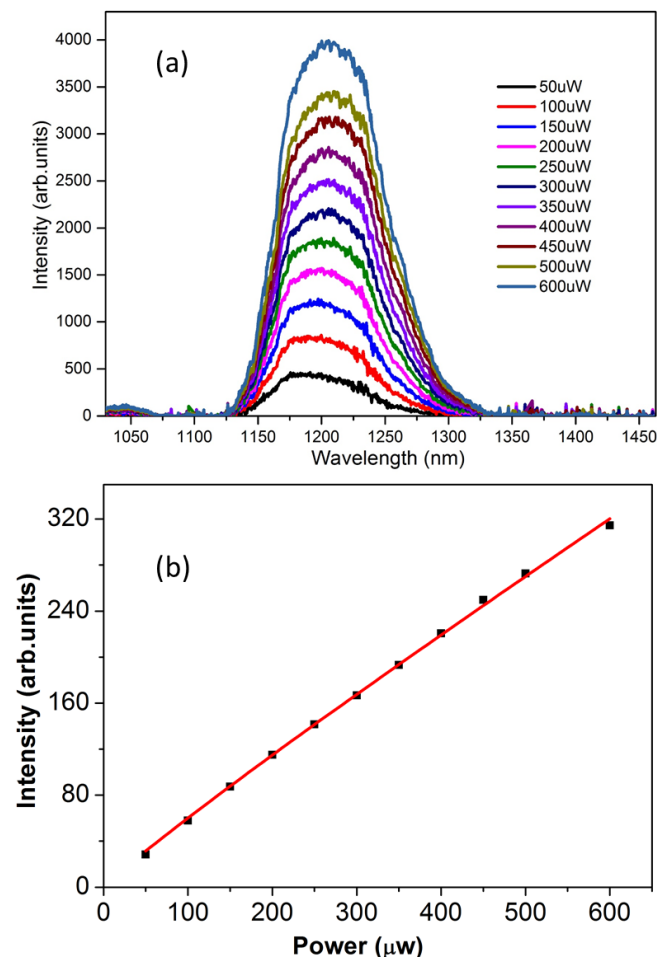


Figure 5-3 (a) spectra of power dependent photoluminescence on CZTSSe-5 film (b) power law fitting of the luminescence intensity versus laser power with a coefficient of 0.93 ± 0.013

Figure 5-2(a) shows the power dependent PL spectra measured at $T=6.5$ K from laser power of 50 μW to 600 μW. As expected, a clear luminescence intensity

increment is observed with increasing laser power. The relationship can be fitted with the following power law ³⁷:

$$I \propto P^k \quad (5.3)$$

where P is the laser power and I is the luminescence intensity and k is the coefficient. The calculated $k \geq 1$ indicates the radiative recombination is excitonic, meaning the band-to-band transition is obtained; while $k < 1$ indicates the recombination involves defects. The principle behind the equation is derived from derivation of near-band-edge photoluminescence. More excited carriers would be generated from the valence band to conduction band as the injected power increased. As the P was large than the band gap and is varying no more than two order of magnitude, the k value indicates the recombination mechanism by comparing its value to 1, meaning to evaluate the proportional increment of emission to the excitation of the carriers.

The fitting shown in figure 5-2(b) attains a k value of 0.93 ± 0.013 , suggesting the donor or acceptor defects are involved in the recombination process. Further observation finds that the small blue-shift of peaks is observed when the power enhances. This phenomenon represents the feature of the DAPs transition type of carriers based on the equation that:

$$h\nu = E_g - (E_D + E_A) + \frac{e^2}{4\pi\epsilon_0\epsilon r} \quad (5.4)$$

where E_g is the band gap, E_D and E_A are the donor and acceptor ionization energies, r is the distance between the donor and acceptor, ϵ_0 is the permittivity of vacuum

and ε is the relative permittivity. The last term expresses the Coulombic interaction between the donors and acceptors. As the laser power increases, the donor-acceptor pairs with smaller r value are also excited and contribute to the recombination spectra, which lead to a blue-shift of the peaks. This observation further verifies the aforementioned DAPs transition suggested by the temperature dependent PL spectra.

Based on the observation analysis above, the defects inside the film play a detrimental role to the minority carriers. The lifetime of the minority carrier and carrier transportation in the film are limited by the large quenching effect from the defects. Besides, the non-radiative recombination is significant inside film which suppresses the V_{oc} . Secondary electron activation from the luminescence cannot be expected due to the lower energy of the luminescence compared to the band gap of the absorber. Therefore, to further improve the CZTSSe absorber quality, the defects quenching effect should be minimized.

5.2 Selenization Temperature Effect on Non-radiative Recombination Channels

Compared to the control sample described above, the CZTSSe-7 absorber was selenized at a higher temperature of 540°C, resulting in the highest 7.5% efficiency solar cell. A band gap of 1.16 eV was calculated from EQE curves and the same procedures for the PL spectroscopy measurements were used for the temperature dependent and power dependent measurements. The cryostat was cooled by

liquid N₂, with a minimum temperature of 77K, which was then ramped up to 180K for the measurement.

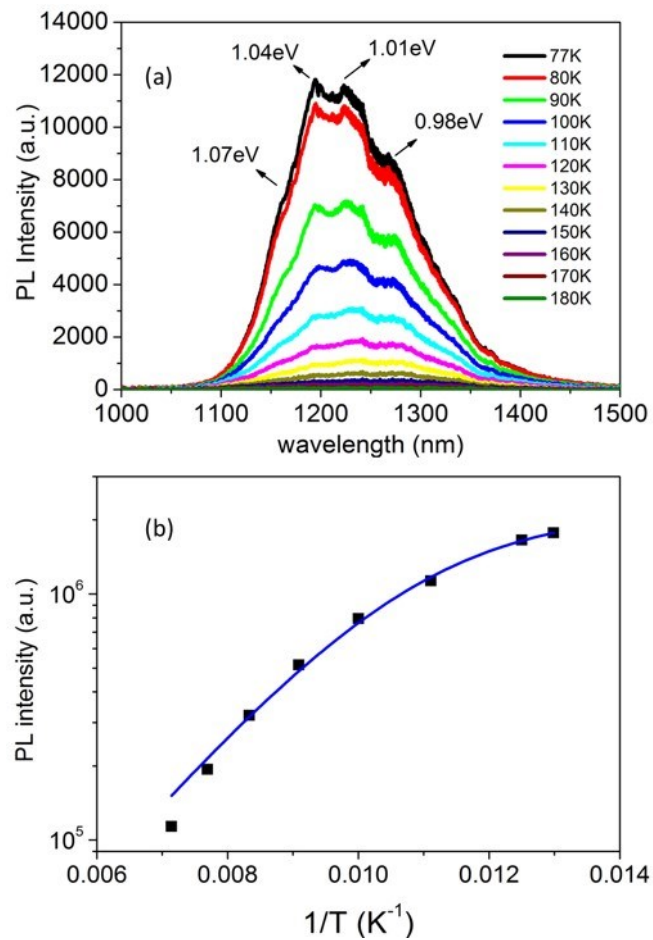


Figure 5-4 (a) spectra of temperature dependent photoluminescence on CZTSSe-7 film (b) temperature quenching effect fitting with one non-radiative recombination parameter

As shown in figure 5-3, the PL spectrum shows a clear temperature quenching effect as expected. The peak energy is lower than the band gap and no change in position is observed along with increasing temperature. Therefore, based on the conclusions discussed in previous experiment, the recombination can be identified as a DAPs transition type. It is worth noting that multiple peaks are observed in the spectra and peak shapes change with increasing temperature. This phenomenon

will be discussed in the following section with comparison to the PL spectra of CZTSSe-5 control absorber.

To calculate the thermal activation energy of the non-radiative recombination, the integrated peak intensity of all peaks measured from 77 K to 140 K was used to fit with equation as following:

$$I(T) = I_0 \left(1 + ae^{-\frac{E}{k_b T}} \right)^{-1} \quad (5.5)$$

Since no clear separation of temperature quenching effect from the spectra is observed in the measurement temperature range, only one major channel of non-radiative recombination is presented with a thermal activation energy of $E = 59.5 \pm 4.1$ meV.

The power dependent PL spectroscopy was also conducted with a laser power ranging from 1 mW to 10 mW at 77 K (figure 5-4). The power law fitting using equation (5.3) indicated a k value of 0.74 ± 0.02 , which is much less than 1, and indicates a restricted bound effect of the carriers in the defects. The phenomenon of the change in the peak shape with increasing temperature is discussed further in the following section.

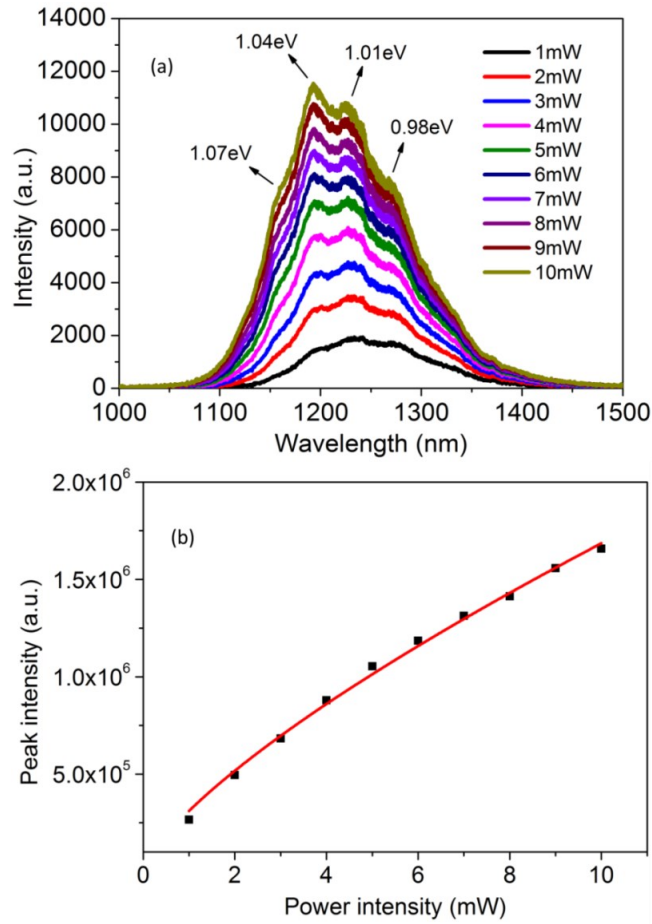


Figure 5-5 (a) spectra of power dependent photoluminescence on CZTSSe-7 film (b) power law fitting of the luminescence intensity versus laser power with a coefficient of 0.74 ± 0.02

5.3 Comparison Analysis on Recombination Behavior in CZTSSe

5.3.1 Phonon Assisted DAPs Transition Analysis from PL Spectra

As described in section 5.2, the temperature dependent PL and power dependent PL spectra of both CZTSSe-5 and CZTSSe-7 absorber were analyzed to describe the recombination conditions and non-radiative quenching effect within the film. It is worth noticing that the PL spectra for CZTSSe-7 presented four

separated peaks merging together. The separation of the peaks becomes more enhanced as the temperature was reduced. However, this phenomenon is not observed in the PL spectra of CZTSSe-5 even though the measuring temperature was reduced to 6.5K. Thus, the analysis of the origin of these peaks can provide further information regarding to the electronic properties of the film.

The four peaks are centered at 1.07 eV, 1.04 eV, 1.01 eV and 0.98 eV respectively. Surprisingly, from a detailed observation, the separation energy of each two neighboring peaks equals to $\Delta E = 0.029$ eV. The peaks separation is enhancing as temperature is reduced and this phenomenon can be explained by attributing to the longitudinal optical (LO) mode phonon coupling effect. Similar peaks pattern has been reported for other semiconductors such as ZnO and SnO₂, which clearly indicate the multiple LO-phonon coupling of the luminescence from the spectra.^{78 79} CZTSe PL spectra with longitudinal optical (LO) phonon coupling had also been reported to accompany a DAPs type recombination.⁸⁰

In order to confirm the validity of the explanation, phonon energy calculation based on LO mode vibration was carried out. From the Raman spectra shown in figure 5-5, two A₁ mode vibrations at 204 cm⁻¹ and 327 cm⁻¹ are identified and correspond to the CZTSe and CZTS with two-model behavior shifts. Based on the theoretical calculation for kesterite material, the peak at 237 cm⁻¹ is identified as the B(LO) mode as discussed in the literatures.^{81 82 83} The energy shift correlated to this peak is 0.028 eV which is very close to the $\Delta E = 0.029$ eV observed from the PL spectra. Therefore, the consistency of the Raman spectra and PL spectra, add further confirmation of the suggested the luminescence mechanism.

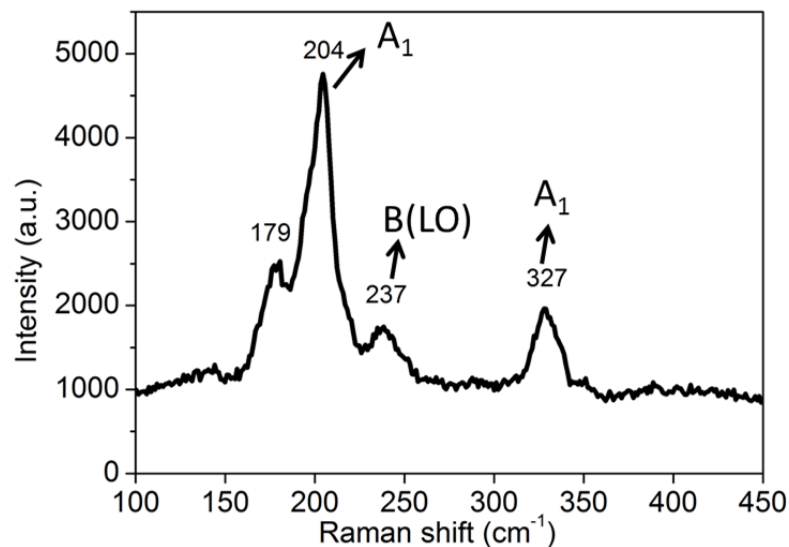


Figure 5-6 Raman spectra of CZTSSe-7 with indicating the vibration mode

In addition, as the temperature was reduced, the peaks with higher energy in the temperature dependent PL spectra rise up more rapidly than the lower energy peaks. The same peak changing pattern is also observed from power dependent PL spectra with the excitation power increased. The sharing effect for lowering temperature and increasing power is due to the boosting of the radiative recombination, which results in a higher luminescence intensity. As a consequence, the LO-phonon coupling becomes insufficient to maintain a correlation with the large change in temperature or laser power.

Based on this explanation, a further reduction in power intensity should eventually result in sufficient LO-phonon coupling for the excited carriers, which subsequently produce a major peak centered at 0.98 eV. Therefore, another series of power dependent PL was carried out with laser power refined in the range 100 μ W to 1000 μ W.

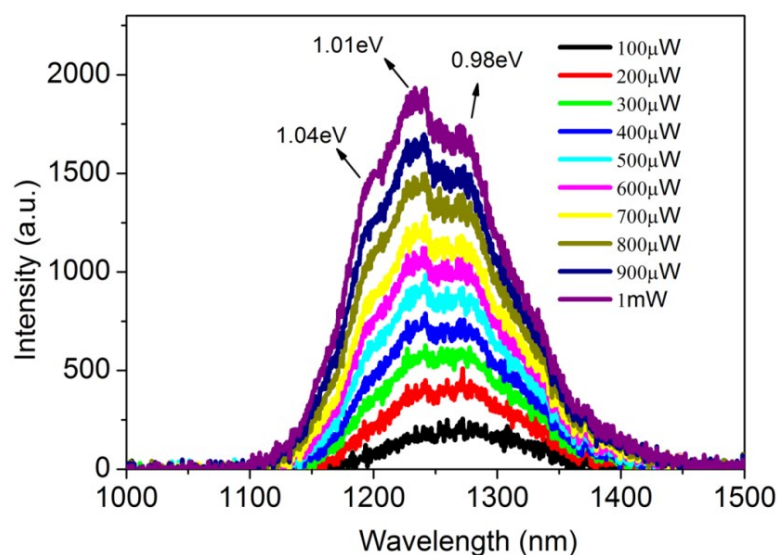


Figure 5-7 Power dependent PL on CZTSSe-7 with power range from 100 μ W to 1 mW

As shown in figure 5-6, the high energy luminescence peak gradually disappears when the laser power is reduced. The peaks merge towards lower energy and eventually combine to give a broad peak centered at 0.98 eV at 100 μ W laser intensity. This observation adds further verification to the suggested phonon assisted DAPs transition mechanism.

5.3.2 Luminescence Energy Discussion and its Relation to the V_{oc} of the Solar Cell

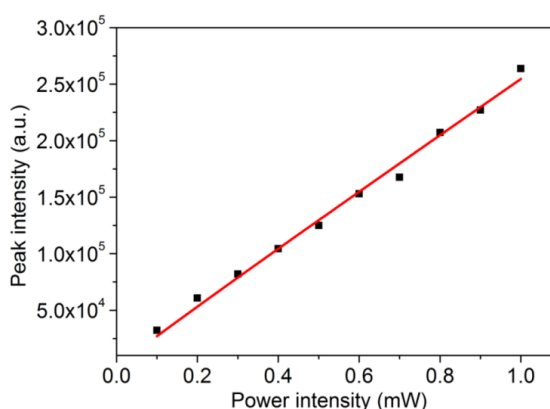


Figure 5-8 Power law fitting in the range of 0.1-1 mW with coefficient value $k=0.97\pm0.04$

The power law fitting were also applied to the laser power range from 100 μW to 1 mW, shown in figure 5-7. The coefficient k value was calculated to be 0.97 ± 0.04 . Comparing to the k value of 0.74 for high laser intensity from 1 mW to 10 mW, it shows that the transition occurring under lower laser intensity behaves as nearly excitonic, which means that the recombination is like a “band to band” transition type. As it has been verified that the recombination is DAPs type in the film, this calculation reveals the defects density of states in the material. Under a low laser power excitation, the generated carrier is in small amount. The defects states are highly-compensated and heavily doped defects, where most of the excited carriers are held under low incident light irradiance. Therefore, they are considered sufficient to contain the excess carriers, which behave like a “mid-gap states” within the forbidden energy band of the semiconductor (figure 5-8). The recombination behaves in an excitonic manner. However, as the laser power increases, the excess carriers overwhelm the defects states, so that the recombination behaves as DAPs transition.

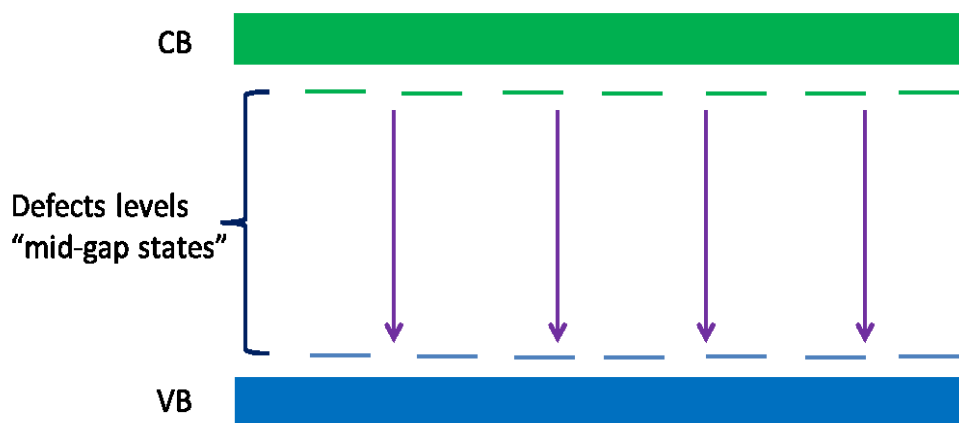


Figure 5-9 Illustration of “mid-gap states” inside the forbidden band of semiconductor

Comparing the spectra of CZTSSe-7 to CZTSSe-5, the multi-peaks pattern originating from the LO-phonon coupling indicated a better crystallization of the film.⁷⁸ It can be attributed to the higher selenization temperature (540°C for CZTSSe-7 and 520°C for CZTSSe-5). As the ramping rate for the selenization process is consistent, the time for the film experiencing high temperature through the whole process is longer for CZTSSe-7 than that of CZTSSe-5. Thus, both factors are considered to contribute to the high crystallinity of the film.

To find the relationship between the open circuit voltages, photoluminescence peak energy and band gaps of the CZTSSe-5 and CZTSSe-7, figure 5-10 indicated the respective values from the aforementioned data, as shown below. The band gap difference between CZTSSe-5 and CZTSSe-7 was very close to the PL peak energy. As donor-acceptor pairs transition was revealed to be the radiative recombination type for the carriers, this similarity indicated a consistent transition mechanism was involved in both cells. Consequentially, the V_{oc} of the CZTSSe-7 is higher than CZTSSe-5. Even the V_{oc} deficit is higher for CZTSSe-7 (0.643V) than that of CZTSSe-5 (0.6), the overall performance of CZTSSe-7 is better.

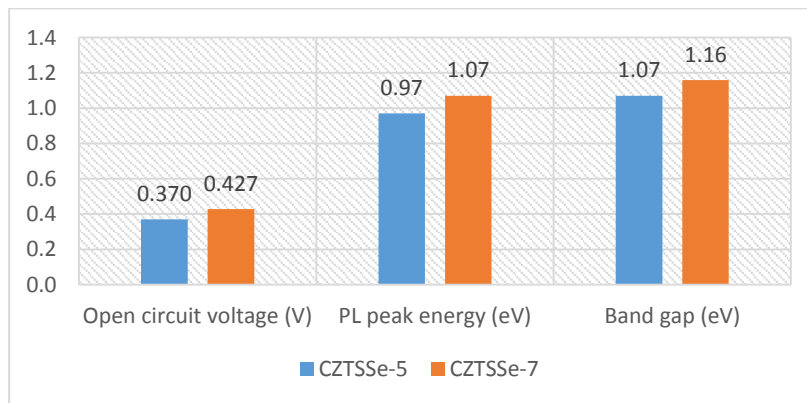


Figure 5-10 value of V_{oc} , PL peak energy and band gap of both CZTSSe-5 and CZTSSe-7 device

5.3.3 Comparison Study on Thermal Activation Energy of Non-radiative Recombination

The temperature quenching effect for CZTSSe-7 is less noticeable than that of CZTSSe-5 (Figure 5-3). It indicates a less non-radiative recombination occurring when the photon is injected. The thermal activation energies of non-radiative recombination were calculated for both CZTSSe-7 and CZTSSe-5 absorber. The value for CZTSSe-7 (59.5 meV) is much higher than that of CZTSSe-5 (29.6 meV), revealing a less favorable thermal activation of the non-radiative recombination for CZTSSe-7.

5.4 Minority Carrier Lifetime Study by TRPL on CZTSSe-7 Absorber

The minority carrier lifetime has an essential relationship with the solar cell performance. The minority carrier lifetime describes the carrier recombination conditions in semiconductor materials. The longer the minority carrier lifetime, the lower of reversed saturated current can be achieved based on the diode equation (5.6), such that

$$I_0 = eA \left(\sqrt{\frac{D_P}{I_P}} \frac{n_i^2}{N_D} + \sqrt{\frac{D_N}{I_N}} \frac{n_i^2}{N_A} \right) \quad (5.6)$$

where I_0 is the reversed saturated current of diode, A is the cross sectional area, D_P and D_N are the diffusion coefficients of holes and electrons respectively, I_P and I_D represent the carrier lifetime of holes and electrons in n-type and p-type semiconductors. The longer the minority carriers can coexist with majority carriers,

the less pronounced recombination is expected. The reversed saturated current I_0 reflects the diode “leakage” capability, which has an inverse relationship with the V_{oc} of the solar cell devices as shown in the equation (5.7), where J_L is the light generating current. Thus, the minority carrier lifetime is crucial for obtaining a high V_{oc} in a solar cell.

$$V_{oc} = \frac{nkT}{q} \ln \left(1 + \frac{J_L}{J_0} \right) \quad (5.7)$$

In the experiment of time resolved photoluminescence (TRPL) spectroscopy, the PL decay time reflects the competition between radiative recombination and non-radiative recombination as shown in equation (5.8)

$$\frac{1}{\tau_{PL}} = \frac{1}{\tau_{rad}} + \frac{1}{\tau_{non}} \quad (5.8)$$

where τ_{PL} represents the PL decay time, τ_{rad} and τ_{non} represent the radiative and non-radiative lifetime of minority carriers.⁷⁷ The PL decay time τ_{PL} is predominated by the smaller value between τ_{rad} and τ_{non} . Therefore, both time values are expected to be high in order to achieve a long minority carrier lifetime.

In this work, TRPL spectroscopy was conducted on CZTSSe-7 absorber with different excitation laser powers. The spectra are shown in figure 5-9, and fitted with the following single exponential function

$$I_{PL}(t) = Ce^{-t/\tau} \quad (5.9)$$

where C is the coefficient and τ is the decay time describing the minority carrier lifetime. The PL decay time was calculated to be less than 2 ns, which indicated a very short lifetime of the minority carriers.

As stated in the previous sections in this chapter, severe non-radiative quenching effect was observed from the temperature dependent PL spectra, meaning that the non-radiative recombination was becoming more influential as the temperature increased. In other words, this phenomenon can be explained by the reduction of the luminescence efficiency as the temperature increased.⁷⁷ The luminescence efficiency p is determined by the radiative and non-radiative lifetime of carrier recombination, such that

$$p = \frac{\tau_{PL}}{\tau_{rad}} = \frac{1}{1 + \tau_{rad}/\tau_{non}} \quad (5.10)$$

As the carrier lifetime of non-radiative recombination becomes shorter at higher temperature, based on equation (5.10), the luminescence efficiency drops significantly. This is consistent with the observation from temperature dependent PL spectra. Therefore, it is believed that the non-radiative recombination was the main factor that led to the short minority carrier lifetime.

From the spectra shown in figure 5-10, it can be seen clearly that as the laser power increases, the PL decay time gets smaller (as indicated by the arrow in figure 5-10). The fitting parameters shown in table 1 confirm this observation.

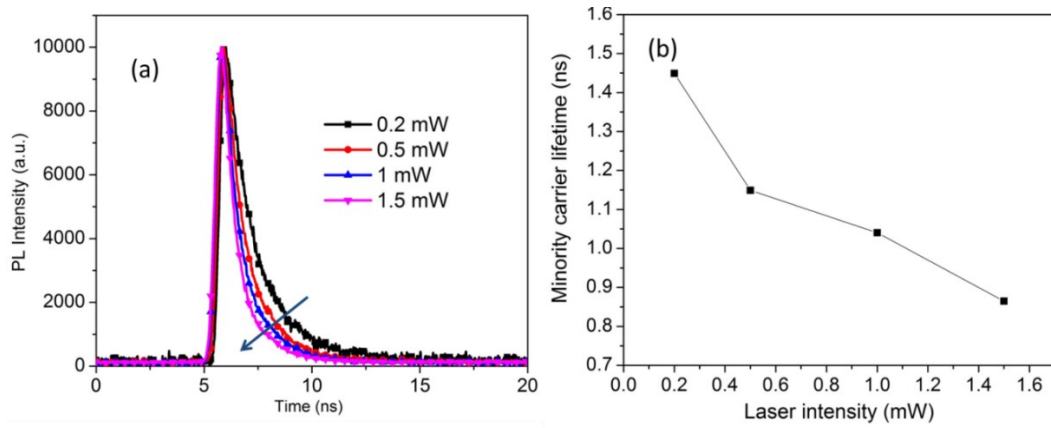


Figure 5-11 a) spectra of TRPL on CZTSSe-7 absorber with different power intensity (b) fitting results of minority carrier lifetime τ

Table 1 TRPL fitting results with different laser power

Laser power	0.2 mW	0.5 mW	1 mW	1.5 mW
Decay time τ (ns)	1.45	1.15	1.04	0.86
coefficient	6640	8058	9112	9148

The reason for the minority carrier lifetime changing with respect to the power intensity is the excess carrier concentration. The TRPL is based on the recombination of excitation carriers over certain period of time. The radiative recombination rate has confirmed relationship with the excess carrier density and the equilibrium carrier concentration.⁸⁴ In a p-type semiconductor, the relation is simplified as in following equation

$$R_{rad}(t) = B \int [p_0(r, t)\Delta n(r, t) + \Delta p(r, t)\Delta n(r, t)] d^3r \quad (5.11)$$

where R_{rad} is the radiative recombination rate, B is the radiative coefficient, p_0 is the equilibrium hole concentration, Δn and Δp are the excess electrons and holes density.⁸⁴ The excess electrons and holes originate from the light injection

from the laser. Therefore, under low-injection conditions, Δp and Δn are small in comparison to p_0 . The first term dominates the radiative recombination rate, resulting in a long PL decay time. On the other hand, under high-injection conditions, Δp and Δn are very large, so that the second term $\Delta p(r, t)\Delta n(r, t)$ contributes significantly to the R_{rad} , and a fast decay is observed.

These results are consistent with the observation on CIGSe absorbers.^{85 84} A future study could focus on the quantitative analysis of the minority carrier lifetime for kesterite absorber under different radiative condition, and its relation to the V_{oc} of the solar cell. Lasers with different wavelength are also believed to have effect on the minority carrier lifetime as the momentum of the excited carriers change accordingly. Therefore, laser sources with different wavelengths are recommended for a more detailed study on the minority carrier lifetimes.

5.5 Summary

By analyzing the PL spectra from temperature dependent and power dependent measurements, the DAPs transition is confirmed as the main recombination mechanism in the CZTSSe film. The DAPs transition gives a lower recombination energy than the absorber band gap that can eventually compromise the V_{oc} obtained from the solar cell.

The temperature quenching effect reflects a significant non-radiative quenching of the minority carriers in the CZTSSe absorber. In this case, the minority carrier lifetime is believed to be shortened, so that the V_{oc} of the solar cell reduces. The thermal activation energies have been calculated for both absorbers and

indicate that by applying higher selenization temperature, the quenching effect can be reduced. In addition, the power dependent PL spectra indicate a “mid-gap states” existing inside the forbidden energy band, which are due to the defects complexes in the CZTSSe as a heavily doped and highly compensated semiconductor. This “mid-gap states” is considered to contribute to the V_{oc} deficit of the solar cell.

The minority carrier separation and collection are critical for the performance of the solar cell. The PL spectroscopy illustrates a feasible way to analyze the quality of the absorber in terms of the minority carrier behavior.

Chapter 6 Energetics Study and Discussion on the V_{oc} of CZTSSe Solar Cells

In this chapter, the energetics alignment of the CZTSSe solar cell has been studied using impedance spectroscopy. The recombination resistances of the devices are investigated from the Nyquist plot under DC bias conditions. The carrier concentration and flat band potential are extracted from the Mott-Schottky relation and indicate the energetics alignment changes for solar cells fabricated using different conditions. The effects of energetics alignment regarding to the V_{oc} achieved are discussed and illustrated schematically. It is aimed that this work can open a discussion of the solar cell V_{oc} from the perspective of the device energetics.

The impedance spectroscopy is a technique that measures the device impedance property under various AC and DC voltages. It mainly focuses on analyzing the junction properties, such as the electrode-electrolyte interface charge transfer and solid interface p-n junction. Thus, it has been widely applied to analyze different types of solar cell including dye-sensitized solar cell (DSSCs),^{58-59,}
⁸⁶ organic solar cell, ^{61, 87-88} thin film solar cell ^{57, 89-90} and Si solar cell ^{60, 91}.

6.1 V_{oc} Analysis and Comparison from J-V and EQE Measurement of the Solar Cells

The chalcogenide based kesterite semiconductor shares many superior properties with chalcopyrite CIGSSe material such as intrinsic p-type characteristics, direct band gap and high absorption coefficient. However, the kesterite solar cell

has only achieved a power conversion efficiency of 12.8% thus far. The V_{oc} of kesterite solar cell is generally lower than that of chalcopyrite solar cell even though they share the same band gap values, which leads to a strong limitation to its photovoltaic performance. The problem has been attributed to the intrinsic electrical properties of the CZTSSe, in particular: bulk recombination in the CZTSSe absorber, interface recombination between CZTSSe/CdS and inner energetics order of the devices.^{34, 92} The recombination mechanism of kesterite solar cell is currently under investigation and the low V_{oc} value cannot be easily derived, and interpreted from the electrical properties of the devices.⁹³ Thus, the investigation of the p-n junction properties is critical for a better understanding the origin of the low V_{oc} values for kesterite solar cell.

Three CZTSSe absorbers were fabricated by chemical spray pyrolysis followed by selenization, as described previously in chapter 4. The thicknesses of the three CZTSSe absorbers were 0.6 μm , 0.9 μm and 1.3 μm and the selenization temperatures were 520°C, 520°C and 540°C (chosen after a performance optimization process). The selenium amount (30 mg pellet) and selenization time (12 minutes) were identical for all three selenization processes. The Cu/(Zn+Sn) and Zn/Sn ratio of all three CZTSSe were measured in the range of 0.75-0.8 and 1.1-1.15 by EDX, which was considered in the optimum ratio range for CZTSSe absorbers. The solar cells were fabricated through the typical structure of glass/Mo/CZTSSe/CdS/i-ZnO/AZO/electrodes without an anti-reflection layer coating. The cell areas were identical at 0.11 cm^2 . The measurement was

performed as described in the experimental chapter 3. Z-View software was employed to fit the data obtained.

The different absorber fabrication conditions lead to different photovoltaic performance of the solar cell. Figure 6-1(a) shows the current-voltage (J-V) curves of three devices under light and dark (one sun at AM1.5) conditions. The fabrication and performance parameters of the three devices are listed in Table 2 as cell-5, cell-6 and cell-7, representing their efficiency levels. To the best of our knowledge, the 7.5% efficiency is also the highest reported efficiency for the CZTSSe solar cell fabricated using aqueous solution deposition technique.

Table 2 Selected kesterite solar cells parameters

<i>Solar cells</i>	<i>Selenization temperature (°C)</i>	<i>PCE (%)</i>	<i>V_{oc} (mV)</i>	<i>J_{sc} (mA/cm²)</i>	<i>FF (%)</i>
<i>Cell-5</i>	<i>520</i>	<i>5.1%</i>	<i>371</i>	<i>27.3</i>	<i>50</i>
<i>Cell-6</i>	<i>520</i>	<i>6.0%</i>	<i>387</i>	<i>28.5</i>	<i>54</i>
<i>Cell-7</i>	<i>540</i>	<i>7.5%</i>	<i>427</i>	<i>28.7</i>	<i>61</i>

The J_{sc} values increase slightly when the absorber thickness increases from 0.6 μm to 0.9 μm and are almost identical for 0.9 μm and 1.3 μm thicknesses. This indicates that the devices almost reach an optimum thickness for the absorber layer in terms of current collection. The differences in the PCE are mainly ascribed to the V_{oc} and FF. In this case, the parameters affecting the V_{oc} become the focus of our analysis.

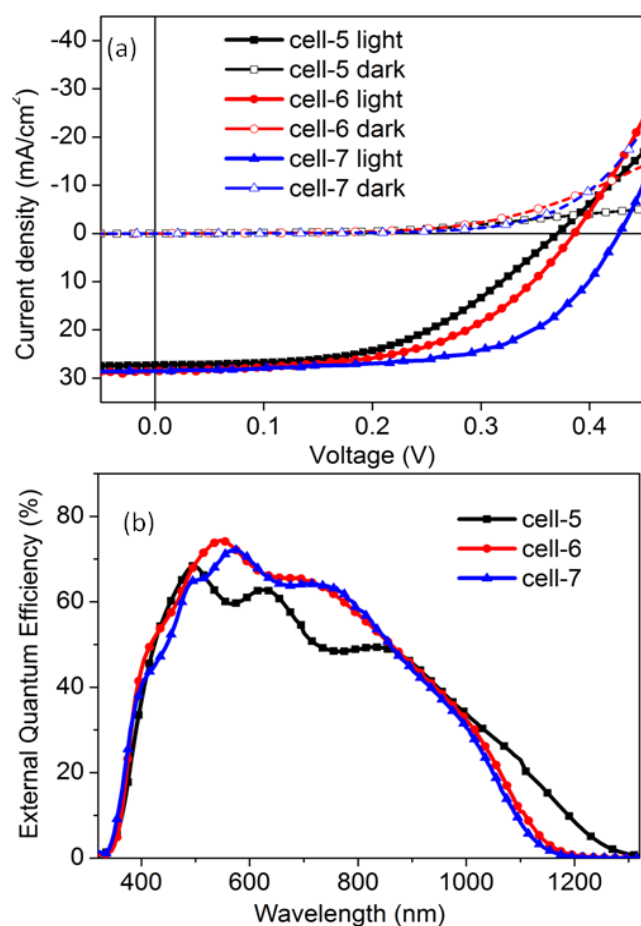


Figure 6-1 (a) J-V curves of selected solar cells under dark and light (one sun AM 1.5) conditions (b) EQE curves of selected solar cells

The band gaps of the CZTSSe absorber were calculated from the external quantum efficiency (EQE) plot (figure 6-1(b)). Despite the slightly lower band gap of cell-5 ($E_g=1.07$ eV), cell-6 and cell-7 possess almost identical band gaps ($E_g=1.16$ eV). The variation of band gaps can be attributed to the different selenium concentration level in the CZTSSe, originating from the different selenization process and thickness of the films. A widely extended analysis relates the V_{oc} to the band gap of the absorber and the reversed saturated current of the diode, which can be described in the following equation:

$$V_{oc} = \frac{E_a}{q} - \frac{nkT}{q} \ln \left(\frac{J_{00}}{J_L} \right) \quad (6.1)$$

where E_a is the activation energy of the recombination, n is the diode ideality factor, J_{00} is the reverse saturated current pre-factor and J_L is the light current.⁹⁴ If the major recombination of the solar cell is determined by the bulk of the absorber layer, the activation energy E_a shall equal the band gap of the absorber layer if the carrier recombination is simply a band-to-band transition. In the DAPs type of transition, the activation energy shall be considered as the energy between the defects levels, which is less than the band gap of the CZTSSe. Therefore, the V_{oc} is relatively low comparing to the absorber band gap.

However, although cell-6 and cell-7 present similar absorber band gaps, the n_{cell-6} and n_{cell-7} calculated from their J-V curves are 2.4 and 2.1 respectively. These values, which are larger than 2, indicates the recombination mechanism cannot be simply identified as a standard Shockley-Read-Hall (SRH) recombination process.⁹⁵⁻
⁹⁶ Thus the n values are not reflecting the exact recombination conditions of the diode. As a consequence, other recombination mechanisms, such as interface recombination, should also be considered. Indeed, the interface recombination has been previously proposed as the dominating recombination mechanism for kesterite solar cell by many groups.^{27, 92, 97} Therefore, E_a is not equal to the band gap of the CZTSSe and the V_{oc} values cannot be simply implied from the above equation.

From another perspective, under illumination, both the recombination and the device energetics determine the splitting of the quasi-Fermi levels for electrons

and holes to achieve the V_{oc} . In this case, to further analyze the V_{oc} and p-n junction property, impedance spectroscopy was applied on these three cells to investigate the recombination resistance effect and band alignment status.

6.2 Investigate Recombination Resistance from Nyquist Plot of Impedance Spectroscopy

The obtained Nyquist plots are fitted with simple equivalent circuit, as shown in figure 6-2(a), where R_s stands for series resistance and R_{rec} stands for recombination resistance. The circuit fitting focuses on understanding the overall impact of the dominated p-n junction in the solar cell. The capacitance was fitted by means of a constant phase element (CPE). The R_{rec} obtained from the fitting of the devices in their working range (i.e. from 0 to 0.5 V) is shown in figure 6-2(b). The higher value of R_{rec} indicates higher recombination resistance, which means lower recombination rate. R_{rec} significantly decreases in the measured range, which is consistent with typical diode behavior.⁶⁰ In principle, a high recombination resistance in the solar cell shall lead to higher V_{oc} , given the same band gap. However, the recombination analysis does not justify the obtained differences in the V_{oc} . The device with lower R_{rec} , cell-7, is the one achieving the highest V_{oc} , whereas cell-6 and cell-5 present similar R_{rec} . The devices probably present different recombination conditions in dark and under illumination, as it can be inferred from the different shapes of the J-V curves in dark and under 1 sun (see Fig 6-1). As a consequence, a more in-depth study of the carrier recombination under illumination is suggested to review change of the recombination resistance with illumination.

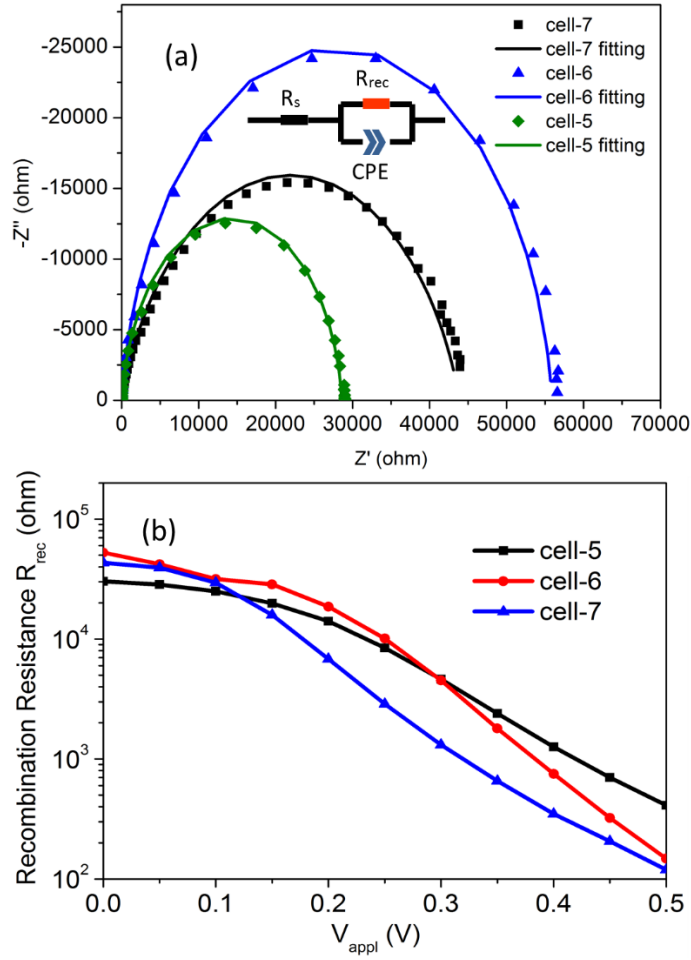


Figure 6-2 (a) impedance spectra fitting by Z-view software with the fitting circuit inset (b)

R_{rec} fitting results from 0-0.5 V for all three cells.

6.3 Energetics Alignment Illustration and Discussion from Mott-Schottky Relation

In order to elucidate further the origin of the V_{oc} difference, Mott-Schottky relations, calculated from the capacitance measured by impedance spectroscopy, were plotted as shown in figure 6-3. The high charge carrier concentration of the n-type materials (10^{17} cm^{-3} for CdS and $10^{18-20} \text{ cm}^{-3}$ for ZnO) allows the approximation of our system to a semiconductor-metal contact where all the

depletion width is located in the p-type material. The flat band potential and carrier density can be calculated based on the Mott-Schottky equation:

$$C^{-2} = \frac{2(V_{fb} - V_{appl})}{A^2 q \epsilon \epsilon_0 N} \quad (6.2)$$

Where V_{fb} is the flat-band potential, V_{appl} is the applied bias, A corresponds to the cell area, ϵ is the relative permittivity of the CZTSSe, ϵ_0 is the vacuum permittivity and N represent the carrier density of CZTSSe.⁶¹ The capacitance obtained was at 5k AC frequency where most of the carriers are activated. The calculated carrier densities for cell-5, cell-6 and cell-7 are $1.4 \cdot 10^{16} \text{ cm}^{-3}$, $1.5 \cdot 10^{16} \text{ cm}^{-3}$ and $2.4 \cdot 10^{16} \text{ cm}^{-3}$ respectively, where no significant diversity was observed. Similar values of carrier density have been reported for both CIGSSe and CZTSSe solar cells with remarkable conversion efficiencies.⁹⁸⁻⁹⁹ These values of carrier densities indicate that the Fermi levels occupy similar relative positions with respect to the valence bands for all three CZTSSe absorbers. However, the flat band potential (V_{fb}) extracted are different (0.52 V, 0.54 V and 0.62 V for cell-5, cell-6 and cell-7 respectively). This parameter accounts for the difference of the Fermi levels at both sides of the p-n diode. Since both the buffer layer and the window layer can be considered identical for all three analyzed devices, V_{fb} can be a good indicator of the energetics alignment of the device.

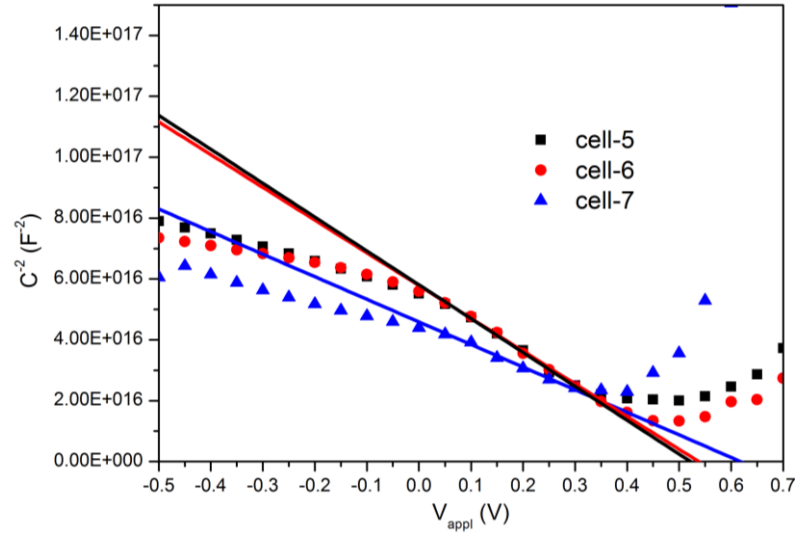


Figure 6-3 Mott-Schottky relation plot extracts the flat band potential at AC frequency 5k.

The V_{fb} difference is especially remarkable for cell-6 and cell-7 as they share the same band gap value but with 80 mV mismatch in the V_{fb} . Regarding the similar band gaps and carrier densities for cell-6 and cell-7, the origin of the V_{fb} variation can be attributed to a different energetics of the CZTSSe (since both n-type layers fabrication followed the same process which should result in identical Fermi level position), possibly originated by the difference in the selenization temperature during its formation. Therefore, two pathways of band alignment for cell-6 and cell-7, leading to different flat band potentials are illustrated in figure 6-4 for comparison. Figure 6-4 presents the proposed schematic energetic alignment pathway for the solar cell. As the carrier concentration of the CdS is considered at order of magnitude of 10^{17} cm^{-3} while the ZnO is in the range of $10^{18} - 10^{20} \text{ cm}^{-3}$, the CdS and i-ZnO can also form an n-n+ junction at their interface. Considering the thickness of both CdS and i-ZnO are less than 70 nm and highly doped Al:ZnO is using as the window layer, the band alignment is based on the Fermi level of the Al:ZnO. For Si based solar cell, the emitter can be simply defined as the n-Si which

is highly doped and directly contacting the p-Si absorber layer. In both chalcopyrite and kesterite solar cell, the emitter is hard to define as CdS and i-ZnO are acting as buffers, they are also n-type semiconductor who generate p-n junction with the absorber layers.

The preferential explanation is based on path (a) \rightarrow (b) as it can properly explain the flat band potential and carrier concentration obtained from impedance spectroscopy. The path (c) \rightarrow (d) can also explain the difference in flat band potentials for cell-6 and cell-7. However, in this case, the carrier concentration shall be remarkably different for the two CZTSSe absorbers, which contradicts the results obtained.

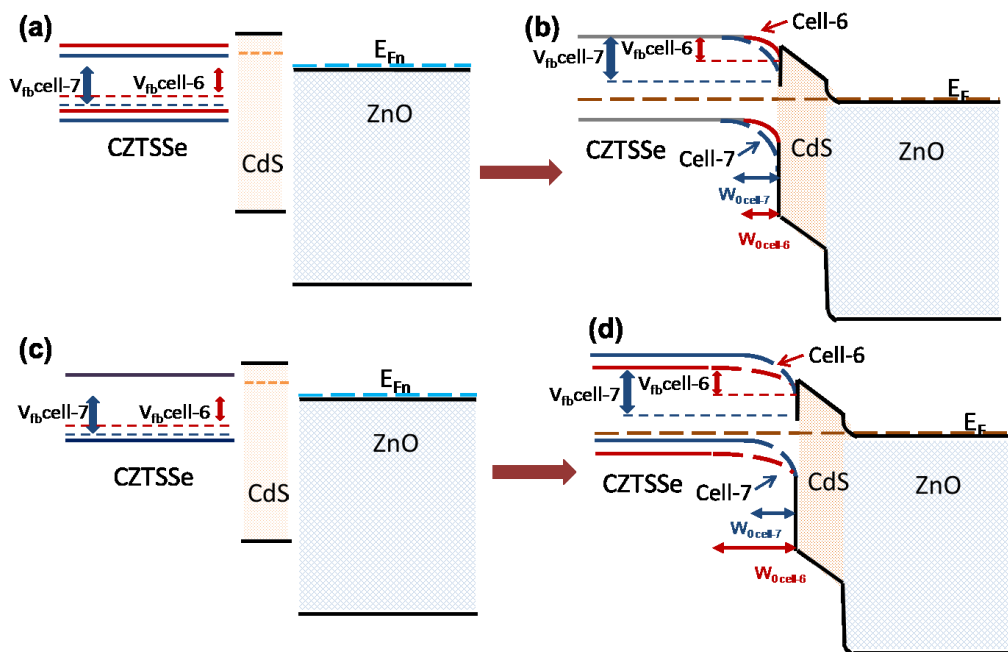


Figure 6-4 Proposed schematic energetic alignment pathway, from (a) \rightarrow (b) and from (c) \rightarrow (d), that satisfy the results of flat band potential calculation (considering same carrier concentration)

Similar to other kind of solar cells such as OPV,⁸⁷ the V_{fb} can be used to measure the relative positions of the energy levels, which directly affects the V_{oc} . From this perspective, the achieved V_{oc} can be related to the respective V_{fb} of individual cells, indicating that the energetics of the devices can be considered as one of primary factors determining the V_{oc} for this type of solar cells.

In this study, a higher flat band potential was observed for CZTSSe-7 than that of CZTSSe-5, which was consistent with the PL peak energy measurement results of the absorber layer. Both effects could lead to a higher V_{oc} for CZTSSe-7 cell. The V_{oc} was, to some extent, dependent on the barrier formed in the p-n junction. Thus, both photoluminescence and impedance spectroscopy analysis were essential to broaden the understanding of the V_{oc} of the kesterite solar cells. Further investigation is urgently demanded to unveil the detailed mechanism.

In addition, the aforementioned carrier density for both cell-6 and cell-7 are at the same level of $2 \cdot 10^{16} \text{ cm}^{-3}$. The carrier density is further extracted from different AC frequency conditions. As it is known that the CZTSSe absorber is a heavily doped and highly compensated semiconductor, deep acceptor defects levels exist in the forbidden energy band. The holes generated by these acceptor defects levels are responding to different AC frequency signals. The shallow defects carriers can respond to very high AC frequency but the deep defects carriers can only be reflected at low AC frequency. Thus, at low AC frequency, a higher carrier density should be observed than that of high AC frequency. As shown in the figure 6-5, this trend is clearly observed from the Mott-Schottky relation calculation. Both cell-6 and cell-7 reveal an increasing trend of carrier density towards lower AC frequency.

The increasing rate for cell-7 is more significant than cell-6, indicating more deep defects existing in cell-7 CZTSSe absorber layer. This can further validate the relatively lower recombination resistance obtained from cell-7, than that of cell-6. However, it is worth mentioning that even though the carrier density increment is different for cell-6 and cell-7, the overall carrier density remains in the same order of magnitude for both absorbers.

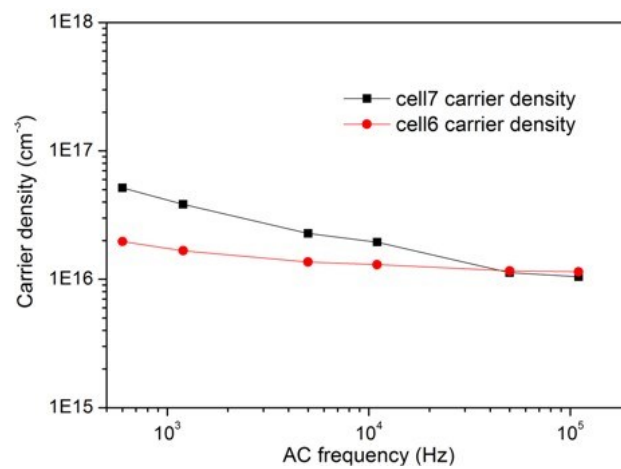


Figure 6-5 Carrier density calculated from different AC frequency impedance spectroscopy.

Meanwhile, the flat band potentials at different AC frequency have also been calculated based on the Mott-Schokkty equation shown in figure 6-6. It can be seen that the flat band potentials calculated from low AC frequency are in similar values, while as the AC frequency rises, so does the flat band potential. This phenomenon is not commonly observed from other types of solar cell such Si based and OPV. In this case, the increment of flat band potential can be explained by the deep defects levels existing in the forbidden energy band of CZTSSe absorber. These deep defects level are activated only at lower AC frequency so the presented quasi-Fermi level of the CZTSSe is affected by different AC frequency. In another words, the

band alignment of the p-n junction is based on the electron-hole diffusion. The junction capacitance charge and discharge effect is highly impacted by the AC frequency once deep defects carrier is presented. The differences of flat band potential for cell-6 and cell-7 are quite consistent at low frequency range, where most of the carriers are involved. It indicates a reasonable and reliable result obtained for explaining the energetics alignment in kesterite solar cells.

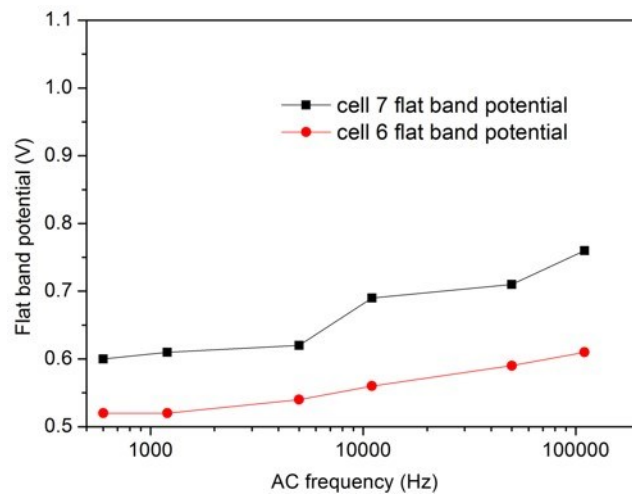


Figure 6-6 Flat band potentials calculated from different AC frequency impedance spectroscopy.

6.4 Summary

In this chapter, impedance spectroscopy was utilized to characterize the full device of kesterite solar cell. The solar cell was analyzed as a whole rather than a layer by layer structure. It helped deliver a more complete understanding of the solar cell.

The V_{oc} differentiation origin was discussed from a perspective of energetics alignment of the device. As the V_{oc} was affected by not only the recombination but

also the device energetics, both factors were derived from impedance spectra analysis. As a result, the energetics alignment presented a critical contribution to the V_{oc} achieved. Together, with the carrier densities obtained, the flat band potential calculated from Mott-Schottky relation was essential to reveal the energetics of the CZTSSe absorber and the band alignment of the device. It indicated a positive correlation to the V_{oc} . Therefore, the V_{oc} deficit problem for the kesterite solar cell is not solely derived from the recombination of both the bulk and interface, but the energetics alignment of the devices too. In summary, apart from the layer by layer recombination study, this work revealed another perspective to study the V_{oc} of the CZTSSe solar cell by using impedance spectroscopy.

Future work is required to reveal the relationship of the recombination and energetics alignment in the solar cell. Further characterization improvement can be obtained by comparing the impedance spectra under dark and illumination conditions. Temperature dependent measurement is also an option to study the carrier behavior in the device.

Chapter 7 CMTS_{Se} (M=Metal) Material

Development and Application in Solar Cell

CMTS_{Se} structure semiconductors draw increasing attention as the intrinsic problems of the CZTS_{Se} emerge. The concept for CMTS_{Se} is to replace the Zn with alternative metallic elements. It aims to modify the band structure and defects properties of I-II-IV-VI groups' semiconductors without compromising the optical and electrical advantages of the CZTS structure. In this way, it is expected to improve the solar cell performance. This chapter will focus on study the CMTS_{Se} material structure for potential solar cell absorbers. The reasoning of choosing this type of materials will be discussed with a comprehensive understanding of the advantages and disadvantages of kesterite materials property and its influence on the solar cell. The alternative CMTS_{Se} may broaden the horizon for viewing the I-II-IV-VI groups' semiconductors. I-II-IV-VI groups' compounds such as Cu₂CaSnS₄, Cu₂NiSnS₄, Cu₂MgSnS₄ and Cu₂MnSnS₄ are deposited by using the same spray pyrolysis technique as depositing CZTS film. The advantages for spray pyrolysis technique provide a feasible solution to deposit thin film with various non-toxic elements. The deposited films are further characterized to investigate the crystal structure compared to CZTS. The obtained films are processed further to a solar cell device by applying the same processes as CZTS_{Se} solar cell.

7.1 Investigation on CMTS_{Se} (M=Mg, Mn, Ni, Ca) as Potential Kesterite Absorbers.

The kesterite CZTSSe structure is derived from the chalcopyrite structure where the group III elements, In and Ga, are replaced by Zn(II) and Sn(IV). Hence, the advantageous properties for chalcopyrite semiconductor, such as high absorption coefficient and direct band gap, remains in the kesterite material.

The main problem existing in CZTSSe kesterite solar cell is the high V_{oc} deficit comparing to the CIGSSe chalcopyrite solar cell. The normal V_{oc} deficit for high efficiency chalcopyrite solar cell is around 500 mV, while for kesterite solar cells this value increases to more than 600 mV.¹⁰⁰⁻¹⁰⁷ The high V_{oc} deficit is originated from lower recombination activation energy of kesterite absorber compared to a chalcopyrite absorber. The CZTSSe material gives a much shorter minority carrier lifetime compared with the CIGSSe absorber,^{85, 108-110} and the deep acceptor defects levels are believed to contribute to this detrimental effect as well.

From theoretical calculations, the Cu_{Zn} antisite is the major acceptor defects existing in the CZTSSe while for chalcopyrite material, where a Cu vacancy is dominant.⁵² The Cu_{Zn} antisite possesses lower formation energy in the CZTSSe system than the Cu vacancy. Considering the Cu vacancy is a shallow defect while the Cu_{Zn} antisite occupies deeper positions in the forbidden energy band, the recombination energy is limited due to the DAPs transition of the carriers.

The reason for the low formation energy for a Cu_{Zn} antisite defect is the similar atomic size and electronic structure of Cu and Zn. Thus, the replacement of Zn by Cu is considered feasible.¹¹¹ This disorder effect has also been observed experimentally by other research groups.¹¹²⁻¹¹⁴ Therefore, replacing Zn by other

metallic elements with different atomic sizes and electronic structures is considered an option to solve the problem. By replacing the Zn with other metallic elements, the CMTS_{Se} will also possess kesterite structure, so that to reserve the advantageous optical and electrical properties of CZTS_{Se}. Due to the atomic size difference (figure 7-1), the Cu-M antisite formation energy should be increased, so that the concentration of defects will be reduced.

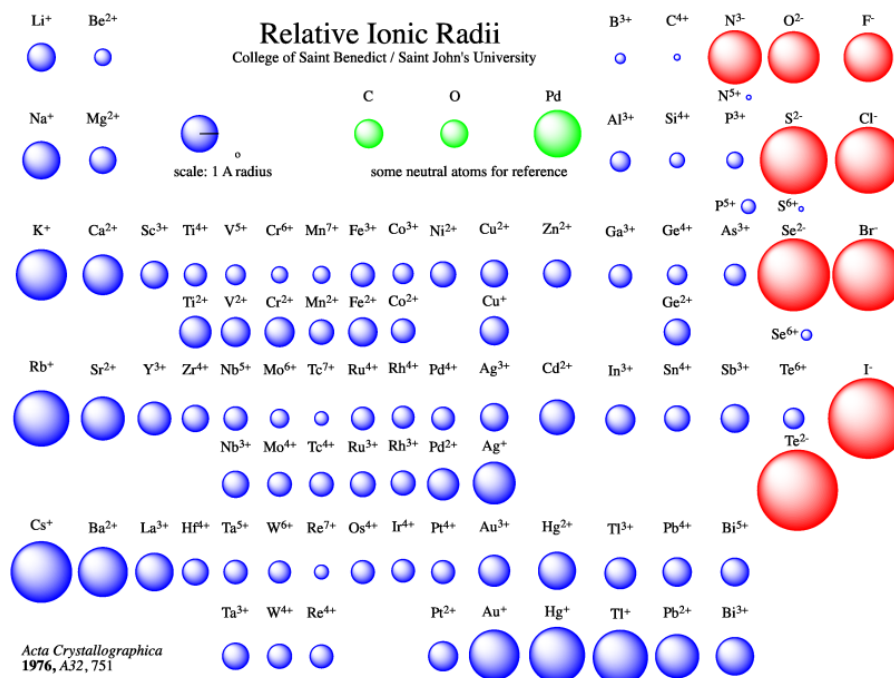


Figure 7-1 Relative ionic radii of atoms ¹¹¹

In addition, metallic elements chosen should also be non-toxic and earth abundant like Zn. ¹¹⁵ Figure 7-2, shows the cheaper and abundant elements such as Mn are good candidate for this study. Based on this analysis, some primary results have been established, indicating the feasibility of this substitution. ¹¹⁶⁻¹¹⁸

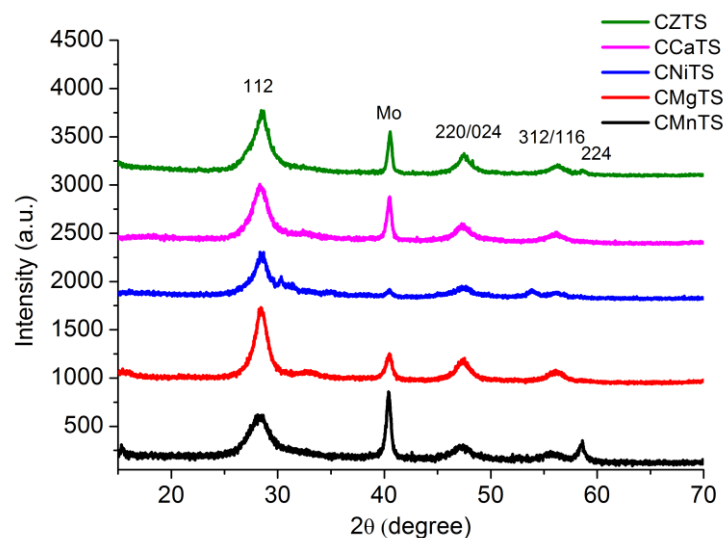


Figure 7-3 XRD curves of as-deposited CMTS (M=Ca, Ni, Mg, Mn) films by spray pyrolysis on Mo coated glass (with CZTS as reference)

After obtaining the film, high temperature selenization was conducted for each film with the sample setup as CZTS. Figure 7-4 shows much sharper peaks observed from the XRD pattern. The reflections at the positions of (112), (220/204) and (312/116) are shown in all CMTS_{Se}. However, only in the CMnTS_{Se} are the kesterite pattern peak (011) and (013) observed, confirming the presence of kesterite phase in CMnTS_{Se} film. In addition, small reflections emerge around 30°, which are also observed for CCaTS_{Se}, CNiTS_{Se} and CMgTS_{Se}. However, we are unable to identify the origin of this reflection. In CNiTS_{Se}, multiple reflections are observed which can be attributed to NiSe₂ phase.¹¹⁹⁻¹²⁰ Reflections at 29.8°, 33.5°, 36.8° and 50.1° correspond to the (220), (210), (211) and (311) diffraction planes from of Ni(SSe)₂. Even though the film CNiTS_{Se} is Ni rich, the observation of NiSe₂ indicates the difficulty in forming CNiTS_{Se} phase as the NiSe₂ is clearly separated and crystalline. This effect is not observed for other alternative substituted metals.

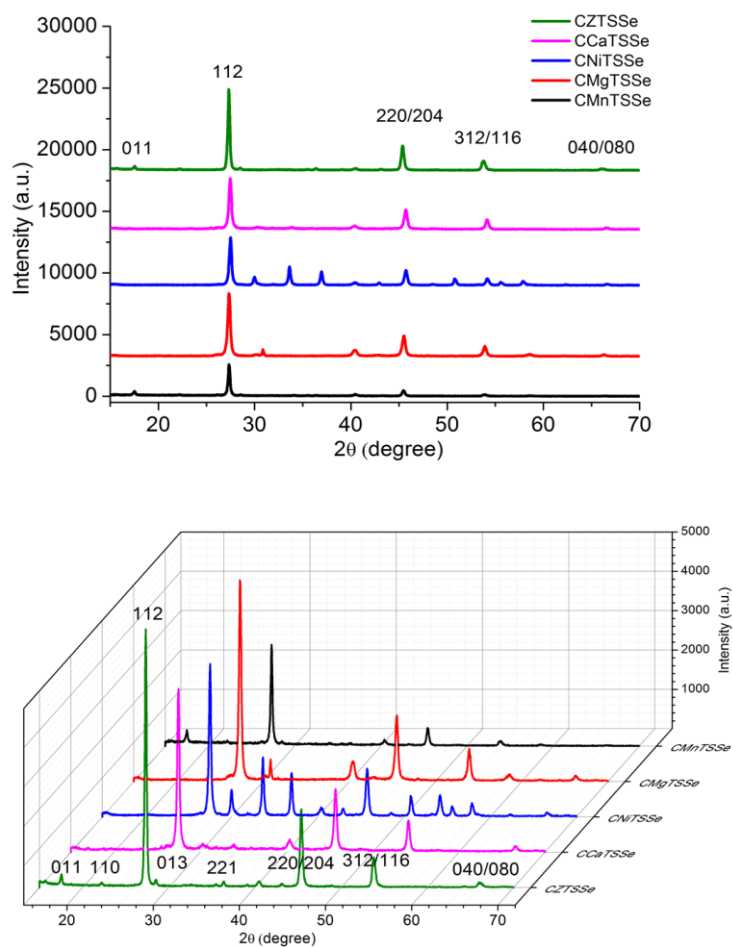


Figure 7-4 XRD curves (two views) of post-selenized CMTSSe (M= Ca, Ni, Mg, Mn) films (with CZTS as reference).

To further verify the phases of CMTSSe film, Raman spectroscopy has been applied for both CMTS and CMTSSe films. Figure 7-5 shows the as-deposited the Raman spectra for the CMTS films. For CZTS, a broad band at Raman shift of 333 cm^{-1} is observed, which is the A_1 mode of the kesterite phase but with low crystallinity. For CCaTS, apart from the small band at 333 cm^{-1} , two major bands at 290 cm^{-1} and 350 cm^{-1} are also observed. The two additional bands can be attributed to CTS-type phases,¹²¹⁻¹²² and indicate the major formation of CTS rather than CCaTS in the film. It was observed that the as-deposited CCaTS films absorb

moisture when exposed to the ambient condition of the laboratory. The film appeared to be deliquescent after half an hour, which is possibly due to the moisture affinity of Ca. The Ca in the film can easily absorb atmospheric H₂O to form Ca(OH)₂. In this case, the as-deposited film results in the CTS Raman shift.

For the CNiTS, CMgTS and CMnTS Raman spectra, the 290 cm⁻¹ and 350 cm⁻¹ are also observed as minor bands compared to band at the 333 cm⁻¹. It suggested the mixed formation of CMTS and CTS in the film. Compared to the CZTS Raman spectra where the CZTS phase is dominant, the formation of CMTS under spray temperature (270°C) is more challenging.

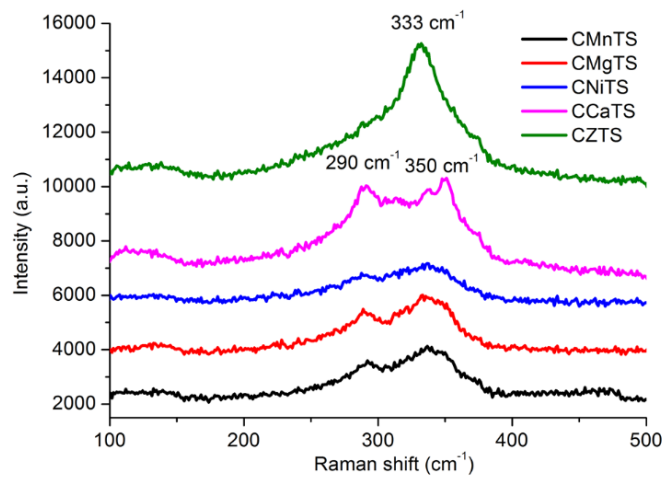


Figure 7-5 Raman spectra of as-deposited CMTS films

Figure 7-6 shows the Raman spectra of post-selenized CMTS_{Se} films. For CZTS_{Se}, bands at 179 cm⁻¹, 203 cm⁻¹ and 238 cm⁻¹ correspond to the A₁ mode vibration of CZTSe, and 327 cm⁻¹ corresponds to the A₁ mode of CZTS. The CCaTS_{Se} gives a broad major band centered at 192 cm⁻¹ which corresponds to the A₁ mode of CTS_{Se}. The two small bands at 240 cm⁻¹ and 256 cm⁻¹ also correspond to the A

mode of CTSSe.¹²³⁻¹²⁶ For CNiTSSe, the secondary phase Ni(SSe)₂ has already been detected from XRD analysis. From the Raman spectra, the band at 224 cm⁻¹ belongs to the A_g mode vibration of Ni(SSe)₂.¹²⁷ The broad band at 190 cm⁻¹ can be considered as the A₁ mode of CTSSe, similar to the CCaTSSe spectra. For CMgTSSe, the broad bands of 182 cm⁻¹ and 237 cm⁻¹ suggest the existence of CTSSe. However, it is not possible to identify other phases from the spectrum.¹²⁸⁻¹²⁹ The CMnTSSe shows pattern peaks of a two-mode behavior of kesterite material with mixture CMnTS and CMnTSe. The selenization process for CMnTS was not as extensive as for CZTS, so that to give a higher S/Se ratio in the CMnTSSe film. Similar behavior has been discussed in previous chapters 4.

Based on the Raman spectrum, the CMnTSSe can be proposed as a potential candidate for replacing CZTSSe as an absorber. The solid-solution of CMnTSSe appears to be kesterite phase without any detectable secondary phases. For other CMTSSe compounds, the presence of secondary phases due to the non-stoichiometry can lead to a detrimental effect on the solar cell performance. However, the elemental ratio applied is mimicking the CZTS initial ratio. Thus, further optimization is required in terms of elemental non-stoichiometry and selenization temperature for better understanding of the materials.

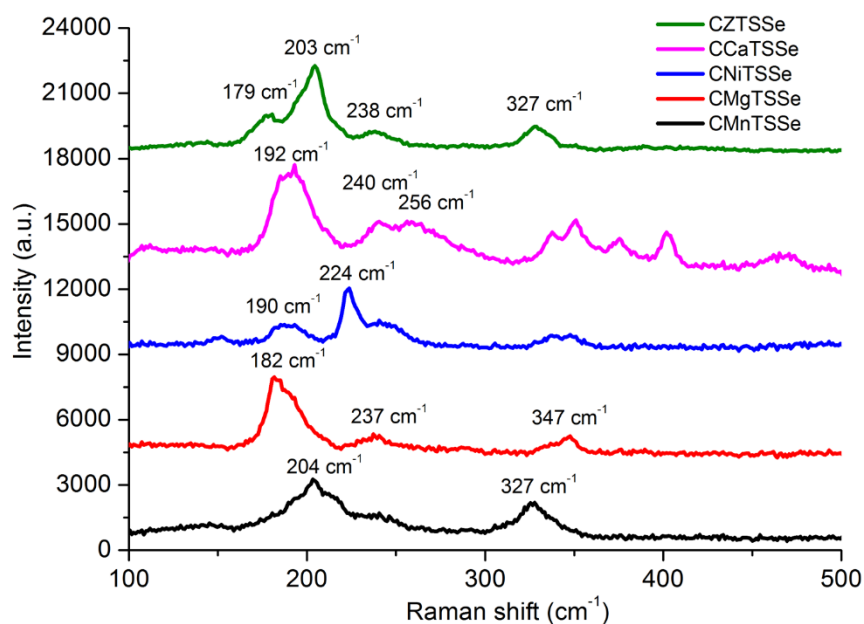


Figure 7-6 Raman spectra of post-selenized CMTSsSe compare to CZTSsSe with same selenization process.

Figure 7-7 shows the cross-sectional SEM image of the CMTSsSe films. The CMnTSsSe after selenization displays large grains on the Mo glass. Large grains are also observed for CCaTSsSe, however, as we have identified the CTSsSe phase dominating in the film, the grains cannot be simply addressed as CCaTSsSe. For both CMgTSsSe and CNiTSsSe small grains are observed, which may indicate further temperature increments during the selenization process to obtain larger grain sizes. Although the absorber quality cannot be simply judged by the grain size, large grain sizes are beneficial for the solar cell performance in general.^{32, 130-132}

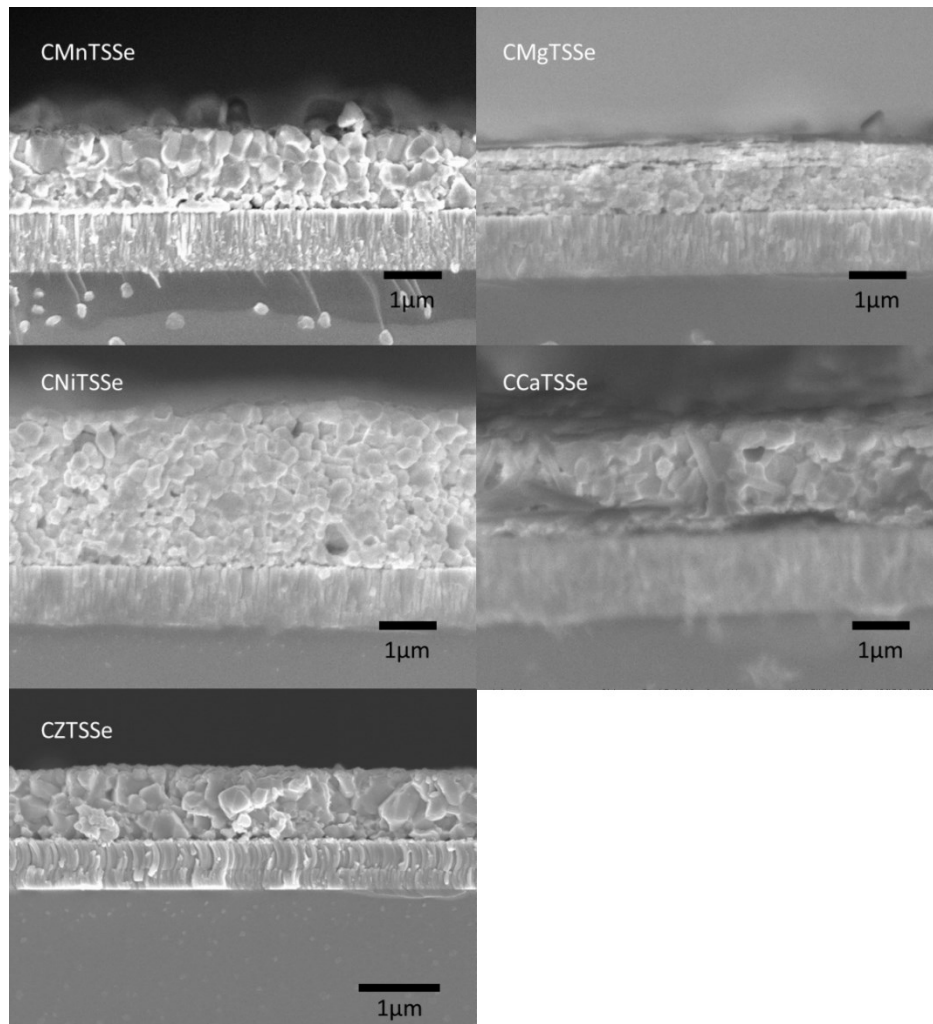


Figure 7-7 Cross-section FE-SEM image of post-selenized CMTSsSe comparing to CZTSsSe

7.3 Light J-V Measurement Discussion on CMTSsSe Solar Cells

The aforementioned CMTSsSe (M=Ni, Mn, Mg) films were used to replace the CZTSsSe as absorber layer in the solar cell. The remaining layers are identical to a CZTSsSe solar cell. Since the CCaTSsSe is highly water absorbing due to the presence of Ca, the film deteriorated after the CdS deposition. Figure 7-8 shows the J-V measurement of the solar cells under one sun at AM 1.5.

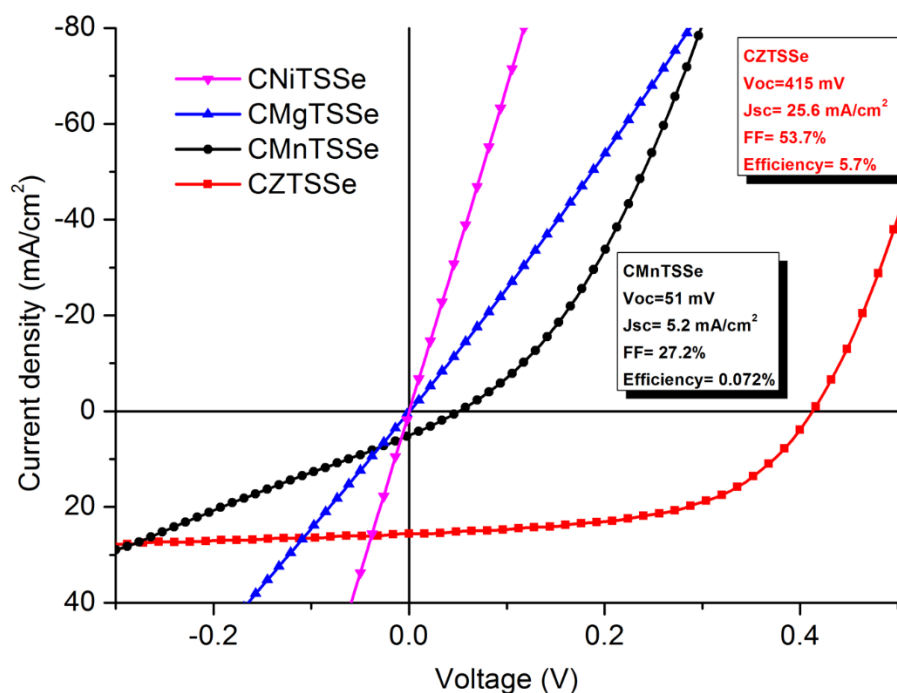


Figure 7-8 Light J-V curves of CMTSse (M=Ni, Mg, Mn) solar cells under one sun illumination comparing with CZTSSe solar cell

Among three CMTSse solar cells, only CMnTSse displayed PV behavior with a conversion efficiency of 0.072%. The solar cell illustrates a diode behavior from the J-V curve, indicating the formation of p-type CMnTSse absorber and p-n junction in the solar cell device. It can be observed that the current density increases significantly at reversed bias, meaning the solar cell suffers from an extensive shunting problem. Further optimization is required in terms of stoichiometric analysis and carrier properties to give an improved performance.

For CMgTSse and CNiTSse solar cell, no PV behavior was observed. The conductivity of the film is significant, which may due to the presence of secondary phases inside the film. Further optimization can focus primarily on fabricating high quality films of the quaternary compounds of CMgTSse and CNiTSse.

7.4 Summary

By replacing the Zn in CZTSSe with alternative metals (Ca, Mg, Mn, Ni), the CMTSSe can be fabricated using spray pyrolysis techniques. Primary characterizations were conducted to reveal the structures of the obtained films. Secondary phases were found to coexist with the CMTSSe (M=Ca, Mg, Ni), indicating the difficulty in forming quaternary compounds under current CZTSSe fabrication condition. Further fabrication improvement for these compounds can focus on the stoichiometric adjustment and selenization process.

In contrast, CMnTSSe solar cell achieved 0.072% efficiency with a clear diode behavior from the J-V curve. Although the shunting problem was noticeable, it presented potential for further optimization as an absorber. As this was primary trial experiment, a further study was required. To our best knowledge, it is the first time a kesterite solar cell has been obtained with CMTSSe as the absorber rather than CZTSSe.

Chapter 8 Conclusion and Prospects

8.1 Conclusion and Overall Summary

Kesterite CZTSSe materials presents promising optical and electrical properties to be considered as good light absorber in thin film solar cells. They are intrinsic p-type semiconductors with a direct band gap and high absorption coefficient. Kesterite solar cells have achieved more than 12% efficiency by using a hydrazine based solution technique, and more than 9% efficiency by vacuum based methodologies. Replacing the In in CISSe by Zn and Sn, the In-free CZTSSe absorber can further reduce the material costs so that to be comparable to CIGSSe chalcopyrite solar cell, which has been industrialized and developed in the PV marketplace.

However, the current fabrication techniques for high quality CZTSSe absorber involve either hazardous solvents such as hydrazine, methanol and dimethyl sulfoxide (DMSO), or high vacuum conditions. Developing a green and cost-effective technique to fabricate high quality CZTSSe absorber is in highly demand. Following this current work, an aqueous solution spray pyrolysis has been introduced into this field. Spray pyrolysis is a green and scalable technique, which can be operated at ambient conditions with low equipment needs and power costs.

In this work, the CZTS film was deposited on Mo coated glass by aqueous solution spray pyrolysis. A uniform coated CZTS film was obtained on Mo coated glass without carbon residues. After high temperature selenization under

atmosphere pressure, a high quality CZTSSe absorber could be achieved. The emitter and window layers fabrication followed the standard protocols as chalcopyrite solar cell.

The obtained CZTSSe absorber underwent XRD and Raman spectroscopy studies to detect the phase purity. No traceable secondary phases were detected under the experimental procedures applied. SIMS depth profile indicated a uniform distribution of Cu, Sn and Se throughout the film, while the Zn and S concentrations increased slightly towards the CZTSSe/Mo interface. This result indicated the possibility of Zn based binary phase coexisting inside the film, although it may act only as a dark region in the solar cell.

Solar cell devices based on this absorber achieved a 7.5% conversion efficiency with $V_{oc} = 427$ mV, $J_{sc} = 28.7$ mA/cm² and FF = 61% without an antireflection layer. The band gap of the CZTSSe absorber was calculated from EQE at $E_g = 1.16$ eV, which indicated a V_{oc} deficit more than 730 mV. The V_{oc} deficit is very high compared to the champion kesterite and chalcopyrite solar cells, which are around 600 mV and 500 mV respectively. The high V_{oc} deficit for kesterite solar cell compared to that of chalcopyrite solar cell is a significantly limiting factor towards the solar cell performance. Therefore, a strong motivation emerged to study the recombination behavior in the CZTSSe absorber in more detail.

Temperature dependent and power dependent PL spectroscopy were conducted to study the carrier recombination effects. The temperature dependent PL spectra gave a consistent peak position with a lower energy than the band gap

of the CZTSSe. It revealed the DAPs transition occurs for the carrier recombination. The power dependent PL spectra further confirmed the defects involving in the recombination process by power law fitting of the PL intensity. Furthermore, significant temperature quenching effect was observed from the PL spectra. The origin of the quenching effect was the activation of non-radiative channel for the carrier recombination. Modification of the selenization process presented an improvement on limiting the non-radiative recombination. As the CZTSSe absorber is an intrinsically heavily doped and highly compensated semiconductor, the DAPs transition lowers the recombination activation energy, so that the V_{oc} is suppressed. The non-radiative recombination promotes the carrier recombination via heat transfer, which is detrimental to the minority carrier lifetime. Thus, the V_{oc} can be further reduced.

The V_{oc} deficit was also studied from the perspective of the energetics alignment of the diode p-n junction. Three kesterite solar cells with similar J_{sc} were measured by impedance spectroscopy. In this case, the solar cells were considered as an entity to fit the diode circuit. For two cells (cell-6 and cell-7) with similar band gaps, the V_{oc} difference was as much as 50 mV. The recombination resistance obtained from impedance spectra of cell-7 was less than that of cell-6, which cannot properly explain the fact that cell-7 possessed a higher V_{oc} than cell-6. Further study of the Mott-Schottky relation revealed similar carrier concentrations for both absorbers. However, the flat band potential for cell-7 was 80 mV larger than that of cell-6. This was considered as one of the critical factors resulting in the difference in V_{oc} .

The deep defects levels such as a Cu_{Zn} antisite defect contribute to the high V_{oc} deficit, as the DAPs transition is dominating in the carrier recombination of CZTSSe absorber. The reasoning of the low formation energy of Cu_{Zn} antisite is the similarity of their atomic sizes and electronic configuration. Therefore, alternative metals were used to replace Zn in CZTSSe. In this study, among the four CMTSSe ($\text{M}=\text{Ca}, \text{Ni}, \text{Mg}, \text{Mn}$) absorbers fabricated by spray pyrolysis technique, the CMnTSSe shows a promising kesterite-type structure without any detectable secondary phases in the film. The remaining CMTSSe absorbers presented binary or tertiary phases, which were detrimental to the solar cell performance. The solar cell based on CMnTSSe absorber obtained a 0.07% conversion efficiency with a clear diode behavior of the device, while the reference CZTSSe solar cell was 5.7% in comparison. Even though the CMnTSSe solar cell performance was not comparable to the CZTSSe solar cell, this preliminary result indicated a potential direction to study the kesterite absorbers. The clear diode behavior inside the CMnTSSe solar cell presented itself as an intrinsic p-type semiconductor.

8.2 Future Work Recommendation

This research work described in this thesis presents a green technique to fabricated kesterite solar cells. The V_{oc} of the solar cells were investigated and analyzed in terms of absorber carrier recombination behavior and device energetics alignment. It was aimed to improve the kesterite solar cell performance by understanding its unique optical and electrical properties. The future work is recommended in the following fields.

8.2.1 Analyze the Illumination Difference between the Absorber and Device

The carrier recombination behavior in the semiconducting absorber layer can be detected by using PL spectroscopy. By comparing the PL intensity from the device and bulk absorber, the front interface recombination and charges separation can be estimated. Under open circuit condition, the excited minority carrier cannot flow through the p-n junction after reaching equilibrium at the beginning of the illumination. By comparing the intensity difference to the bulk absorber, the interface recombination can be estimated. Furthermore, under short circuit conditions, the excited minority carrier from the absorber will immediately flow through the depletion region to the emitter so that the PL intensity will drop accordingly. The reduction of the PL intensity can be attributed to the charge separation. In this case, the effectiveness of charge separation can be extracted from the comparison of the PL intensity under OC and SC conditions. Besides this, the TRPL spectroscopy can also be applied under same assumption to investigate the minority carrier lifetime under aforementioned conditions.

8.2.2 Investigate the Back Surface Field for Kesterite Solar Cell

The back surface field (BSF) is critical for solar cell performance as it involves the carrier recombination in the absorber. The BSF has been studied for Si based solar cell for many decades.¹³³⁻¹³⁶ The Mo back contact for kesterite solar cell is providing a Shockley contact at the Mo/CZTSSe interface. The electric field can restrict the carrier movement in the bulk of CZTSSe absorber. The recombination

at the back surface is one of the critical limiting factors for the V_{oc} and J_{sc} of the solar cell.

In this case, by applying configuration shown in figure 8-1 to the device, the Mo/CZTSSe Shockley barrier can be isolated and investigated by impedance spectroscopy. Together with the J-V measurements, the impedance spectra can be analyzed via Mott-Schottky relation to illustrate the barrier effects of the Mo back contact. In addition, the $Mo(SSe)_2$ effect can also be studied by this configuration.

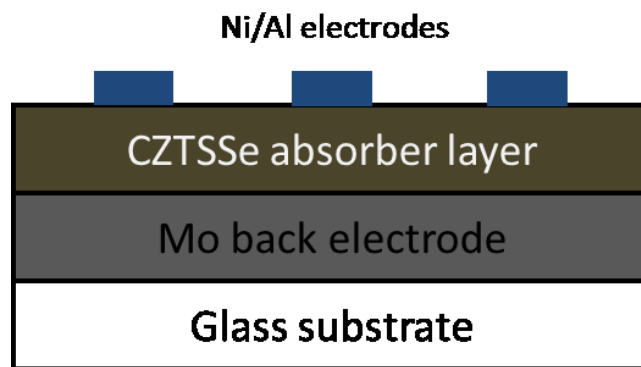


Figure 8-1 configuration for back surface field study by impedance spectroscopy

8.2.3 Investigate the Impedance Behavior of the Solar Cell under Different Illumination Conditions.

Impedance spectroscopy can be applied under different illumination conditions to disclose the electrical properties of solar cells. Different illumination intensities give different excited carrier concentrations. For different excitation wavelength, the exciting depth and carrier mobility are changing (figure 8-2). The carrier lifetime based on each condition can be extracted from the Nyquist plots. The carrier lifetime comparison can further illustrate the overall recombination behavior in the

solar cell. The study on the series and recombination resistance can improve the understanding of diode properties and capacitance behavior of the device. The carrier concentrations can be extracted from dark and light conditions, so that the excited carrier concentrations can be obtained to further study the current density of the solar cell. Temperature variation can also be applied to the solar cell to enable a more comprehensive understanding of the operating mechanisms.

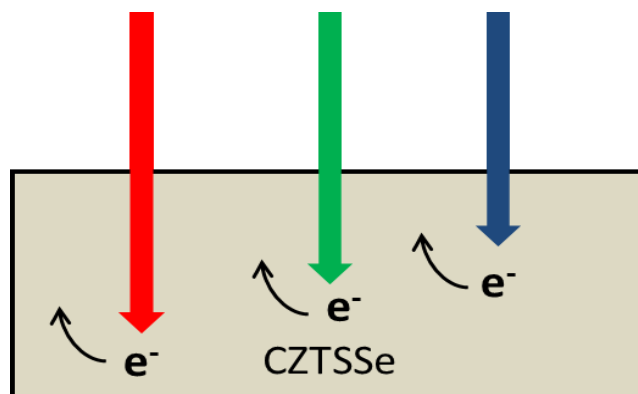


Figure 8-2 Schematic illustration of light wavelength dependence on penetration depth

8.2.4 Tuning the Band Gap by Cation Incorporation and Replacement

By incorporating Ga into the CISSe absorber, the band gap can be tuning to the optimum value so as to achieve more than 20% conversion efficiency for chalcopyrite solar cell. For CZTSSe absorber, the primary study replacing Sn with Ge has similarly achieved the band tuning effect. However, the conversion efficiency did not show remarkable improvement. Further study on incorporating metals with oxidation state of +3 such as Al and Ga can be considered as alternative options. Replacing Zn with other metal elements such as Mn or Cd is also worthy of study, so as to follow on from the promising initial results described in this work.

Reference

1. Chapin, D. M.; Fuller, C. S.; Pearson, G. L., A New Silicon p-n Junction Photocell for Converting Solar Radiation into Electrical Power. *Journal of Applied Physics* **1954**, 25 (5), 676.
2. Abermann, S., Non-vacuum processed next generation thin film photovoltaics: Towards marketable efficiency and production of CZTS based solar cells. *Solar Energy* **2013**, 94, 37-70.
3. Azimi, H.; Hou, Y.; Brabec, C. J., Towards low-cost, environmentally friendly printed chalcopyrite and kesterite solar cells. *Energy & Environmental Science* **2014**, 7 (6), 1829.
4. Jackson, P.; Würz, R.; Rau, U.; Mattheis, J.; Kurth, M.; Schlötzer, T.; Bilger, G.; Werner, J. H., High quality baseline for high efficiency, Cu(In_{1-x}Ga_x)Se₂ solar cells. *Progress in Photovoltaics: Research and Applications* **2007**, 15 (6), 507-519.
5. Jaffe, J.; Zunger, A., Theory of the band-gap anomaly in ABC₂ chalcopyrite semiconductors. *Physical Review B* **1984**, 29 (4), 1882-1906.
6. Chirila, A.; Buecheler, S.; Pianezzi, F.; Bloesch, P.; Gretener, C.; Uhl, A. R.; Fella, C.; Kranz, L.; Perrenoud, J.; Seyrling, S.; Verma, R.; Nishiwaki, S.; Romanyuk, Y. E.; Bilger, G.; Tiwari, A. N., Highly efficient Cu(In,Ga)Se₂ solar cells grown on flexible polymer films. *Nat Mater* **2011**, 10 (11), 857-61.
7. Reinhard, P.; Pianezzi, F.; Kranz, L.; Nishiwaki, S.; Chirilă, A.; Buecheler, S.; Tiwari, A. N., Flexible Cu(In,Ga)Se₂ solar cells with reduced absorber thickness. *Progress in Photovoltaics: Research and Applications* **2013**, n/a-n/a.
8. Yagioka, T.; Nakada, T., Cd-Free Flexible Cu(In,Ga)Se₂ Thin Film Solar Cells with ZnS(O,OH) Buffer Layers on Ti Foils. *Applied Physics Express* **2009**, 2, 072201.
9. Rockett, A. A., Current status and opportunities in chalcopyrite solar cells. *Current Opinion in Solid State and Materials Science* **2010**, 14 (6), 143-148.
10. Green, M. A.; Emery, K.; Hishikawa, Y.; Warta, W.; Dunlop, E. D., Solar cell efficiency tables (version 44). *Progress in Photovoltaics: Research and Applications* **2014**, 22 (7), 701-710.
11. Chen, S.; Walsh, A.; Yang, J.-H.; Gong, X. G.; Sun, L.; Yang, P.-X.; Chu, J.-H.; Wei, S.-H., Compositional dependence of structural and electronic properties of Cu₂ZnSn(S,Se)₄ alloys for thin film solar cells. *Physical Review B* **2011**, 83 (12).
12. Wang, W.; Winkler, M. T.; Gunawan, O.; Gokmen, T.; Todorov, T. K.; Zhu, Y.; Mitzi, D. B., Device Characteristics of CZTSSe Thin-Film Solar Cells with 12.6% Efficiency. *Advanced Energy Materials* **2013**, n/a-n/a.
13. Repins, I.; Beall, C.; Vora, N.; DeHart, C.; Kuciauskas, D.; Dippo, P.; To, B.; Mann, J.; Hsu, W.-C.; Goodrich, A.; Noufi, R., Co-evaporated Cu₂ZnSnSe₄ films and devices. *Solar Energy Materials and Solar Cells* **2012**, 101, 154-159.
14. Mitzi, D. B.; Gunawan, O.; Todorov, T. K.; Wang, K.; Guha, S., The path towards a high-performance solution-processed kesterite solar cell. *Solar Energy Materials and Solar Cells* **2011**, 95 (6), 1421-1436.
15. Walsh, A.; Chen, S.; Wei, S.-H.; Gong, X.-G., Kesterite Thin-Film Solar Cells: Advances in Materials Modelling of Cu₂ZnSnS₄. *Advanced Energy Materials* **2012**, 2 (4), 400-409.
16. Barkhouse, D. A. R.; Haight, R.; Sakai, N.; Hiroi, H.; Sugimoto, H.; Mitzi, D. B., Cd-free buffer layer materials on Cu₂ZnSn(S_xSe_{1-x})₄: Band alignments with ZnO, ZnS, and In₂S₃. *Applied Physics Letters* **2012**, 100 (19), 193904.

17. Yan, C.; Liu, F.; Song, N.; Ng, B. K.; Stride, J. A.; Tadich, A.; Hao, X., Band alignments of different buffer layers (CdS, Zn(O,S), and In₂S₃) on Cu₂ZnSnS₄. *Applied Physics Letters* **2014**, *104* (17), 173901.
18. Htay, M. T.; Hashimoto, Y.; Momose, N.; Sasaki, K.; Ishiguchi, H.; Igarashi, S.; Sakurai, K.; Ito, K., A Cadmium-Free Cu₂ZnSnS₄/ZnO Heterojunction Solar Cell Prepared by Practicable Processes. *Japanese Journal of Applied Physics* **2011**, *50*, 032301.
19. Nielsen, T. D.; Cruickshank, C.; Foged, S.; Thorsen, J.; Krebs, F. C., Business, market and intellectual property analysis of polymer solar cells. *Solar Energy Materials and Solar Cells* **2010**, *94* (10), 1553-1571.
20. Espinosa, N.; Hosel, M.; Angmo, D.; Krebs, F. C., Solar cells with one-day energy payback for the factories of the future. *Energy & Environmental Science* **2012**, *5* (1), 5117-5132.
21. Jackson, P.; Hariskos, D.; Lotter, E.; Paetel, S.; Wuerz, R.; Menner, R.; Wischmann, W.; Powalla, M., New world record efficiency for Cu(In,Ga)Se₂ thin-film solar cells beyond 20%. *Progress in Photovoltaics: Research and Applications* **2011**, *19* (7), 894-897.
22. Kranz, L.; Gretener, C.; Perrenoud, J.; Schmitt, R.; Pianezzi, F.; La Mattina, F.; Blösch, P.; Cheah, E.; Chirilă, A.; Fella, C. M.; Hagendorfer, H.; Jäger, T.; Nishiwaki, S.; Uhl, A. R.; Buecheler, S.; Tiwari, A. N., Doping of polycrystalline CdTe for high-efficiency solar cells on flexible metal foil. *Nat Commun* **2013**, *4*.
23. Ferry, V. E.; Verschuuren, M. A.; Lare, M. C. v.; Schropp, R. E. I.; Atwater, H. A.; Polman, A., Optimized Spatial Correlations for Broadband Light Trapping Nanopatterns in High Efficiency Ultrathin Film a-Si:H Solar Cells. *Nano letters* **2011**, *11* (10), 4239-4245.
24. Morales-Acevedo, A., Effective absorption coefficient for graded band-gap semiconductors and the expected photocurrent density in solar cells. *Solar Energy Materials and Solar Cells* **2009**, *93* (1), 41-44.
25. Chirilă, A.; Buecheler, S.; Pianezzi, F.; Bloesch, P.; Gretener, C.; Uhl, A. R.; Fella, C.; Kranz, L.; Perrenoud, J.; Seyrling, S.; Verma, R.; Nishiwaki, S.; Romanyuk, Y. E.; Bilger, G.; Tiwari, A. N., Highly efficient Cu(In,Ga)Se₂ solar cells grown on flexible polymer films. *Nat Mater* **2011**, *10* (11), 857-861.
26. Caballero, R.; Kaufmann, C. A.; Eisenbarth, T.; Unold, T.; Klenk, R.; Schock, H.-W., High efficiency low temperature grown Cu(In,Ga)Se₂ thin film solar cells on flexible substrates using NaF precursor layers. *Progress in Photovoltaics: Research and Applications* **2011**, *19* (5), 547-551.
27. Bag, S.; Gunawan, O.; Gokmen, T.; Zhu, Y.; Todorov, T. K.; Mitzi, D. B., Low band gap liquid-processed CZTSe solar cell with 10.1% efficiency. *Energy & Environmental Science* **2012**, *5* (5), 7060.
28. Todorov, T. K.; Reuter, K. B.; Mitzi, D. B., High-efficiency solar cell with Earth-abundant liquid-processed absorber. *Adv Mater* **2010**, *22* (20), E156-9.
29. Miskin, C. K.; Yang, W.-C.; Hages, C. J.; Carter, N. J.; Joglekar, C. S.; Stach, E. A.; Agrawal, R., 9.0% efficient Cu₂ZnSn(S,Se)₄ solar cells from selenized nanoparticle inks. *Progress in Photovoltaics: Research and Applications* **2014**, n/a-n/a.
30. Hages, C. J.; Levencio, S.; Miskin, C. K.; Alsmeyer, J. H.; Abou-Ras, D.; Wilks, R. G.; Bär, M.; Unold, T.; Agrawal, R., Improved performance of Ge-alloyed CZTGeSSe thin-film solar cells through control of elemental losses. *Progress in Photovoltaics: Research and Applications* **2013**, n/a-n/a.
31. Cao, Y.; Denny, M. S., Jr.; Caspar, J. V.; Farneth, W. E.; Guo, Q.; Ionkin, A. S.; Johnson, L. K.; Lu, M.; Malajovich, I.; Radu, D.; Rosenfeld, H. D.; Choudhury, K. R.; Wu, W., High-efficiency solution-processed Cu₂ZnSn(S,Se)₄ thin-film solar cells prepared from binary and ternary nanoparticles. *J Am Chem Soc* **2012**, *134* (38), 15644-7.

32. Shin, B.; Gunawan, O.; Zhu, Y.; Bojarczuk, N. A.; Chey, S. J.; Guha, S., Thin film solar cell with 8.4% power conversion efficiency using an earth-abundant Cu₂ZnSnS₄ absorber. *Progress in Photovoltaics: Research and Applications* **2013**, 21 (1), 72-76.
33. Brammertz, G.; Buffière, M.; Oueslati, S.; ElAnzeery, H.; Ben Messaoud, K.; Sahayaraj, S.; Köble, C.; Meuris, M.; Poortmans, J., Characterization of defects in 9.7% efficient Cu₂ZnSnSe₄-CdS-ZnO solar cells. *Applied Physics Letters* **2013**, 103 (16), 163904.
34. Gunawan, O.; Todorov, T. K.; Mitzi, D. B., Loss mechanisms in hydrazine-processed Cu₂ZnSn(Se,S)₄ solar cells. *Applied Physics Letters* **2010**, 97 (23), 233506.
35. Redinger, A.; Mousel, M.; Djemour, R.; Gütay, L.; Valle, N.; Siebentritt, S., Cu₂ZnSnSe₄ thin film solar cells produced via co-evaporation and annealing including a SnSe₂ capping layer. *Progress in Photovoltaics: Research and Applications* **2014**, 22 (1), 51-57.
36. Schmidt, T.; Lischka, K.; Zulehner, W., Excitation-power dependence of the near-band-edge photoluminescence of semiconductors. *Physical Review B* **1992**, 45 (16), 8989-8994.
37. Leitão, J. P.; Santos, N. M.; Fernandes, P. A.; Salomé, P. M. P.; da Cunha, A. F.; González, J. C.; Ribeiro, G. M.; Matinaga, F. M., Photoluminescence and electrical study of fluctuating potentials in Cu₂ZnSnS₄-based thin films. *Physical Review B* **2011**, 84 (2).
38. Grossberg, M.; Krustok, J.; Timmo, K.; Altosaar, M., Radiative recombination in Cu₂ZnSnSe₄ monograins studied by photoluminescence spectroscopy. *Thin Solid Films* **2009**, 517 (7), 2489-2492.
39. Grossberg, M.; Krustok, J.; Raudoja, J.; Timmo, K.; Altosaar, M.; Raadik, T., Photoluminescence and Raman study of Cu₂ZnSn(S_{1-x}Se_x)₄ monograins for photovoltaic applications. *Thin Solid Films* **2011**, 519 (21), 7403-7406.
40. Singh, A.; Singh, S.; Levchenko, S.; Unold, T.; Laffir, F.; Ryan, K. M., Compositionally tunable photoluminescence emission in Cu₂ZnSn(S_{1-x}Se_x)₄ nanocrystals. *Angew Chem Int Ed Engl* **2013**, 52 (35), 9120-4.
41. Krustok, J.; Jagomägi, A.; Raudoja, J.; Altosaar, M., Photoluminescence properties of stoichiometric CuInSe₂ crystals. *Solar Energy Materials and Solar Cells* **2003**, 79 (3), 401-408.
42. Shirakata, S.; Ohkubo, K.; Ishii, Y.; Nakada, T., Effects of CdS buffer layers on photoluminescence properties of Cu(In,Ga)Se₂ solar cells. *Solar Energy Materials and Solar Cells* **2009**, 93 (6-7), 988-992.
43. Puyvelde, L. V.; Lauwaert, J.; Pianezzi, F.; Nishiwaki, S.; Smet, P. F.; Poelman, D.; Tiwari, A. N.; Vrielinck, H., Influence of an Sb doping layer in CIGS thin-film solar cells: a photoluminescence study. *Journal of Physics D: Applied Physics* **2014**, 47 (4), 045102.
44. Shirakata, S.; Ohkubo, K.; Ishii, Y.; Nakada, T., Effects of CdS buffer layers on photoluminescence properties of Cu(In,Ga)Se₂ solar cells. *Solar Energy Materials and Solar Cells* **2009**, 93 (6-7), 988-992.
45. Harris, T. D., Photoluminescence of bulk and epitaxial GaAs. *Journal of Crystal Growth* **1988**, 89 (1), 21-27.
46. Nathan, M. I.; Burns, G.; Blum, S. E.; Marinace, J. C., Electroluminescence and Photoluminescence of GaAs at 77°K. *Physical Review* **1963**, 132 (4), 1482-1485.
47. Liu, C. Y.; Yuan, S.; Dong, J. R.; Chua, S. J., Temperature dependence of photoluminescence intensity from AlGaInP/GaInP multi-quantum well laser structures. *Journal of Crystal Growth* **2004**, 268 (3-4), 426-431.
48. Ning, J. Q.; Xu, S. J.; Deng, Z.; Su, Z. C., Polarized and non-polarized photoluminescence of GaInP₂ alloy with partial CuPt-type atomic ordering: ordered domains vs. disordered regions. *Journal of Materials Chemistry C* **2014**, 2 (30), 6119-6124.
49. Chen, S.; Gong, X. G.; Walsh, A.; Wei, S.-H., Defect physics of the kesterite thin-film solar cell absorber Cu₂ZnSnS₄. *Applied Physics Letters* **2010**, 96 (2), 021902.

50. Chen, S.; Walsh, A.; Luo, Y.; Yang, J.-H.; Gong, X. G.; Wei, S.-H., Wurtzite-derived polytypes of kesterite and stannite quaternary chalcogenide semiconductors. *Physical Review B* **2010**, *82* (19).
51. Chen, S.; Yang, J.-H.; Gong, X. G.; Walsh, A.; Wei, S.-H., Intrinsic point defects and complexes in the quaternary kesterite semiconductor $\text{Cu}_{2}\text{ZnSnS}_{4}$. *Physical Review B* **2010**, *81* (24).
52. Chen, S.; Wang, L.-W.; Walsh, A.; Gong, X. G.; Wei, S.-H., Abundance of $\text{CuZn} + \text{SnZn}$ and $2\text{CuZn} + \text{SnZn}$ defect clusters in kesterite solar cells. *Applied Physics Letters* **2012**, *101* (22), 223901.
53. Chen, S.; Walsh, A.; Gong, X. G.; Wei, S. H., Classification of lattice defects in the kesterite $\text{Cu}_{2}\text{ZnSnS}_{4}$ and $\text{Cu}_{2}\text{ZnSnSe}_{4}$ earth-abundant solar cell absorbers. *Adv Mater* **2013**, *25* (11), 1522-39.
54. Chen, S.; Gong, X. G.; Walsh, A.; Wei, S.-H., Crystal and electronic band structure of $\text{Cu}_{2}\text{ZnSnX}_{4}$ ($\text{X}=\text{S}$ and Se) photovoltaic absorbers: First-principles insights. *Applied Physics Letters* **2009**, *94* (4), 041903.
55. Chen, S.; Gong, X.; Walsh, A.; Wei, S.-H., Electronic structure and stability of quaternary chalcogenide semiconductors derived from cation cross-substitution of II-VI and I-III-VI₂ compounds. *Physical Review B* **2009**, *79* (16).
56. Macdonald, J. R.; Johnson, W. B., Fundamentals of Impedance Spectroscopy. In *Impedance Spectroscopy*, John Wiley & Sons, Inc.: 2005; pp 1-26.
57. Proskuryakov, Y. Y.; Durose, K.; Al Turkestani, M. K.; Mora-Seró, I.; Garcia-Belmonte, G.; Fabregat-Santiago, F.; Bisquert, J.; Barrioz, V.; Lamb, D.; Irvine, S. J. C.; Jones, E. W., Impedance spectroscopy of thin-film CdTe/CdS solar cells under varied illumination. *Journal of Applied Physics* **2009**, *106* (4), 044507.
58. Adachi, M.; Sakamoto, M.; Jiu, J.; Ogata, Y.; Isoda, S., Determination of Parameters of Electron Transport in Dye-Sensitized Solar Cells Using Electrochemical Impedance Spectroscopy. *The Journal of Physical Chemistry B* **2006**, *110* (28), 13872-13880.
59. Wang, Q.; Moser, J.-E.; Grätzel, M., Electrochemical Impedance Spectroscopic Analysis of Dye-Sensitized Solar Cells. *The Journal of Physical Chemistry B* **2005**, *109* (31), 14945-14953.
60. Mora-Seró, I.; Garcia-Belmonte, G.; Boix, P. P.; Vázquez, M. A.; Bisquert, J., Impedance spectroscopy characterisation of highly efficient silicon solar cells under different light illumination intensities. *Energy & Environmental Science* **2009**, *2* (6), 678.
61. Boix, P. P.; Garcia-Belmonte, G.; Muñecas, U.; Neophytou, M.; Waldauf, C.; Pacios, R., Determination of gap defect states in organic bulk heterojunction solar cells from capacitance measurements. *Applied Physics Letters* **2009**, *95* (23), 233302.
62. Sugiyama, M.; Hayashi, M.; Yamazaki, C.; Hamidon, N. B.; Hirose, Y.; Itagaki, M., Application of impedance spectroscopy to investigate the electrical properties around the pn interface of Cu(In,Ga)Se_{2} solar cells. *Thin Solid Films* **2013**, *535*, 287-290.
63. Bayhan, H.; Sertap Kavasoglu, A., Study of $\text{CdS/Cu(In,Ga)Se}_{2}$ heterojunction interface using admittance and impedance spectroscopy. *Solar Energy* **2006**, *80* (9), 1160-1164.
64. Cai, Y.; Ho, J. C.; Batabyal, S. K.; Liu, W.; Sun, Y.; Mhaisalkar, S. G.; Wong, L. H., Nanoparticle-induced grain growth of carbon-free solution-processed CuIn(S,Se)_{2} solar cell with 6% efficiency. *ACS Appl Mater Interfaces* **2013**, *5* (5), 1533-7.
65. Kishore Kumar, Y. B.; Suresh Babu, G.; Uday Bhaskar, P.; Sundara Raja, V., Preparation and characterization of spray-deposited $\text{Cu}_{2}\text{ZnSnS}_{4}$ thin films. *Solar Energy Materials and Solar Cells* **2009**, *93* (8), 1230-1237.
66. Kumar, Y. B. K.; Babu, G. S.; Bhaskar, P. U.; Raja, V. S., Effect of starting-solution pH on the growth of $\text{Cu}_{2}\text{ZnSnS}_{4}$ thin films deposited by spray pyrolysis. *physica status solidi (a)* **2009**, *206* (7), 1525-1530.

67. Kumar, Y. B. K.; Bhaskar, P. U.; Babu, G. S.; Raja, V. S., Effect of copper salt and thiourea concentrations on the formation of Cu₂ZnSnS₄ thin films by spray pyrolysis. *physica status solidi (a)* **2010**, *207* (1), 149-156.
68. Madarász, J.; Bombicz, P.; Okuya, M.; Kaneko, S., Thermal decomposition of thiourea complexes of Cu(I), Zn(II), and Sn(II) chlorides as precursors for the spray pyrolysis deposition of sulfide thin films. *Solid State Ionics* **2001**, *141–142* (0), 439-446.
69. Platzer-Björkman, C.; Scragg, J.; Flammersberger, H.; Kubart, T.; Edoff, M., Influence of precursor sulfur content on film formation and compositional changes in Cu₂ZnSnS₄ films and solar cells. *Solar Energy Materials and Solar Cells* **2012**, *98*, 110-117.
70. Bacewicz, R.; Gebicki, W.; Filipowicz, J., Raman scattering in CuInS₂ x Se₂(1-x) mixed crystals. *Journal of Physics: Condensed Matter* **1994**, *6* (49), L777.
71. Maeda, T.; Nakamura, S.; Wada, T., First Principles Calculations of Defect Formation in In-Free Photovoltaic Semiconductors Cu₂ZnSnS₄ and Cu₂ZnSnSe₄. *Japanese Journal of Applied Physics* **2011**, *50* (4), 04DP07.
72. Fontané, X.; Calvo-Barrio, L.; Izquierdo-Roca, V.; Saucedo, E.; Pérez-Rodríguez, A.; Morante, J. R.; Berg, D. M.; Dale, P. J.; Siebentritt, S., In-depth resolved Raman scattering analysis for the identification of secondary phases: Characterization of Cu₂ZnSnS₄ layers for solar cell applications. *Applied Physics Letters* **2011**, *98* (18), 181905.
73. Hsu, W.-C.; Repins, I.; Beall, C.; DeHart, C.; Teeter, G.; To, B.; Yang, Y.; Noufi, R., The effect of Zn excess on kesterite solar cells. *Solar Energy Materials and Solar Cells* **2013**, *113*, 160-164.
74. Lindahl, J.; Wätjen, J. T.; Hultqvist, A.; Ericson, T.; Edoff, M.; Törndahl, T., The effect of Zn_{1-x}Sn_xO_y buffer layer thickness in 18.0% efficient Cd-free Cu(In,Ga)Se₂ solar cells. *Progress in Photovoltaics: Research and Applications* **2013**, *21* (8), 1588-1597.
75. Hultqvist, A.; Edoff, M.; Törndahl, T., Evaluation of Zn₂SnO buffer layers for CuIn_{0.5}Ga_{0.5}Se₂ solar cells. *Progress in Photovoltaics: Research and Applications* **2011**, *19* (4), 478-481.
76. Davies, G., The optical properties of luminescence centres in silicon. *Physics Reports* **1989**, *176* (3–4), 83-188.
77. Zhang, S. K.; Lu, H.; Wang, W. B.; Das, B. B.; Okoye, N.; Tamargo, M.; Alfano, R. R., Radiative and nonradiative recombination processes in ZnCdSe / ZnCdMgSe multi-quantum-wells. *Journal of Applied Physics* **2007**, *101* (2), 023111.
78. Chen, R.; Tay, Y.; Ye, J.; Zhao, Y.; Xing, G.; Wu, T.; Sun, H., Investigation of Structured Green-Band Emission and Electron-Phonon Interactions in Vertically Aligned ZnO Nanowires. *The Journal of Physical Chemistry C* **2010**, *114* (41), 17889-17893.
79. Chen, R.; Xing, G. Z.; Gao, J.; Zhang, Z.; Wu, T.; Sun, H. D., Characteristics of ultraviolet photoluminescence from high quality tin oxide nanowires. *Applied Physics Letters* **2009**, *95* (6), 061908.
80. Luckert, F.; Hamilton, D. I.; Yakushev, M. V.; Beattie, N. S.; Zoppi, G.; Moynihan, M.; Forbes, I.; Karotki, A. V.; Mudryi, A. V.; Grossberg, M.; Krustok, J.; Martin, R. W., Optical properties of high quality Cu₂ZnSnSe₄ thin films. *Applied Physics Letters* **2011**, *99* (6), 062104.
81. Khare, A.; Himmetoglu, B.; Johnson, M.; Norris, D. J.; Cococcioni, M.; Aydil, E. S., Calculation of the lattice dynamics and Raman spectra of copper zinc tin chalcogenides and comparison to experiments. *Journal of Applied Physics* **2012**, *111* (8), 083707.
82. Khare, A.; Himmetoglu, B.; Cococcioni, M.; Aydil, E. S., First principles calculation of the electronic properties and lattice dynamics of Cu₂ZnSn(S_{1-x}Se_x)₄. *Journal of Applied Physics* **2012**, *111* (12), 123704.
83. Gürel, T.; Sevik, C.; Çağın, T., Characterization of vibrational and mechanical properties of quaternary compounds Cu₂ZnSnS₄ and Cu₂ZnSnSe₄ in kesterite and stannite structures. *Physical Review B* **2011**, *84* (20).

84. Metzger, W. K.; Repins, I. L.; Romero, M.; Dippo, P.; Contreras, M.; Noufi, R.; Levi, D., Recombination kinetics and stability in polycrystalline Cu(In,Ga)Se₂ solar cells. *Thin Solid Films* **2009**, *517* (7), 2360-2364.
85. Metzger, W. K.; Repins, I. L.; Contreras, M. A., Long lifetimes in high-efficiency Cu(In,Ga)Se₂ solar cells. *Applied Physics Letters* **2008**, *93* (2), 022110.
86. Han, L.; Koide, N.; Chiba, Y.; Mitate, T., Modeling of an equivalent circuit for dye-sensitized solar cells. *Applied Physics Letters* **2004**, *84* (13), 2433-2435.
87. Boix, P. P.; Wienk, M. M.; Janssen, R. A. J.; Garcia-Belmonte, G., Open-Circuit Voltage Limitation in Low-Bandgap Diketopyrrolopyrrole-Based Polymer Solar Cells Processed from Different Solvents. *The Journal of Physical Chemistry C* **2011**, *115* (30), 15075-15080.
88. Fabregat-Santiago, F.; Garcia-Belmonte, G.; Mora-Sero, I.; Bisquert, J., Characterization of nanostructured hybrid and organic solar cells by impedance spectroscopy. *Physical Chemistry Chemical Physics* **2011**, *13* (20), 9083-9118.
89. Wang, G.; Zhao, W.; Cui, Y.; Tian, Q.; Gao, S.; Huang, L.; Pan, D., Fabrication of a Cu₂ZnSn(S,Se)₄ photovoltaic device by a low-toxicity ethanol solution process. *ACS Appl Mater Interfaces* **2013**, *5* (20), 10042-7.
90. Courtel, F. M.; Paynter, R. W.; Marsan, B. t.; Morin, M., Synthesis, Characterization, and Growth Mechanism of n-Type CuInS₂ Colloidal Particles. *Chemistry of Materials* **2009**, *21* (16), 3752-3762.
91. Liu, Y.; Liu, A.; Hu, Z.; Liu, W.; Qiao, F., Impedance spectroscopy studies on CuPc/n-Si hybrid solar cell. *Journal of Physics and Chemistry of Solids* **2012**, *73* (5), 626-629.
92. Gunawan, O.; Gokmen, T.; Warren, C. W.; Cohen, J. D.; Todorov, T. K.; Barkhouse, D. A. R.; Bag, S.; Tang, J.; Shin, B.; Mitzi, D. B., Electronic properties of the Cu₂ZnSn(Se,S)₄ absorber layer in solar cells as revealed by admittance spectroscopy and related methods. *Applied Physics Letters* **2012**, *100* (25), 253905.
93. Todorov, T.; Gunawan, O.; Chey, S. J.; de Monsabert, T. G.; Prabhakar, A.; Mitzi, D. B., Progress towards marketable earth-abundant chalcogenide solar cells. *Thin Solid Films* **2011**, *519* (21), 7378-7381.
94. Cao, Q.; Gunawan, O.; Copel, M.; Reuter, K. B.; Chey, S. J.; Deline, V. R.; Mitzi, D. B., Defects in Cu(In,Ga)Se₂ Chalcopyrite Semiconductors: A Comparative Study of Material Properties, Defect States, and Photovoltaic Performance. *Advanced Energy Materials* **2011**, *1* (5), 845-853.
95. Macdonald, D.; Geerligs, L. J., Recombination activity of interstitial iron and other transition metal point defects in p- and n-type crystalline silicon. *Applied Physics Letters* **2004**, *85* (18), 4061-4063.
96. Hengel, I.; Neisser, A.; Klenk, R.; Lux-Steiner, M. C., Current transport in CuInS₂:Ga/Cds/Zno – solar cells. *Thin Solid Films* **2000**, *361–362* (0), 458-462.
97. Haight, R.; Barkhouse, A.; Gunawan, O.; Shin, B.; Copel, M.; Hopstaken, M.; Mitzi, D. B., Band alignment at the Cu₂ZnSn(S_xSe_{1-x})₄/CdS interface. *Applied Physics Letters* **2011**, *98* (25), 253502.
98. Duan, H.-S.; Yang, W.; Bob, B.; Hsu, C.-J.; Lei, B.; Yang, Y., The Role of Sulfur in Solution-Processed Cu₂ZnSn(S,Se)₄ and its Effect on Defect Properties. *Advanced Functional Materials* **2013**, *23* (11), 1466-1471.
99. Barkhouse, D. A. R.; Gunawan, O.; Gokmen, T.; Todorov, T. K.; Mitzi, D. B., Device characteristics of a 10.1% hydrazine-processed Cu₂ZnSn(Se,S)₄ solar cell. *Progress in Photovoltaics: Research and Applications* **2012**, *20* (1), 6-11.
100. Repins, I.; Contreras, M. A.; Egaas, B.; DeHart, C.; Scharf, J.; Perkins, C. L.; To, B.; Noufi, R., 19.9%-efficient ZnO/CdS/CuInGaSe₂ solar cell with 81.2% fill factor. *Progress in Photovoltaics: Research and Applications* **2008**, *16* (3), 235-239.

101. Chirila, A.; Reinhard, P.; Pianezzi, F.; Bloesch, P.; Uhl, A. R.; Fella, C.; Kranz, L.; Keller, D.; Gretener, C.; Hagendorfer, H.; Jaeger, D.; Erni, R.; Nishiwaki, S.; Buecheler, S.; Tiwari, A. N., Potassium-induced surface modification of Cu(In,Ga)Se₂ thin films for high-efficiency solar cells. *Nat Mater* **2013**, *12* (12), 1107-11.
102. Salomé, P. M. P.; Fjällström, V.; Szaniawski, P.; Leitão, J. P.; Hultqvist, A.; Fernandes, P. A.; Teixeira, J. P.; Falcão, B. P.; Zimmermann, U.; da Cunha, A. F.; Edoff, M., A comparison between thin film solar cells made from co-evaporated CuIn_{1-x}Ga_xSe₂ using a one-stage process versus a three-stage process. *Progress in Photovoltaics: Research and Applications* **2014**, n/a-n/a.
103. Wada, T.; Nakamura, S.; Maeda, T., Ternary and multinary Cu-chalcogenide photovoltaic materials from CuInSe₂ to Cu₂ZnSnS₄ and other compounds. *Progress in Photovoltaics: Research and Applications* **2012**, *20* (5), 520-525.
104. Vermang, B.; Wätjen, J. T.; Fjällström, V.; Rostvall, F.; Edoff, M.; Kotipalli, R.; Henry, F.; Flandre, D., Employing Si solar cell technology to increase efficiency of ultra-thin Cu(In,Ga)Se₂ solar cells. *Progress in Photovoltaics: Research and Applications* **2014**, n/a-n/a.
105. Guo, L.; Zhu, Y.; Gunawan, O.; Gokmen, T.; Deline, V. R.; Ahmed, S.; Romankiw, L. T.; Deligianni, H., Electrodeposited Cu₂ZnSnSe₄ thin film solar cell with 7% power conversion efficiency. *Progress in Photovoltaics: Research and Applications* **2014**, *22* (1), 58-68.
106. Kim, J.; Hiroi, H.; Todorov, T. K.; Gunawan, O.; Kuwahara, M.; Gokmen, T.; Nair, D.; Hopstaken, M.; Shin, B.; Lee, Y. S.; Wang, W.; Sugimoto, H.; Mitzi, D. B., High Efficiency Cu₂ZnSn(S,Se)₄ Solar Cells by Applying a Double In₂S₃/CdS Emitter. *Advanced Materials* **2014**, n/a-n/a.
107. Shin, B.; Zhu, Y.; Bojarczuk, N. A.; Jay Chey, S.; Guha, S., Control of an interfacial MoSe₂ layer in Cu₂ZnSnSe₄ thin film solar cells: 8.9% power conversion efficiency with a TiN diffusion barrier. *Applied Physics Letters* **2012**, *101* (5), 053903.
108. Zhou, H.; Song, T. B.; Hsu, W. C.; Luo, S.; Ye, S.; Duan, H. S.; Hsu, C. J.; Yang, W.; Yang, Y., Rational defect passivation of Cu₂ZnSn(S,Se)₄ photovoltaics with solution-processed Cu₂ZnSnS₄:Na nanocrystals. *J Am Chem Soc* **2013**, *135* (43), 15998-6001.
109. Repins, I. L.; Moutinho, H.; Choi, S. G.; Kanevce, A.; Kuciauskas, D.; Dippo, P.; Beall, C. L.; Carapella, J.; DeHart, C.; Huang, B.; Wei, S. H., Indications of short minority-carrier lifetime in kesterite solar cells. *Journal of Applied Physics* **2013**, *114* (8), 084507.
110. Gokmen, T.; Gunawan, O.; Mitzi, D. B., Minority carrier diffusion length extraction in Cu₂ZnSn(Se,S)₄ solar cells. *Journal of Applied Physics* **2013**, *114* (11), 114511.
111. Shannon, R., Revised effective ionic radii and systematic studies of interatomic distances in halides and chalcogenides. *Acta Crystallographica Section A* **1976**, *32* (5), 751-767.
112. Mendis, B. G.; Shannon, M. D.; Goodman, M. C. J.; Major, J. D.; Claridge, R.; Halliday, D. P.; Durose, K., Direct observation of Cu, Zn cation disorder in Cu₂ZnSnS₄ solar cell absorber material using aberration corrected scanning transmission electron microscopy. *Progress in Photovoltaics: Research and Applications* **2014**, *22* (1), 24-34.
113. Scragg, J. J. S.; Choubrac, L.; Lafond, A.; Ericson, T.; Platzer-Björkman, C., A low-temperature order-disorder transition in Cu₂ZnSnS₄ thin films. *Applied Physics Letters* **2014**, *104* (4), 041911.
114. Paris, M.; Choubrac, L.; Lafond, A.; Guillot-Deudon, C.; Jobic, S., Solid-State NMR and Raman Spectroscopy To Address the Local Structure of Defects and the Tricky Issue of the Cu/Zn Disorder in Cu-Poor, Zn-Rich CZTS Materials. *Inorg Chem* **2014**, *53* (16), 8646-53.
115. Robert Jaffe, J. P., Murray Hitzman, and Francis Slakey, Energy Critical Elements. *Physics & Society* **2011**, *40* (3).

116. Cui, Y.; Deng, R.; Wang, G.; Pan, D., A general strategy for synthesis of quaternary semiconductor Cu_2MSnS_4 ($\text{M} = \text{Co}^{2+}, \text{Fe}^{2+}, \text{Ni}^{2+}, \text{Mn}^{2+}$) nanocrystals. *Journal of Materials Chemistry* **2012**, 22 (43), 23136.
117. Wei, M.; Du, Q.; Wang, R.; Jiang, G.; Liu, W.; Zhu, C., Synthesis of New Earth-abundant Kesterite $\text{Cu}_2\text{MgSnS}_4$ Nanoparticles by Hot-injection Method. *Chemistry Letters* **2014**, 43 (7), 1149-1151.
118. Wang, Y.-X.; Wei, M.; Fan, F.-J.; Zhuang, T.-T.; Wu, L.; Yu, S.-H.; Zhu, C.-F., Phase-Selective Synthesis of $\text{Cu}_2\text{ZnSnS}_4$ Nanocrystals through Cation Exchange for Photovoltaic Devices. *Chemistry of Materials* **2014**.
119. Zhang, W.-B.; Chen, S.; Zeng, K., Tuning the crystal shape of materials by chemical potential: a combined theoretical and experimental study for NiSe_2 . *RSC Advances* **2014**, 4 (26), 13395-13404.
120. Yuan, B.; Luan, W.; Tu, S.-t., One-step solvothermal synthesis of nickel selenide series: Composition and morphology control. *CrystEngComm* **2012**, 14 (6), 2145-2151.
121. Berg, D. M.; Djemour, R.; Gütay, L.; Siebentritt, S.; Dale, P. J.; Fontane, X.; Izquierdo-Roca, V.; Pérez-Rodríguez, A., Raman analysis of monoclinic Cu_2SnS_3 thin films. *Applied Physics Letters* **2012**, 100 (19), -.
122. Naoya, A.; Ayaka, K.; Kazuki, K.; Manami, Y.; Kotoba, T.; Hideaki, A.; Akiko, T.; Hironori, K., Sulfurization temperature dependences of photovoltaic properties in Cu_2SnS_3 -based thin-film solar cells. *Japanese Journal of Applied Physics* **2014**, 53 (5S1), 05FW13.
123. Marcano, G.; Rincón, C.; López, S. A.; Sánchez Pérez, G.; Herrera-Pérez, J. L.; Mendoza-Alvarez, J. G.; Rodríguez, P., Raman spectrum of monoclinic semiconductor. *Solid State Communications* **2011**, 151 (1), 84-86.
124. Beigom Mortazavi Amiri, N.; Postnikov, A., Secondary phase Cu_2SnSe_3 vs. kesterite $\text{Cu}_2\text{ZnSnSe}_4$: Similarities and differences in lattice vibration modes. *Journal of Applied Physics* **2012**, 112 (3), -.
125. Postnikov, A. V.; Mortazavi Amiri, N. B., Calculated vibration spectrum of monoclinic Cu_2SnSe_3 in comparison with kesterite-type $\text{Cu}_2\text{ZnSnSe}_4$. *physica status solidi (a)* **2013**, 210 (7), 1332-1335.
126. Kevin, P.; Malik, S. N.; Malik, M. A.; O'Brien, P., The aerosol assisted chemical vapour deposition of SnSe and Cu_2SnSe_3 thin films from molecular precursors. *Chemical Communications* **2014**.
127. Heras, C. d. I.; Agulló-Rueda, F., Raman spectroscopy of NiSe_2 and $\text{NiS}_{2-x}\text{Se}_x$ ($0 < x < 2$) thin films. *Journal of Physics: Condensed Matter* **2000**, 12 (24), 5317.
128. Wang, D.; Huang, D.; Jin, C.; Liu, X.; Lin, Z.; Wang, J.; Wang, X., Raman spectra of $\text{Zn}_{1-x}\text{Mg}_x\text{SnSe}_{1-y}$ quaternary alloys. *Journal of Applied Physics* **1996**, 80 (2), 1248-1250.
129. Huang, D.; Jin, C.; Wang, D.; Liu, X.; Wang, J.; Wang, X., Crystal structure and Raman scattering in $\text{Zn}_{1-x}\text{Mg}_x\text{Se}$ alloys. *Applied Physics Letters* **1995**, 67 (24), 3611-3613.
130. Tanaka, K.; Oonuki, M.; Moritake, N.; Uchiki, H., thin film solar cells prepared by non-vacuum processing. *Solar Energy Materials and Solar Cells* **2009**, 93 (5), 583-587.
131. Guo, Q.; Ford, G. M.; Yang, W.-C.; Walker, B. C.; Stach, E. A.; Hillhouse, H. W.; Agrawal, R., Fabrication of 7.2% Efficient CZTSSe Solar Cells Using CZTS Nanocrystals. *Journal of the American Chemical Society* **2010**, 132 (49), 17384-17386.
132. Platzer-Björkman, C.; Scragg, J.; Flammersberger, H.; Kubart, T.; Edoff, M., Influence of precursor sulfur content on film formation and compositional changes in $\text{Cu}_2\text{ZnSnS}_4$ films and solar cells. *Solar Energy Materials and Solar Cells* **2012**, 98 (0), 110-117.
133. Narasinha, S.; Rohatgi, A. In *Optimized aluminum back surface field techniques for silicon solar cells*, Photovoltaic Specialists Conference, 1997., Conference Record of the Twenty-Sixth IEEE, 29 Sep-3 Oct 1997; 1997; pp 63-66.

134. Schultz, O.; Glunz, S. W.; Willeke, G. P., SHORT COMMUNICATION: ACCELERATED PUBLICATION: Multicrystalline silicon solar cells exceeding 20% efficiency. *Progress in Photovoltaics: Research and Applications* **2004**, *12* (7), 553-558.
135. Narasimha, S.; Rohatgi, A.; Weeber, A. W., An optimized rapid aluminum back surface field technique for silicon solar cells. *Electron Devices, IEEE Transactions on* **1999**, *46* (7), 1363-1370.
136. Dao, V. A.; Heo, J.; Choi, H.; Kim, Y.; Park, S.; Jung, S.; Lakshminarayan, N.; Yi, J., Simulation and study of the influence of the buffer intrinsic layer, back-surface field, densities of interface defects, resistivity of p-type silicon substrate and transparent conductive oxide on heterojunction with intrinsic thin-layer (HIT) solar cell. *Solar Energy* **2010**, *84* (5), 777-783.

Appendix A: List of Abbreviations

CZTSSe	$\text{Cu}_2\text{ZnSn}(\text{S},\text{Se})_4$
CIGSSe	$\text{Cu}(\text{In},\text{Ga})(\text{S},\text{Se})_2$
CMTSSe	$\text{Cu}_2\text{MSn}(\text{S},\text{Se})_4$ (M=metal)
CTS	$\text{Cu}_2\text{Sn}(\text{S},\text{Se})_3$
CB	Conduction Band
VB	Valence Band
CBD	Chemical Bath Deposition
TCO	Transparent Conducting Oxide
E_g	Energy Band Gap
V_{oc}	Open Circuit Voltage
J_{sc}	Short Circuit Current
FF	Fill Factor
η	Solar Cell Efficiency
PL	Photoluminescence
V_{fb}	Flat Band Potential
EQE	External Quantum Efficiency
SCR	Space Charge Region
FE-SEM	Field Emission Scanning Electron Microscope
XRD	X-ray Diffraction
SIMS	Secondary Ion Mass Spectroscopy
EDS	Energy Dispersive X-Ray Spectroscopy
DAPs	Donor-Acceptor Pairs

Appendix B: List of Publications

Journals

1. Zeng, X.; Boix, P. P.; Lee, K. K.; Chen, X.; Wong, L. H., Influence of the energetic alignment on the Voc of $\text{Cu}_2\text{ZnSn}(\text{S,Se})_4$ solar cells studied by impedance spectroscopy. Submitted to ACS AMI
2. Prabhakar, R. R.; Su, Z.; Zeng, X.; Baiker, T.; Shukla, S.; Batabyal, S. K.; Wong, L. H., Photovoltaic Effect in Earth Abundant Solution Processed $\text{Cu}_2\text{MnSnS}_4$ and $\text{Cu}_2\text{MnSn}(\text{S,Se})_4$ Thin Films. In preparation
3. Zeng, X.; Tai, K. F.; Zhang, T.; Ho, C. W. J.; Chen, X.; Huan, A.; Sum, T. C.; Wong, L. H., $\text{Cu}_2\text{ZnSn}(\text{S,Se})_4$ kesterite solar cell with 5.1% efficiency using spray pyrolysis of aqueous precursor solution followed by selenization. Solar Energy Materials and Solar Cells 2014, 124, 55-60.
4. Li, Z.; Ho, J. C. W.; Lee, K. K.; Zeng, X.; Zhang, T.; Wong, L. H.; Lam, Y. M., Environmentally friendly solution route to kesterite $\text{Cu}_2\text{ZnSn}(\text{S,Se})_4$ thin films for solar cell applications. RSC Advances 2014, 4 (51), 26888-26894.
5. Zeng, X.; Pramana, S. S.; Batabyal, S. K.; Mhaisalkar, S. G.; Chen, X.; Jinesh, K. B., Low temperature synthesis of wurtzite zinc sulfide (ZnS) thin films by chemical spray pyrolysis. Physical Chemistry Chemical Physics 2013, 15 (18), 6763-6768.
6. Su, Z.; Tan, M. R. J.; Li, X.; Zeng, X.; Batabyal, S. K.; Wong, L. H.; Cation Substitution of Solution-Processed $\text{Cu}_2\text{ZnSnS}_4$ Thin Film Solar Cell with over 9% Efficiency. Advanced Energy Materials 2015, DOI: 10.1002/aenm.201500682

Conferences

1. Zeng, X.; Tai, K. F.; Zhang, T.; Ho, C. W. J.; Wong, L. H.; Chen, X.; Mhaisalkar, S. G., Kesterite solar cell with 5.1% efficiency using solution based chemical spray pyrolysis of $\text{Cu}_2\text{ZnSnS}_4$ followed by selenization. 2012 MRS Fall Meeting & Exhibit, poster presentation
2. Zeng, X.; Tai, K. F.; Boix, P. P.; Wong, L. H., Impedance spectroscopy and photoluminescence characterization of 5.1% kesterite solar cell fabricated by chemical spray pyrolysis method. 2014 EU PVSEC, visual presentation

Patents

1. Prabhakar, R. R., Zeng, X., Batabyal, S. K., Wong, L. H., $\text{Cu}_2\text{MSn}(\text{S,Se})_4$ (M= Mn, Fe, Co, Ni) semiconducting photovoltaic materials. 2014

2. Ho, C. W. J.; Zeng, X.; Batabyal, S. K.; Lu, C. K. A.; Wong, L. H., Carbon-Free CIGS and CZTS type Devices on Mo Substrates by Spray Pyrolysis in ambient environment. 2013